

University of New Mexico

UNM Digital Repository

Electrical and Computer Engineering ETDs

Engineering ETDs

Fall 11-8-2019

EXPERIMENTAL TESTING OF A 3D-PRINTED METAMATERIAL SLOW WAVE STRUCTURE FOR HIGH POWER MICROWAVE GENERATION

Antonio B. de Alleluia
The University of New Mexico

Follow this and additional works at: https://digitalrepository.unm.edu/ece_etds



Part of the [Electrical and Computer Engineering Commons](#), and the [Plasma and Beam Physics Commons](#)

Recommended Citation

de Alleluia, Antonio B.. "EXPERIMENTAL TESTING OF A 3D-PRINTED METAMATERIAL SLOW WAVE STRUCTURE FOR HIGH POWER MICROWAVE GENERATION." (2019). https://digitalrepository.unm.edu/ece_etds/481

This Thesis is brought to you for free and open access by the Engineering ETDs at UNM Digital Repository. It has been accepted for inclusion in Electrical and Computer Engineering ETDs by an authorized administrator of UNM Digital Repository. For more information, please contact amywinter@unm.edu, lsloane@salud.unm.edu, sarahrk@unm.edu.

Antonio Breno de Alleluia

Candidate

Electrical and Computer Engineering

Department

This thesis is approved, and it is acceptable in quality and form for publication:

Approved by the Thesis Committee:

Dr. Edl Schamiloglu, Chairperson

Dr. Mark Gilmore

Dr. Ahmed Elfrgani

**EXPERIMENTAL TESTING OF A 3D-PRINTED METAMATERIAL SLOW WAVE STRUCTURE FOR
HIGH POWER MICROWAVE GENERATION**

by

ANTONIO BRENO DE ALLELUIA

B.S. IN ELECTRICAL ENGINEERING

STATE UNIVERSITY OF RIO DE JANEIRO

2004

THESIS

Submitted in Partial Fulfillment of the
Requirements for the Degree of

Master of Science

In

Electrical Engineering

The University of New Mexico

Albuquerque, New Mexico

DECEMBER 2019

Dedication

In memory of engineer Jose Ricardo Pena Borges, who supported me during a great family lost and shown me how amazing science could be when you have four years old.

In memory of my grand grandmother Alzira, who told funny stories and always pushed me to be better and help others.

To my beloved grandmothers Maria Jose e Maria da Conceicao who took care of me and allowed me to explore their house with my little experiments

To my dad, best professor ever, who most of the time gave me books instead of toys to build a library, believing that a great nation is built on books.

To my mother who let me learn basic science burning down my wardrobe and from physical discipline taught basic math and English (no regrets or that).

To my beloved sisters for their love and comprehension in let me doing experiments in their dolls.

To my beloved wife who supported me in moments of sorrow and great stress during the thesis.

To my two beautiful kids Duda and little Antonio, who are the joys of my life and my strength to keep moving.

To the Al Mighty God, Creator of the universe and Source of all Knowledge and my personal inspiration.

Acknowledgements

I'm grateful to my technical advisor Dr. Motta from the State University of Sao Paulo, who had been training me over the last 10 years in high power microwave transmitters and looked for funds to support me today for the past 5 years.

I'm deeply grateful to my advisor, Dr. Edl Schamiloglu, for accepting me as his student and allowing me to do research in his Pulsed Power Beams and High-Power Microwaves Laboratory. As an experimentalist, he understood my preferences for not coding and computer simulation, although he introduced me to CST and PIC simulator. After 6 months of polishing bits and bytes first results came out. Today, one year and 11 months later I do recognize the importance of computational tools.

I would like to thank my committee members, Professors Mark Gilmore and Ahmed Elfrgani for joining Dr. Schamiloglu for their good advice and suggestions.

I would like to acknowledge the financial support of the Electrical and Computer Engineering Department of the University of New Mexico and the Brazilian Government for providing me the necessary financial support throughout my thesis work. I especially would like to thank my advisor for the scholarship provided to support my studies.

I am very much indebted to Mr. Bill Moeney, who provided deep conversation and thoughts about pulsed power regarding electron accelerators.

I am very much indebted to Dr Jane Lehr, who helped me in the modelling and simulation of pulsed power systems and good conversations about high power electromagnetic fields.

This thesis would not have been possible without the help, support, and patience of my lab mates Dmitrii Andreev (the Red October), Artem Kuskov (AK), Braulio Martinez, Stacie Hernandez, Joe, Raul, Bi, Jacob, Max, and the 5 new undergraduate students Chris, Eli, Cameron, Ethan, and Anna who drove me crazy with questions around the lab. It would have been a very lonely lab without all of them.

I would like to thank staff members Mrs. Yvoné Nelson and Cornelia Platero who provided academic and administrative support for my thesis work.

I would like to thank the Navy Technological Center in Sao Paulo, Navy Nuclear Development Directorate, High-Power Microwave Laboratory, and Patria Foundation for all technical and financial support.

The main ideas behind the research pursued in this thesis were supported by AFOSR MURI Grant FA9550-12-1-0489 at the University of New Mexico and the University of California, Irvine. In addition, supplemental support at the University of New Mexico was provided by AFOSR Grant FA9550-10-1-0103.

Experimental Testing of a 3D-Printed Metamaterial Slow Wave Structure for High Power Microwave Generation

by

Antonio Breno de Alleluia

B.S., Electrical Engineering, State University of Rio de Janeiro, 2004

M.S., Electrical and Computer Engineering, University of New Mexico, 2019

Abstract

A metamaterial (MTM) high power microwave (HPM) vacuum electron device (VED) was developed using 3D printing technology. The specific geometric pattern of the source can produce both negative permittivity and permeability to interact with a relativistic electron beam. The electron beam is generated using a pulsed electron accelerator with a maximum energy of 700 keV and lasting approximately 16 ns. The design of this novel VED consists of a circular waveguide loaded with complementary split-ring resonators in a linear periodic arrangement in which the relativistic beam travels guided by a magnetic field. The electrons interact with the MTM producing electromagnetic radiation, which is radiated to free space using a horn antenna. The HPM signal generated is characterized using a resistive sensor detector and a waveguide detector connected to a crystal diode. The radiation field distribution was measured using these detectors. Mode characterization is facilitated using an array of neon bulbs, which light up according to the intensity of the electric field. As a result, this excitation resembles the field pattern generated by the VED. The experimental results are compared with particle-in-cell (PIC) simulations and theoretical considerations.

TABLE OF CONTENTS

LIST OF FIGURES	ix
LIST OF TABLES	xiv
1 CHAPTER 1: INTRODUCTION	1
1.1 Background	1
1.1.1 Thesis Organization	7
2 CHAPTER 2: FUNDAMENTALS	8
2.1 Microwave Radiation Pattern.....	8
2.2 Far-Field and Near-Field Analysis	11
2.2.1 Radian and Solid Angle	13
2.2.2 E-Field Pattern	15
2.3 Total Radiated Power	16
2.4 Fundamentals of Pulsed Power	16
2.4.1 Electron Beam Accelerators	16
2.4.2 High Voltage Tesla Transformer and Pulse Forming Line.....	18
2.4.3 Spark Gap Gas Switch	20
2.4.4 Pulsed Magnet Circuit.....	21
2.5 Fundamentals of Metamaterials	23
3 CHAPTER 3: EXPERIMENTAL SETUP.....	26
3.1 3D Printed Metamaterial and Electron Beam Accelerator Setup.....	26

3.2	Characterization of Pulsed Power Driver and Magnetic Field.....	29
3.3	Cold Test Characterization.....	33
3.4	Frequency Characterization, Power, and Field Mapping.....	35
3.5	Optical Diagnostics	37
4	CHAPTER 4: RESULTS	40
4.1	Fundamentals of Computer Simulations	40
4.2	Simulation Results	41
4.3	Eigenmode Solver	42
4.4	Frequency Domain Solver.....	51
4.4.1	Experimental Results from the Vector Network Analyzer	53
4.5	Particle-in-Cell Simulation.....	56
4.5.1	PIC Simulation for 400 kV	56
4.5.2	PIC Simulation for 490 kV	61
4.5.3	PIC Simulation with SINUS Voltage Waveform Input File.....	69
4.6	Hot Test Experiments: Horizontal Power Scan.....	77
4.7	Visible Radiation Pattern Detection.....	83
5	CHAPTER 5: CONCLUSION AND FUTURE WORK	85
	REFERENCES.....	89

LIST OF FIGURES

Figure 2.1 3D field pattern simulated using CST.	9
Figure 2.2 Field regions of an antenna [11].	13
Figure 2.3 Schematic showing the solid angle [11].	14
Figure 2.4 Radian and steradian configuration [11].	14
Figure 2.5 E-Field distribution.	15
Figure 2.6 Power flow from the antenna at 2.95 GHz.	16
Figure 2.7 Solidworks model of the SINUS-6 electron beam accelerator.	17
Figure 2.8 Temporal energy compression in the SINUS-6 accelerator.	18
Figure 2.9 SINUS-6 equivalent circuit.	19
Figure 2.10 Tesla transformer waveform.	20
Figure 2.11 Layout of the spark gap gas switch: 1,4 brass electrodes; 2 pin, 5 N ₂ gas up to 22 ATM pressure in the switch housing.	21
Figure 2.12 Schematic of the pulsed magnetic circuit.	22
Figure 2.13 Pulsed current for the magnet.	22
Figure 2.14 Bose’s microwave experiment layout.	23
Figure 2.15 Classification of materials in terms of permittivity and permeability.	24
Figure 2.16 Complementary split ring resonators (CSSRs).	25
Figure 3.1 3D printed VED structure.	26
Figure 3.2 3D VED inside of the vacuum waveguide on the SINUS-6 accelerator.	27
Figure 3.3 Mechanical alignment of the MTMSWS.	28
Figure 3.4 Mechanical (left) and electrical beam alignment (right).	29
Figure 3.5 SINUS 6 pulsed power driver layout [22].	30

Figure 3.6 SINUS 6 spark gap gas switch [22].	30
Figure 3.7 Voltage as a function of spark gap pressure.	31
Figure 3.8 Cathode current as a function of spark gap pressure.	32
Figure 3.9 Pulsed magnetic field measurement.	33
Figure 3.10 Device under test.	33
Figure 3.11 Excitation probe for the 3D SWS.	34
Figure 3.12 Photograph of the RF detector.	35
Figure 3.13 RF measurement experimental layout.	36
Figure 3.14 Photograph of the resistive sensor used for field distribution measurements.	36
Figure 3.15 Photograph of the neon bulb array for field pattern measurement.	37
Figure 3.16 Optical diagnostics schematic for visible light emission.	38
Figure 3.17 HPM antenna output.	39
Figure 4.1 A unit cell of the MTM CSSR.	41
Figure 4.2 MTM's dimensions.	42
Figure 4.3 Dispersion characteristics for a single cell of the MTMSWS.	43
Figure 4.4 DBEO modes.	44
Figure 4.5 -Mode dispersion for hollow waveguide	44
Figure 4.6 Field distribution inside of a unit cell of the MTMSWS [27].	46
Figure 4.7 Mode 3 E field distribution from TM_{01} .	47
Figure 4.8 Mode 3 E Field distribution z-axis for TM_{01} mode.	47
Figure 4.9 Mode 3 magnetic field distribution for the TM_{01} mode.	48
Figure 4.10 Unit cell H-field z-direction distribution for the TM_{01} mode.	48

Figure 4.11 Coupling impedance as a function of frequency.	50
Figure 4.12 Dispersion curve with the beam line for an electron beam voltage of 400 kV [27].	51
Figure 4.13 Negative permittivity.	52
Figure 4.14 Negative permeability	52
Figure 4.15 Mode 2 excited with S_{22} at 2.731 GHz regarding TM_{01}	53
Figure 4.16 Mode 3 excited with S_{22} at 3.38 GHz TM_{01}	54
Figure 4.17 Higher order mode, which needs further investigation.	55
Figure 4.18 3D Printed MTMSWS with antenna.	56
Figure 4.19 Cathode voltage.	57
Figure 4.20 Cathode current.	57
Figure 4.21 Output RF power.	58
Figure 4.22 FFT of the output electric field.	58
Figure 4.23 PIC voltage and current waveforms from ICEPIC (blue line) and MAGIC (orange line).	59
Figure 4.24 Output RF power comparing ICEPIC (blue line) and MAGIC (orange line).	60
Figure 4.25 FFT of the electric field in ICEPIC (blue line) and MAGIC (orange line)..	60
Figure 4.26 SINUS voltage waveform in PIC simulations.	62
Figure 4.27 Cathode current from SINUS in PIC simulations.	62
Figure 4.28 Output RF power.	63
Figure 4.29 FFT of output electric field.	63
Figure 4.30 E-field distribution for 490 kV at different times.	64

Figure 4.31	Electric field distribution along the 11-period MTMSWS.....	65
Figure 4.32	Voltage in the first ring (straight).....	65
Figure 4.33	Voltage in the second ring (angle).....	66
Figure 4.34	FFT of the signal from ring 2.	66
Figure 4.35	Voltage in the slot of ring 2.....	67
Figure 4.36	FFT of ring 2 slot voltage.	67
Figure 4.37	Voltage in ring 3 (straight).	68
Figure 4.38	FFT of ring 4 slot voltage (angle).....	68
Figure 4.39	Transverse magnetic mode.	69
Figure 4.40	SINUS voltage waveform in experiment.....	69
Figure 4.41	Cathode current in experiment.	70
Figure 4.42	Output RF power in experiment.	70
Figure 4.43	FFT of the output RF electric field in experiment.....	71
Figure 4.44	Voltage in the slot of ring 2.....	71
Figure 4.45	FFT of the ring 2 slot voltage (angle).....	72
Figure 4.46	Voltage in the slot of ring 4 (angle).....	72
Figure 4.47	FFT of the ring 2 slot voltage (angle).....	73
Figure 4.48	Voltage between gaps 1-4.....	74
Figure 4.49	Electron bunching inside the SWS at 5.4 ns.....	76
Figure 4.50	Electron bunching inside SWS at 6.5 ns.....	76
Figure 4.51	Experimental hot test results [22].	77
Figure 4.52	Fast signal measurements: CH1-current, CH2-voltage, CH3-RF power, and CH4-frequency.....	78

Figure 4.53 Hot test results for the 3D printed MTMSWS.....	79
Figure 4.54 Output RF power signal from CST-SINUS-6 driver.....	81
Figure 4.55 Poynting vector distribution.	81
Figure 4.56 Horizontal power distribution.....	82
Figure 4.57 Computational versus experimental hot test results.	82
Figure 4.58 Radiation pattern from the neon bulb array.....	83
Figure 4.59 Visible light detection from the MTMSWS source.....	84
Figure 5.1 3D printed MTMSWS after more than 100 shots.....	85
Figure 5.2 3D printed MTMSWS in its waveguide.	86

LIST OF TABLES

Table 4-1 Cutoff frequencies for a hollow waveguide of 24 mm radius.....	45
Table 4-2 Comparison between PIC codes.	61
Table 4-3 Optimized PIC and benchmark parameters.	75
Table 4-4 Output RF power signal from CST using the SINUS voltage waveform.	80
Table 5-1 Average parameters.	87

1 CHAPTER 1: INTRODUCTION

1.1 Background

During the cold war, two nations were leading the studies of high-power microwaves (HPMs) applied to defense systems. The main characters were the United States and the former Soviet Union [1]. Most of the applications were counter-electronic against military systems. After the end of the Cold War and the collapse of the political socialist regime, it brought up transformation in science and technology regarding pulsed power and HPM. As a result, an exchange of information between the nations started. Later on, it integrated the international scientific community, universities, and research centers around the world. The power derby dilemma was a competition for the most powerful microwave generators designed between the two nations and was for many decades the main driver for their research. This dilemma pushed scientists to the development of new components and systems.

Among the new applications to stand out, interests in non-lethal, space weapons, and advanced technology for space travel brought the attention of the international scientific community over the years. Particularly noteworthy is the need for de-escalation of force in urban conflicts and the deployment of nonlethal weapons. Since most of the international conflicts nowadays occur in urban settings, the civilian population became collateral damage [2]. Therefore, it is necessary to apply high precision surgical tools capable of counteracting hostile forces on the ground with the lowest possibility of casualties. Besides that, space propulsion technology demands highly efficient thrust systems capable of achieving higher speeds. These systems have a direct impact on the launch cost as well as the product life cycle.

HPM sources are considered microwaves generators of powers greater than 100 MW peak power in the frequency range between 0.3 and 300 GHz [3]. The two categories of vacuum electron devices (VEDs) are linear structures (O-Type) and cross-field structures (M-Type). The first consists of devices such as the Backward Wave Oscillator (BWO) and the Traveling Wave Tube (TWT). The second consists of cross-field amplifiers and oscillator sources such as the TPO (tubes à propagation des ondes) and the magnetron. Pulsed electron beam accelerator systems that can generate short pulses in the range of some tens of nanoseconds are commonly used to power HPM devices. One of the most common sources using relativistic electron beams is the BWO. The BWO is a microwave VED that has a periodic rippled-wall waveguide structure through which an electron beam is injected axially using a pulsed power driver and an explosive emission cathode.

A set of electromagnetic coils generates an external magnetic field responsible for focusing and guiding the electrons in the slow wave structure (SWS). The beam propagates within the structure and is synchronous with an electromagnetic wave whose phase velocity is reduced because of the rippled-wall waveguide (hence, SWS). This results in the growth of the electromagnetic wave at the expense of the kinetic energy of electrons. Thus, this interaction enables electrons to radiate analogous to Cherenkov radiation [4], where they propagate at a local velocity greater than the characteristic speed in the medium. The region in the SWS where the electron beam reduces its kinetic energy and the electromagnetic wave grows is called the interaction region and the manner in which the electron beam interacts with the SWS is through the coupling impedance of the structure. The main feature for O-type sources, i.e., BWO, in general, is the use of an axial magnetic field and a longitudinal electron beam.

On the other hand, cross-field or M-Type sources have an electron beam perpendicular to the magnetic field. These devices include the magnetron and TPO, which have high efficiency for relativistic beam operation in electron accelerators. Research on VEDs of the BWO class has demonstrated multi-gigawatt output powers.

The research goals in this thesis on microwave VEDs are higher output power, efficiency, and miniaturization; these fundamentals led to the development and optimization of a new kind of HPM source that was produced using additive manufacturing. Additive manufacturing technology revolutionized the design and manufacture of VEDs. Initially, 3D printing technology reduced manufacturing cost and time for producing structures used in VEDs. Thereafter, it allowed for the construction of new SWS geometries that would be extremely expensive to produce due to their specificity in the traditional machinery production process. Additionally, this new industrial manufacturing achievement allows researchers in the field of HPM and pulsed electron beams to innovate in the process of component miniaturization. One of the greatest challenges is the development of 3D printed SWSs fully in metal [5]. Due to the dimensions of the device that was ultimately selected, 3D printing in metal was not possible because of the wall thickness.

A Multidisciplinary University Research Initiative (MURI) program sponsored by the Air Force Office of Scientific Research (AFOSR) was awarded to a team led by the University of New Mexico (UNM) in 2012. The team comprised five universities: UNM, Massachusetts Institute of Technology (MIT), Louisiana State University (LSU), Ohio State University (OSU), and the University of California Irvine (UCI). This program focused on studying metamaterials (MTMs) and their use in HPM sources. The particular SWS that is described in this thesis was developed by UNM's collaborators at UCI.

There is not a concise definition about MTMs, although it can be outlined in four principles: engineered materials, exotic properties, geometry, and design pattern. Thus, it is an engineered material from a design pattern with a specific geometry capable to exhibit exotic properties not found in nature. This type of material can be categorized in four different classes defined by the permittivity and permeability. Here we consider only double negative (DNG) MTMs where both permittivity and permeability are negative.

The DNG material distinguishes MTMs for electromagnetic applications. This property that is “beyond what is in nature” is the horsepower for linear microwave VEDs. DNG materials double the parameter space of seeking novel SWSs and beam-wave interaction structures. One of the key results of using DNG materials is to transmit microwave signals in waveguides below their cutoff frequency [6]. This reduces the cross-sectional dimension of the structures. Making new sources with highly complex geometries produce unique electromagnetic properties in the face of the natural characteristics of the material.

According to recent electromagnetic history, the DNG property was initially proposed by Veselago [8] in 1968 using the equations of Maxwell with negative permittivity and negative permeability. Given the high degree of theoretical abstraction for electromagnetic wave propagation, initially, the relevant applications only occurred decades later. This achievement was made possible by the work of Marques [9] who built small structures with subwavelength dimensions in which electromagnetic radiation was able to propagate below cutoff in a DNG medium. After this work, other scientists were able to perform similar experiments. Noteworthy is Smith, who was responsible for creating the first DNG material [10]. However, the applications previously studied had no relation to HPM. That was when in 2008 Marques published an article in which he brought the potential use to

HPM. His article revolutionized VED technology for particle accelerators. The construction of waveguides with split ring resonators (SRRs) generated negative values of permittivity and permeability. This characteristic is a result of a signal transmitted inside of a below cutoff waveguide. Therefore, this allowed for the reduction of the size of MTM microwave sources while increasing the RF signal strength.

In recent decades there has been considerable growth in the field of research for MTM with applications for scaling down the size of VEDs. A significant amount of scientific publications nowadays focuses on the research and development of new O-type sources. It is because for this type of geometry it is easy to construct 3D axial SRRs structures through which the electron beam propagates. Besides, it makes a counterpoint to the azimuthal interaction model observed in M-type devices as an interesting HPM source choice driven by electron accelerators.

An important limiting factor to be considered in the research and development of HPM sources is the concern of high voltage breakdown in the interaction structure. This phenomenon is the result of intense electric fields with high values in the internal regions of the SWS. For 3D printed VED devices, the possibility of this effect is extremely dangerous as it can destroy the SWS and at the same time reduce its efficiency. Plasma diagnostics can be used to observe the explosive electron emission from a graphite cathode. Through simulations using the CST particle-in-cell (PIC) code, it is possible to observe isolated points in which the intensity of the electric field is very high.

It is essential in the design of an HPM source to identify the dominant mode of operation. This mode describes the distribution and orientation of the fields inside the SWS self-consistent with the boundary conditions.

For MTM structures used in HPM sources, there are three classes of modes:

TE or H modes without the axial component of the electric field along the propagation axis and TM or E Modes without an axial component of the magnetic field along the propagation axis. Electric or magnetic hybrid (HE or HM) modes, a configuration in which the electromagnetic field has characteristics similar to TE and TM modes, are also possible. Throughout this thesis, only the TM mode will be studied to describe the behavior of the electromagnetic fields supported by the SWS.

The purpose of this thesis is to experimentally validate, through a set of hot tests, a 3D printed MTM VED [11]. The applied voltage, current, frequency, and total RF power parameters at the antenna output and radiation pattern will be compared with simulated computational values initially. From the voltage applied by the accelerator, the other parameters such as current and power are recorded and continuously monitored. The full RF power at the antenna output is obtained using horizontal and vertical scanning in the far-field region under an 3D printed arc-shaped structure. The operating frequency is recorded using two separate sensors, one S-band waveguide detector and one with a resistive element for the same spectrum. The microwave radiation pattern is verified using a 3D printed panel of neon discharge bulbs. Through computer simulations, the output dominant mode is evaluated and compared with experimental data. An SLR camera records time-integrated photographs of the neon discharge bulb array, which are then analyzed to determine the dominant model on the antenna output.

The relevance of this research is to counteract traditional manufacturing processes for VEDs with 3D technology and to demonstrate through experimental results their significance in the creation of new microwave devices with unique geometry for linear

electron accelerators. The research in HPM sources led by UNM is the result of expertise and highly technical skills in design and development of VEDs by researchers and professionals. Moreover, UNM is the national center of excellence for Directed Energy High Power Microwaves.

1.1.1 Thesis Organization

The organization of the thesis is as follows. Chapter 2 describes the fundamentals of microwave radiation and pulsed power applied to electron accelerators. Chapter 3 describes the experimental layout of the SWS and presents hot test results as well as integration of the MTM SWS with the SINUS-6 electron accelerator. Chapter 4 presents results from the PIC code, eigenmode solver, and experimental data. The experimental results include voltage and current from the cathode employing explosive emission, frequency, and power analysis of the RF signal as well as the radiation pattern evidenced by the neon panel. Chapter 5 contains the conclusions and suggestions for future work.

2 CHAPTER 2: FUNDAMENTALS

2.1 Microwave Radiation Pattern

The microwave radiation generation process is the result of the application of a high voltage pulse to a cathode and the interaction of the resultant electron beam with the SWS. Through the explosive emission model, it is possible to describe with computational simulation the generation of a relativistic electron beam and the generation of RF power. The definition of radiation pattern in the microwave literature is synthesized by C.A. Balanis [12] in *Antenna Theory Analysis and Design, 4th Ed.* An antenna radiation pattern or antenna pattern is defined as a “mathematical function or a graphical representation of the radiation properties of the antenna as a function of space coordinates. In most cases, the radiation pattern is determined in the far-field region and is represented as a function of the directional coordinates. Radiation properties include power flux density, radiation intensity, field strength, directivity, phase, or polarization.”

The radiation pattern of the horn antenna in the UNM experiments [13] is observed using a panel of neon bulb arrays in the far-field. The experimental measurement process can be described in 2D or 3D graphs for recorded power density for a 120° arc with a 5° angular pitch. Data acquisition for a 3D model requires a set of electronic sensors for the vertical and horizontal position. In order to simplify the measurement, discrete data from the horizontal and vertical scan were collected along an arc at a fixed radial distance from the antenna. The electric field strength detected at the receiver is called the field amplitude pattern. The field values are normalized to their maximum value recorded during the sweep by the receiver.

The electric field distribution contains two parts, the primary and secondary lobes. The main lobe contains most of the electric field strength while the secondary lobes are adjacent and have low field amplitude. Figure 2.1 illustrates the result of an S-band horn antenna simulation for the 3D distribution of electric field strength.

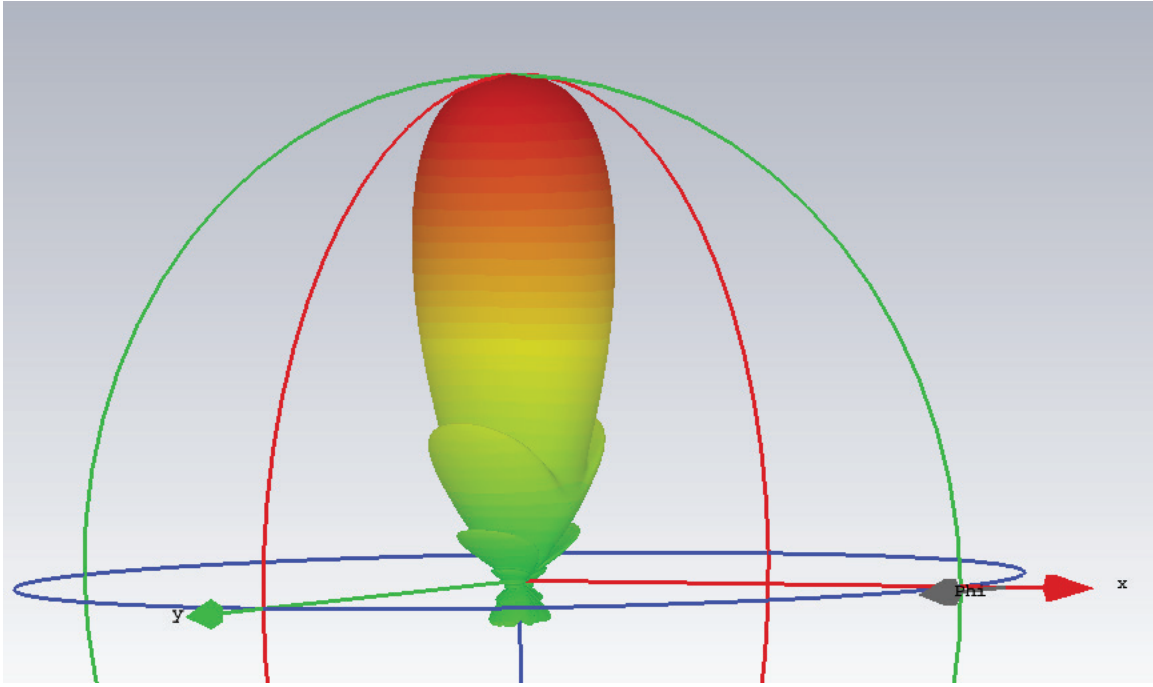


Figure 2.1 3D field pattern simulated using CST.

The computational results obtained using the CST time domain solver indicates that the difference in dBV between the primary and secondary lobe is 12.52 dBV. Importantly, secondary lobes should be avoided during antenna design in order not to reduce the density of the Poynting vector contained in the main. Besides, the underlying values may contribute to the formation of reflections, which can be detected at the receiver, making the signal interpretation difficult. The computational results and experiments for an S-band horn antenna will be compared in Chapter 3. One of the most critical analysis in antenna studies is to determine the electromagnetic fields as a function of current and spatial distribution,

respectively. The vector and scalar potential method for homogeneous media are deduced from the potential and vector functions described below:

$$\vec{B} = \mu \vec{H} = \nabla \times \vec{A} \quad (2-1)$$

$$\vec{E} = -\nabla \phi - i\omega \vec{A} \quad (2-2)$$

Similarly, \vec{A}, ϕ satisfy the Lorenz gauge:

$$\nabla A + i\omega \mu \epsilon \phi = 0 \quad (2-3)$$

Equations 2.1 and 2.2 are solutions of their respective wave (Helmholtz) equations:

$$(\nabla^2 + k^2) \vec{A} = -\mu \vec{J} \quad (2-4)$$

$$(\nabla^2 + k^2) \phi = -\frac{\rho}{\epsilon} \quad (2-5)$$

where $k = \omega \sqrt{\mu \epsilon}$.

In this way, it is possible to write the expressions for the electric and magnetic vector fields from the vector potential A of Equation 2.3

$$\vec{E} = -\frac{i\omega}{k^2} (\nabla \nabla \cdot \vec{A} + k^2 \vec{A}) \quad (2.6)$$

$$\vec{B} = \mu \vec{H} = \nabla \times \vec{A} \quad (2.7)$$

Solutions to the potential functions for a region of space R^3 due to volumetric distributions of currents and loads located in a finite region of space are:

$$\phi(\vec{r}) = \frac{1}{4\pi\epsilon} \int_{V'} \frac{\rho(\vec{r}') e^{-ikr}}{r} dV' \quad (2.8)$$

$$\vec{A}(\vec{r}) = \frac{\mu}{4\pi} \int_{v'} \frac{\vec{J}(\vec{r}') e^{-ikr}}{r} dV \quad (2.9)$$

Once the expression given by Equation 2.9 is known, it is possible to determine the electromagnetic fields using Equations 2.6 and 2.7.

2.2 Far-Field and Near-Field Analysis

The antenna study is analyzed in two distinct regions of interest. The first corresponds to the field in the region near the transmitting antenna, also known as the Fresnel region. In this condition the observation point satisfies $kr \ll 1$, $r \ll \lambda$ an induction field exists in which the reactive energy is stored in the fields during one part of the cycle and returns to the source in the other.

Another condition is the study of antennas for distant fields, also known as the Fraunhofer or far-field region. In this condition the observation point satisfies $kr \gg 1$ or $r \gg \lambda$. The far-field region is usually applied for communications and detection.

The vector potentials vary with radius and $e^{-ikr/r}$, so the equations are:

$$E = k^2 \frac{e^{-ikr}}{r} \left\{ \theta_1 \left[\left(\sqrt{\frac{\mu}{\epsilon}} \right) F_\phi + A_\phi \right] - \phi_1 \left[\left(\sqrt{\frac{\mu}{\epsilon}} \right) F_\phi - A_\phi \right] \right\} \quad (2.10)$$

$$H = k^2 \frac{e^{-ikr}}{r} \left\{ \theta_1 \left[F_\theta + \left(\sqrt{\frac{\epsilon}{\mu}} \right) A_\phi \right] - \phi_1 \left[F_\phi + \left(\sqrt{\frac{\mu}{\epsilon}} \right) A_\theta \right] \right\} \quad (2.11)$$

From the practical view of antenna analysis for near- and far-fields, the following equations can be used, respectively:

$$R_1 = 0.62 \sqrt{\frac{D^3}{\lambda}} \quad (2.12)$$

$$R_2 = \frac{2D^2}{\lambda} \quad (2.13)$$

In summary it is possible to say that the analysis of the signal received at the antenna can be modeled for three different regions:

- Reactive near-field region: It is the closest region to the transmitting antenna as stated in R1 from Figure 2.2, wherein the field is mostly reactive.
- Radiating near-field (Fresnel): It is the region between the Fresnel and far-field wherein radiation fields are dominant, and the angular electric distribution is dependent on distance.
- Radiating far-field (Fraunhofer): This is the most important region away from the antenna. In this case the field distribution is not proportional to distance or angular position. In this condition the wave is a spherical TEM wave and can be approximated as a plane wave. At this distance the field pattern is established, and the reactive components are negligible in the time average Poynting vector. This is the region of relevance for power measurements and in communications.

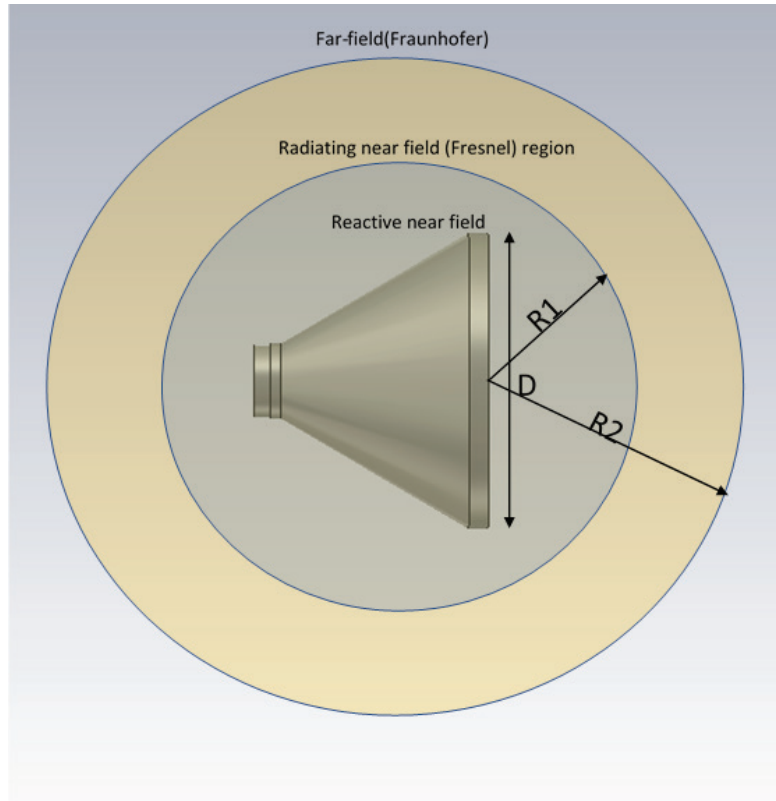


Figure 2.2 Field regions of an antenna [11].

2.2.1 Radian and Solid Angle

Angular measurement is intended to spatially identify the power density (Poynting vector) and total radiated power. Thus, the plane angle is the radian unit of measure with the vertex at the center of a circle with radius r . Figure 2.3 below illustrates the arc of length r . The differential area element dA is given by:

$$dA = r^2 \sin\theta d\theta d\phi \text{ (m}^2\text{)} \quad (2.14)$$

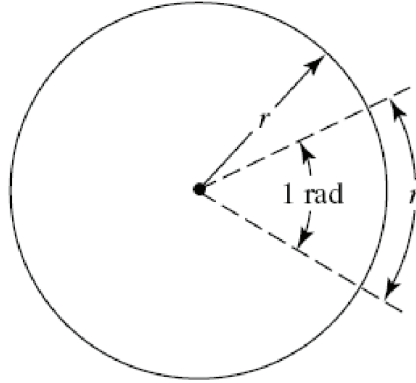


Figure 2.3 Schematic showing the solid angle [11].

The unit of measurement for solid angle is a rad with vertex at the center of a sphere of radius r which defines on its surface an area equal to r^2 . The solid angle element of Figure 2.4 and $d\Omega$ in the sphere is given by

$$d\Omega = \frac{dA}{r^2} = \sin\theta d\theta d\phi \quad (2.15)$$

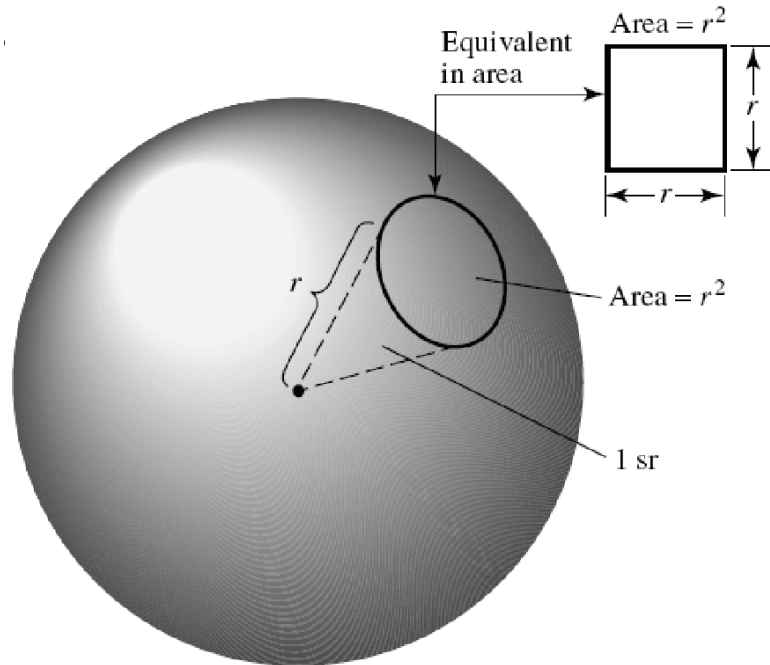


Figure 2.4 Radian and steradian configuration [11].

2.2.2 E-Field Pattern

The distribution of the electromagnetic field [14] in the far-field region along a specific arc, i.e. spherical coordinates in free space, determines the value of the Poynting vector. This distribution is of utmost importance in quantifying the power density. Figure 2.5 is a result of a CST time-domain solver computer simulation of an S-band horn antenna.

It is important to highlight that the half-power angle is 33.9°; the main lobe of the antenna is within this region. For values greater than this angle the signal strength decreases considerably. The scan error is $\frac{\pi}{8}$ as referenced in [12].

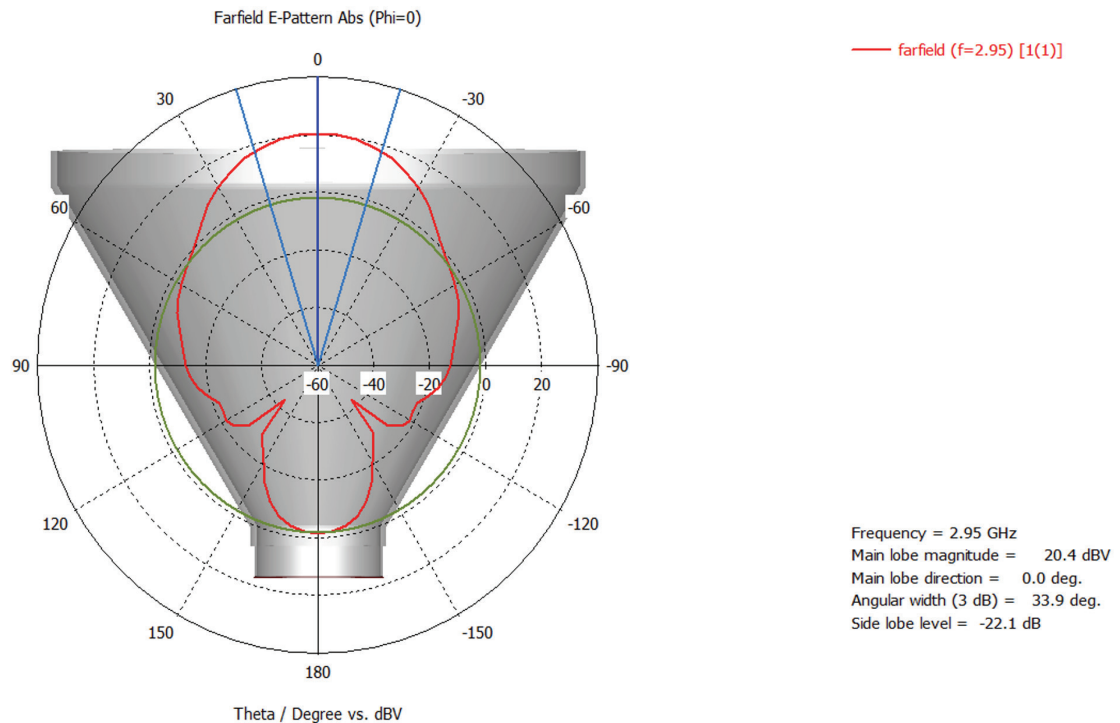


Figure 2.5 E-Field distribution.

2.3 Total Radiated Power

The total radiated power is the result of arc-integrated horizontal and vertical receiver scanning of power density at a fixed antenna distance. This value synthesizes the average Poynting vector (Watts/m²) and $dS = r^2 \sin\theta d\theta d\phi$. Thus, the total radiated power is:

$$P = \iint \langle S_r \rangle r^2 \sin\theta d\theta d\phi \quad (2.16)$$

The simulated spatial distribution of power density is illustrated in Figure 2.6. The experimental results from Chapter 03 will demonstrate a two-dimensional spatial scan.

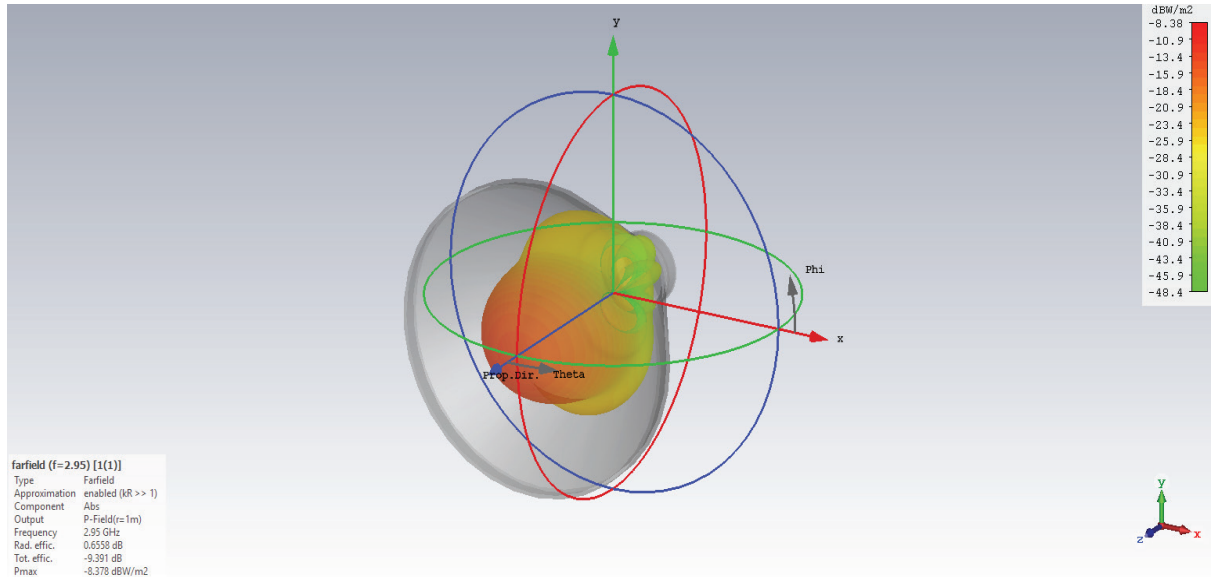


Figure 2.6 Power flow from the antenna at 2.95 GHz.

2.4 Fundamentals of Pulsed Power

2.4.1 Electron Beam Accelerators

The basic principles for the generation of high-power pulses in the time domain depend on the storage capacity of the electric energy and the switching speed for discharge. These two pillars of power electronics are the boundary conditions for the driver, allowing the

pulsed high voltage power supply to be effectively coupled to the load impedance. Figure 2.7 is an illustration of the SINUS-6 electron beam accelerator where the green capacitors store energy for the Tesla transformer and the yellow for solenoid coils.

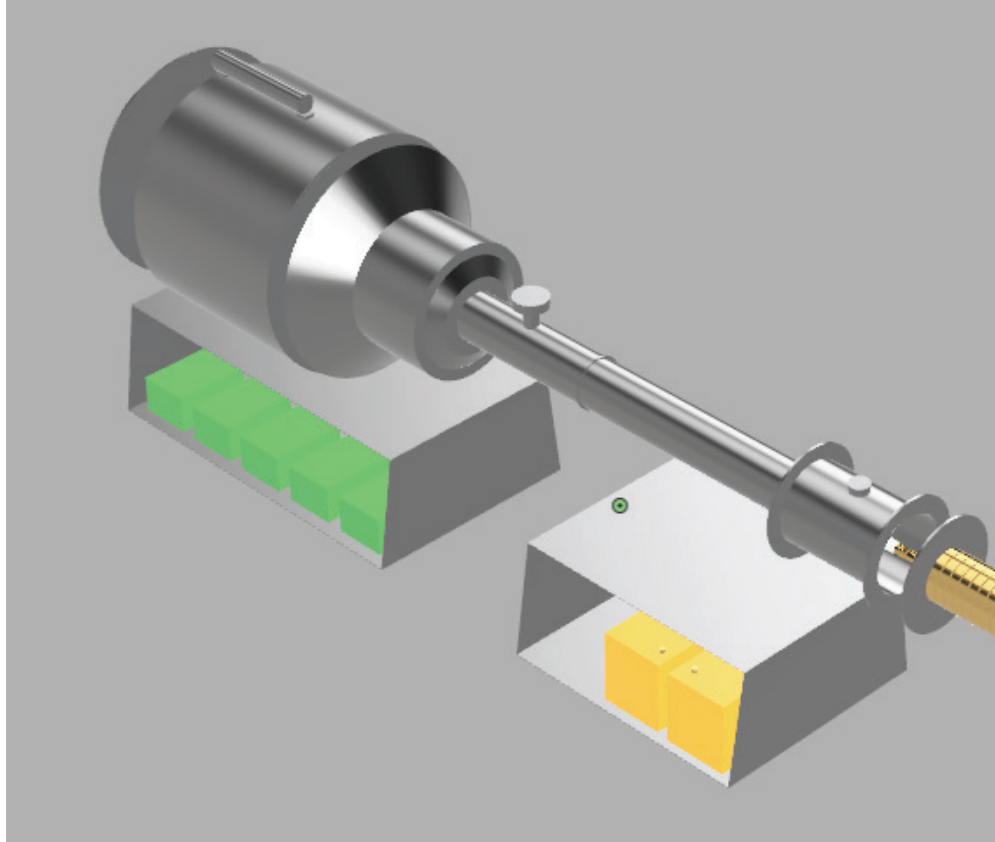


Figure 2.7 Solidworks artistic model of the SINUS-6 electron beam accelerator

In addition, the SINUS-6 [15] pulsed electron beam accelerator is featured in HPM research. It has the characteristic of long storage time and fast discharge. The timescale for pulse generation are: discharge transmission in seconds, milliseconds, microseconds and finally nanoseconds. In this way the stored electrical energy is transferred to a step-up Tesla transformer with a high coupling coefficient open ferromagnetic core. This circuit topology avoids magnetic saturation and enables high efficiency. The basic components of the

system are pulsed power supply, Tesla transformer, pulse forming line, and vacuum diode. The generation and formation of the electromagnetic pulse can be modeled from three initial parameters rise, fall, and flatness time, with the latter being the most important for describing the RF signal in the VED.

The pulsed power driver for the HPM MTM source is divided into four basic parts, as shown in Figure 2.8 for the SINUS-6 accelerator.

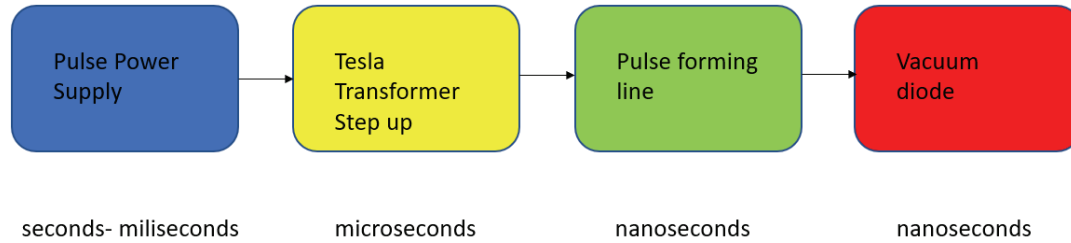


Figure 2.8 Temporal energy compression in the SINUS-6 accelerator.

2.4.2 High Voltage Tesla Transformer and Pulse Forming Line

The Tesla-type transformer [16] combined with the pulse forming line are at the heart of the accelerator, and the theoretical and experimental considerations of optimization for the magnetic circuit were described by Eltchaninov in the early 1980s. Figure 2.9 illustrates the simplified model of the magnetic circuit of the high voltage generator. The coupling coefficient k between the primary and secondary coils in the SINUS 6 is nearly 1.0.

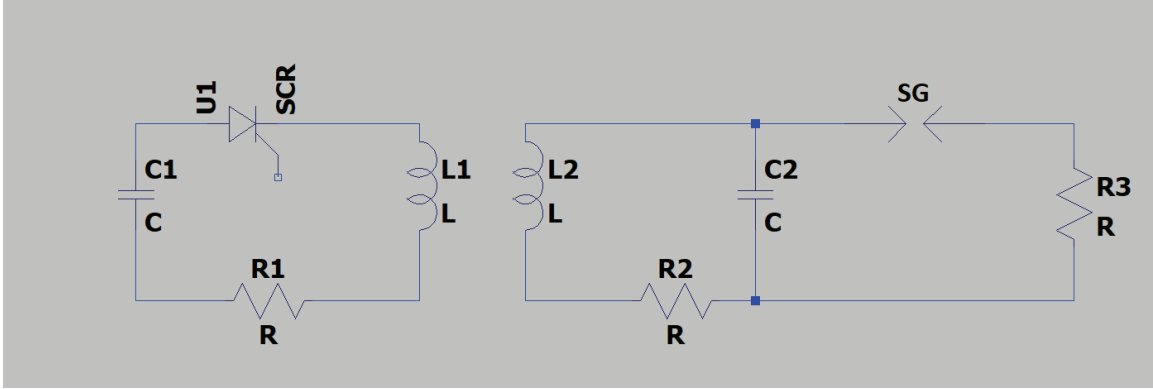


Figure 2.9 SINUS-6 equivalent circuit.

The magnetic circuit consists of a single turn in the primary and 3500 turns in the secondary. An SCR switch discharges the energy stored in capacitors at the primary of the transformer. The open-core ferromagnetic material for this transformer allows operation at high repetition rate, near 200 Hz, with high reliability without magnetic saturation. Due to technical and operational limitations and constraints of the facility, the SINUS-6 only operated in single shot mode.

Initial simulations for the Tesla transformer are illustrated in Figure 2 with the secondary indicating an output voltage of approximately 700 kV. The output voltage on the switch is important since oscillations in signal amplitude have a direct impact on the RF pulse formation from the electron beam/SWS interaction.

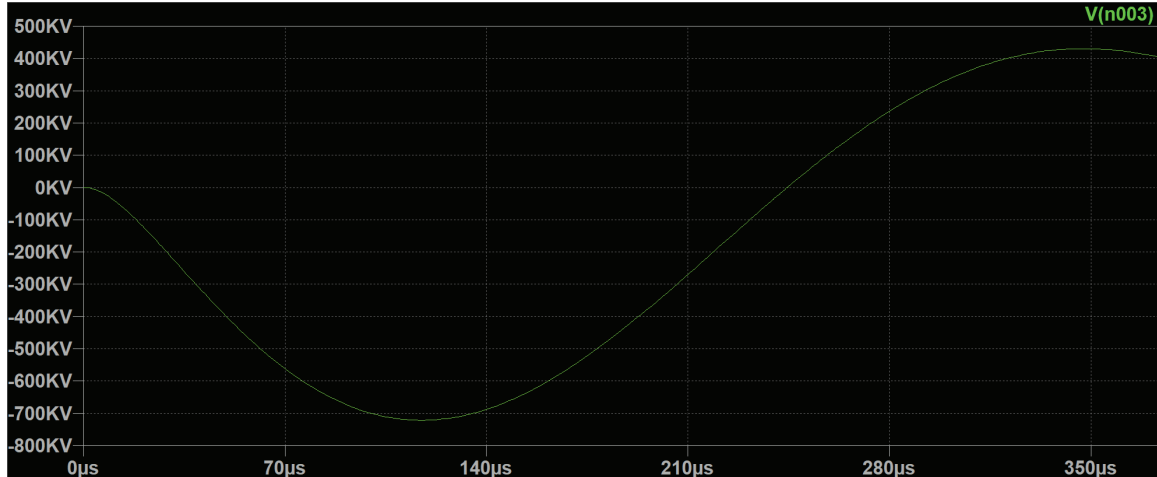


Figure 2.10 Tesla transformer waveform.

The energy generated by the Tesla transformer charges the pulse forming transmission line. This is responsible for the temporal compression of the electromagnetic energy. The forming line charging time for SINUS-6 is 60 μ S with an impedance of 20 Ω . The low impedance of the PFL is connected to a transmission line of $>100 \Omega$. To drive the diode, a small mismatch between PFL and transmission line is adjusted and as a result, there is a decrease in efficiency of conversion of the energy.

2.4.3 Spark Gap Gas Switch

The mechanism of gas breakdown in the spark gap switch follows Townsend's theory for electricity in gases, and Paschen's law. The SINUS-6 accelerator has a gas self-breaking voltage switch filled with nitrogen. Quoting J.C. Martin [17] "One of the minor irritations of my life has been the fact that while approximate calculations of the breakdown volts of practical sphere/sphere and cylinder/ cylinder gas give reasonable agreement to 10-20 percent, when more accurate attempts are made to compare experiment with crude theory,

reality seems strangely perverse.” The brass electrodes have a radius of 4.0. Figure 2.11 illustrates the gas gap self-breaking switch filled with nitrogen.

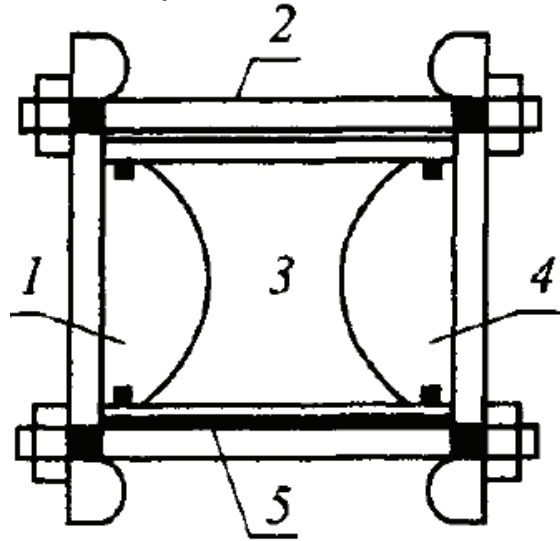


Figure 2.11 Layout of the spark gap gas switch: 1,4 brass electrodes; 2 pin, 5 N₂ gas up to 22 ATM pressure in the switch housing.

2.4.4 Pulsed Magnet Circuit

The arrangement of 9 coils generates up to 2 Tesla using a pulsed magnetic circuit. It is responsible for focusing the electron beam traveling inside the SWS. The confinement of the beam has a strong influence on the coupling impedance and, therefore, RF power output from the HPM source. Figure 2.12 illustrates the pulsed magnetic circuit. The synchronization of the high voltage Tesla transformer system and the solenoid is accomplished by trigger signals in the accelerator control box.

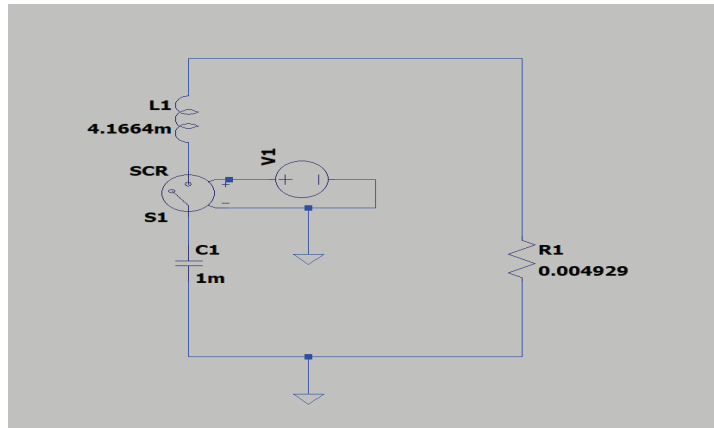


Figure 2.12 Schematic of the pulsed magnetic circuit.

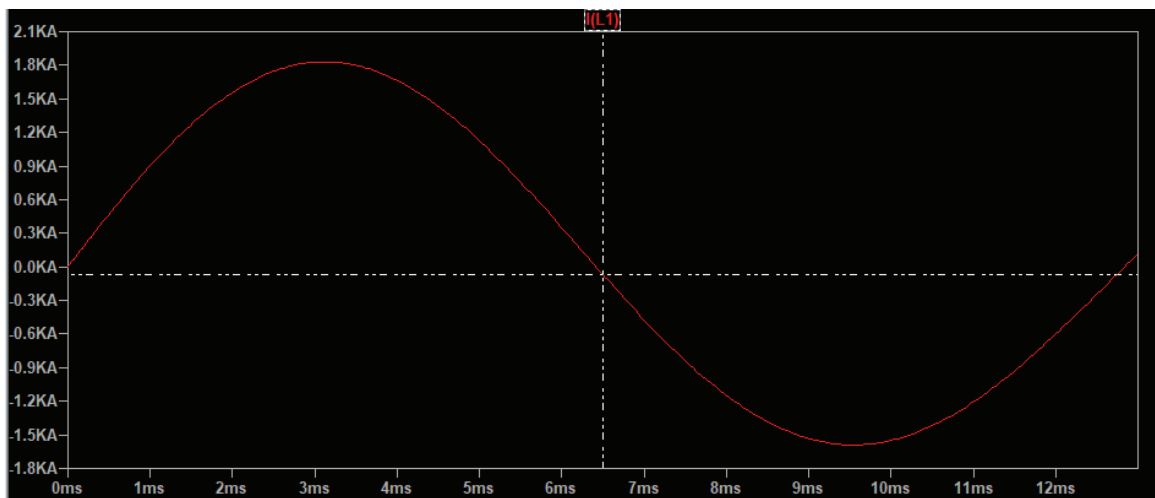


Figure 2.13 Pulsed current for the magnet.

2.5 Fundamentals of Metamaterials

The first studies on artificial materials, i.e., MTMs, were recorded [18] in the late 19th century. Researcher J.C. Bose conducted the microwave experiment with twisted structure geometries, as shown in Figure 2.13.

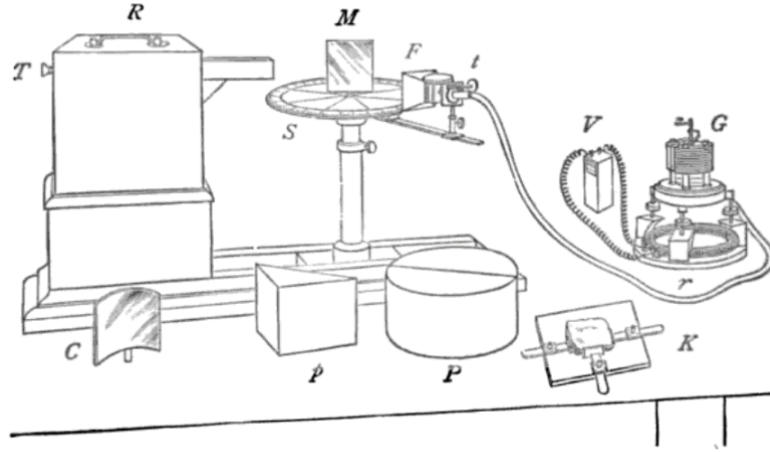


Figure 2.14 Bose's microwave experiment layout.

Interest in artificially modified materials with applications in electromagnetism has spurred researchers from the US and UK defense agencies [19]. From 1999 a multidisciplinary research program with American universities was created with Dr. Browning's initiative and on the British side led by Dr. John Pendry's initiative.

The definition of MTMs, according to researcher Rodger M. Walser of the University of Texas at Austin, is "Macroscopic composites having a man made, three-dimensional, periodic cellular architecture designed to produce an optimized combination, not available in nature, of two or more responses to specific excitation."

The exotic characteristics of MTMs [20] are not in their physical properties, but in their ability to extract, by geometric patterns, the desired effects not observed in nature. Thus, MTMs can be classified according to their permittivity and permeability as illustrated in Figure 2.15.

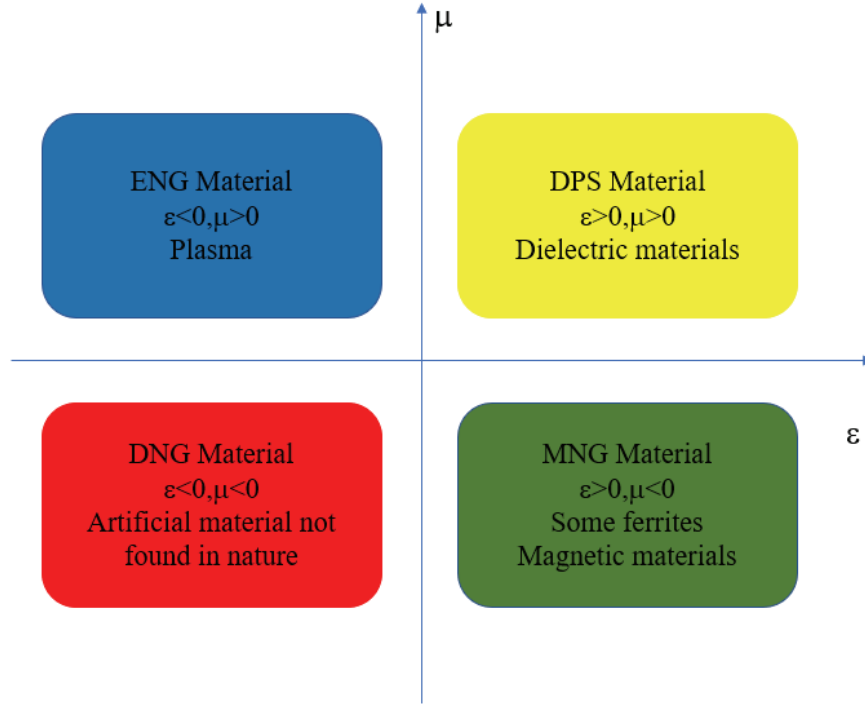


Figure 2.15 Classification of materials in terms of permittivity and permeability.

From the classification in Figure 2.15, the DNG property drives the design and research of accelerator HPM structures [21]. This feature allows signals to be propagated below the cut-off frequency in waveguides, as well as the higher power transmission for the same physical dimensions.

UCI has developed an MTM SWS based on the degenerate band edge (DBE) effect of frozen modes. The SWS consists of 11 pairs of complementary split rings misaligned by a 45° angle with a radial gap between them of 3.5 mm, and each unit cell is offset 180° .

Figure 2.16 illustrates the two rings in the SWS for HPM generation.



Figure 2.16 Complementary split ring resonators (CSSRs).

In this type of structure, the interaction of the electron beam depends on the geometric arrangement, as well as the degree of misalignment between the rings. A more detailed description of the structure will be given in Chapter 3.

3 CHAPTER 3: EXPERIMENTAL SETUP

3.1 3D Printed Metamaterial and Electron Beam Accelerator Setup

The MTMSWS was designed by Dr. Filippo Capolino's team from UCI. Initially, the designed MTMSWS did not fit inside of the interaction regime within the solenoid at UNM, and a series of interactive steps regarding computer simulations and mechanical assembling were performed. The final model optimized consisted of 11 pairs of CSRRs. This 3D printed structure fit within a vacuum waveguide. A unit cell comprises two CSRRs which are periodically loaded inside of waveguide. Figures 3.1 and 3.2 show the MTMSWS and its placement inside the waveguide.

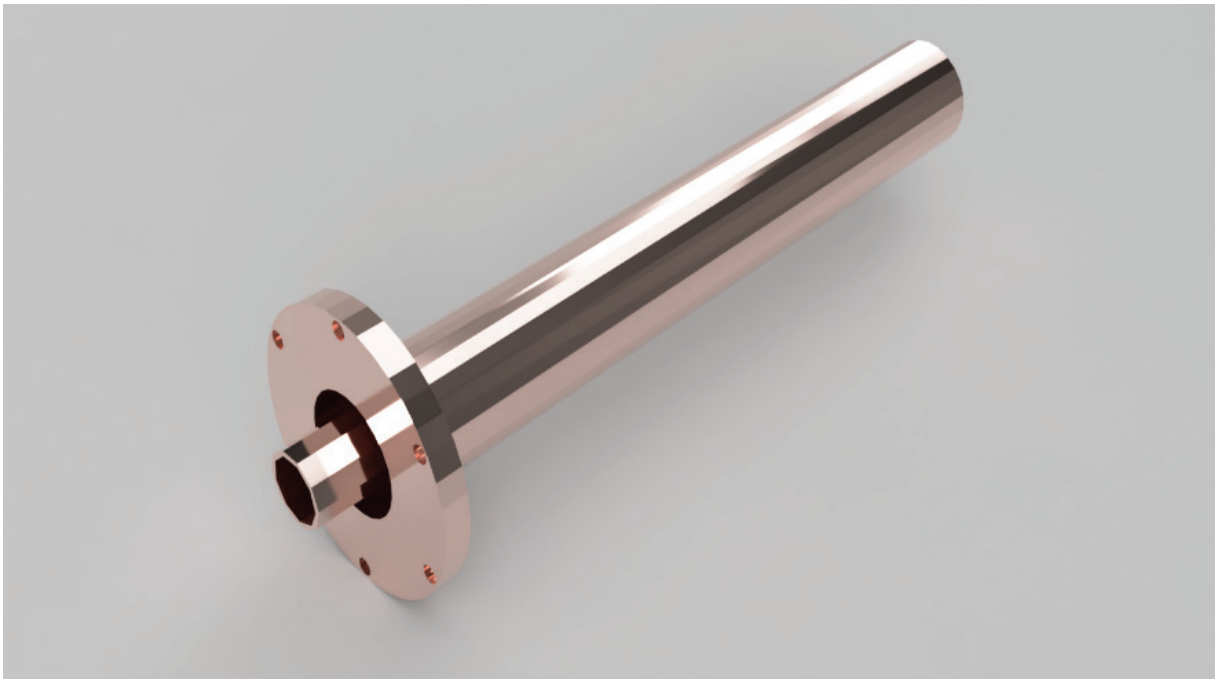


Figure 3.1 3D printed VED structure.

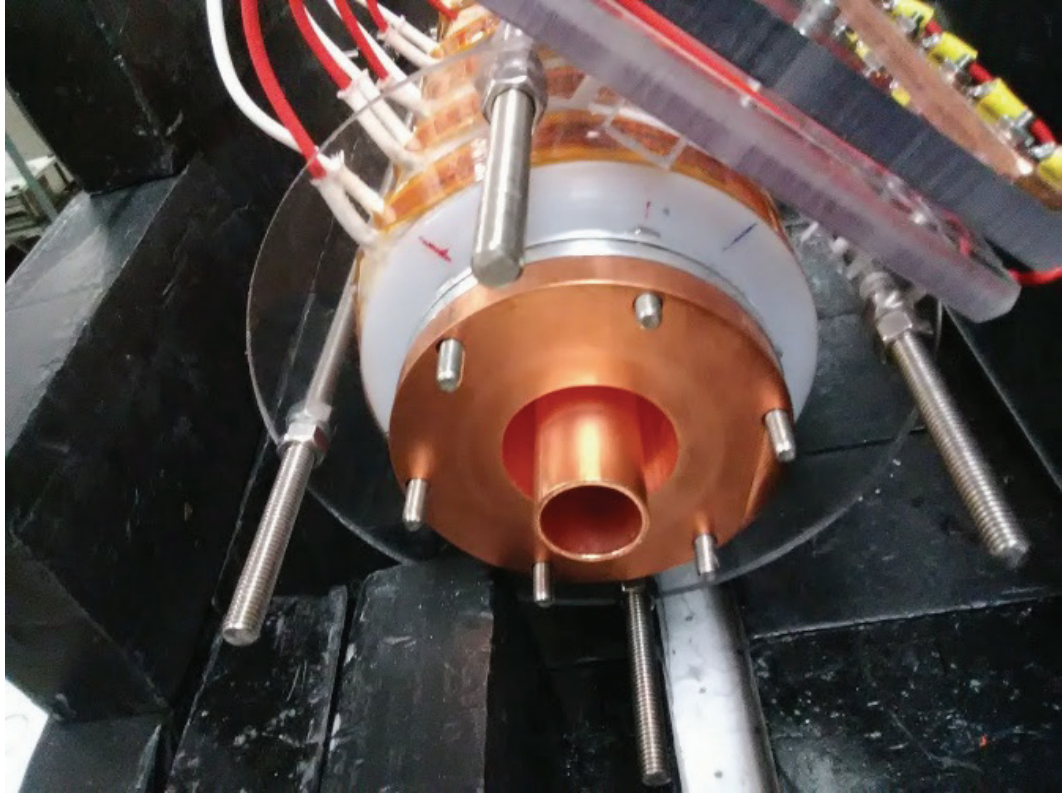


Figure 3.2 3D VED inside of the vacuum waveguide on the SINUS-6 accelerator.

The period of a unit cell is 15 mm. The dimensions are inner diameter 48.3 mm and 400 mm length. The MTMSWS is attached to the SINUS-6 pulsed electron beam accelerator. The center of the structure is mechanically aligned to the graphite cathode such that the relativistic electron beam travels through the structure guided by the pulsed magnetic field distribution produced by the solenoid.

Figure 3.3 shows the mechanical alignment procedure. After completing the assembly, the system is closed and fired to crosscheck the mechanical and electrical alignment.



Figure 3.3 Mechanical alignment of the MTMSWS.

The result from this procedure is illustrated in Figure 3.3. Good alignment is considered within about 90% and the beam should not intercept the inner parts of the structure. This was a great concern since the SWS is 3D printed in plastic and coated with copper. It is also important to note that misalignment has an influence on the interaction impedance of the SWS. This geometric issue must be minimized to increase the efficiency of the source. As the beam travels along the SWS it is slightly modulated.

A final alignment near 91% was achieved after firing the accelerator. In this case the witness plate suggested good alignment. The result through “eyeball” in Figure 3.4 (left side) seemed to suggest sufficient alignment.

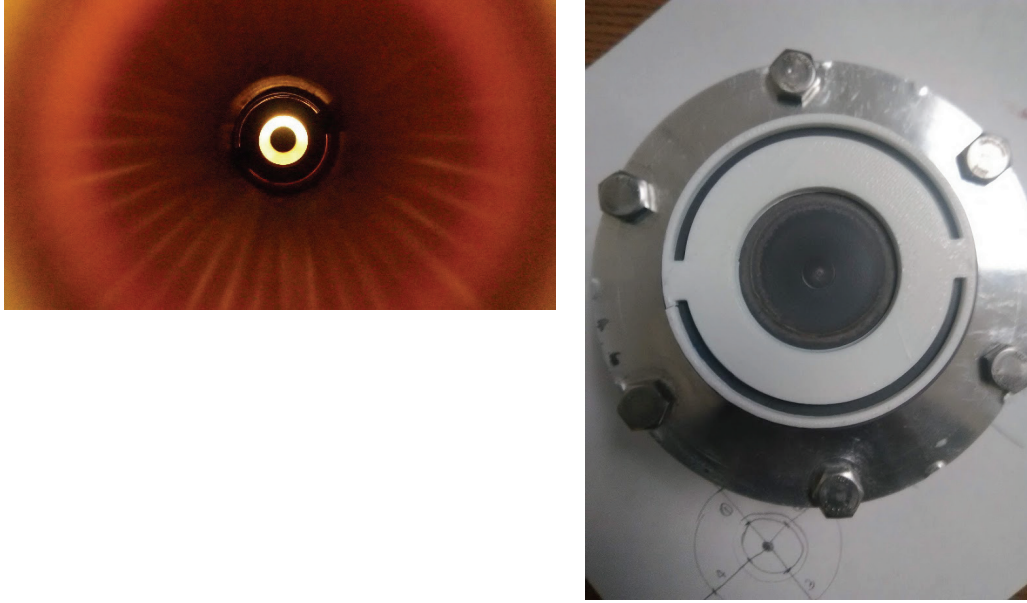


Figure 3.4 Mechanical (left) and electrical beam alignment (right).

Scientists from the Institute of High Current Electronics, Siberian Division of the Russian Academy of Sciences, designed and constructed UNM's SINUS-6 pulsed electron beam accelerator for HPM sources with a pulse width of approximately 16 ns.

3.2 Characterization of Pulsed Power Driver and Magnetic Field

The electron beam accelerator is capable of delivering 700 kV and 6 kA in single shot operation as illustrated in Figure 3.5. The primary of the Tesla transformer is charged up to 258.4 VDC and discharged in 60 μ s. Under this circumstance, the self-breaking gas switch plays an important role in discharging the energy stored in the pulse forming line (PFL) to the load.

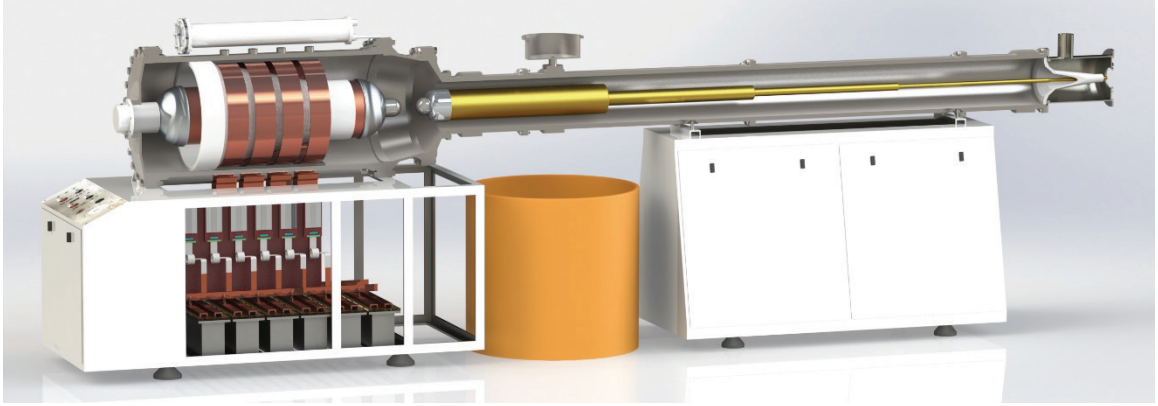


Figure 3.5 SINUS 6 pulsed power driver layout [22].

The switch is made of two brass electrodes capable of maximum pressure of 22 ATM, as illustrated in Figure 3.6. The mechanisms for the discharge and the plasma channel formation are non-deterministic. The spark gap switch has two electrodes made of brass with 4 cm radius and 2 cm distance. It was characterized with a pressure scan to evaluate the voltage and current as a function of pressure.

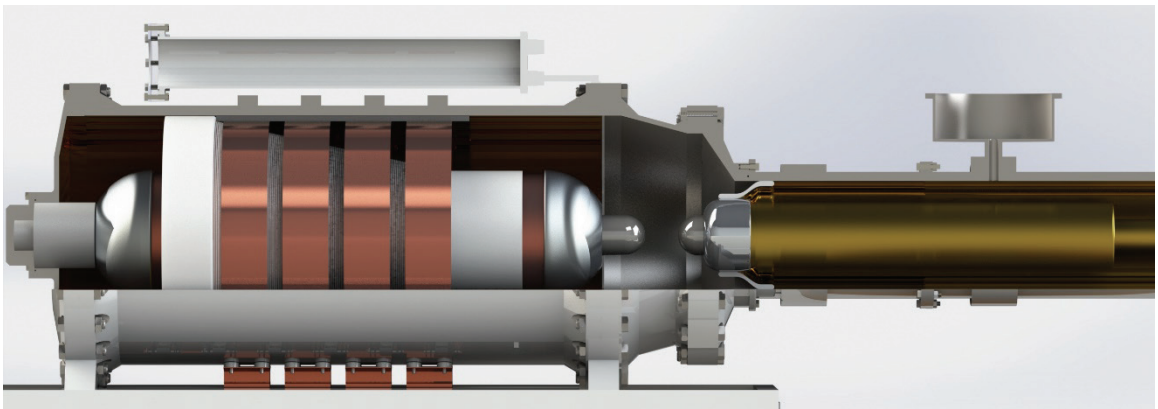


Figure 3.6 SINUS 6 spark gap gas switch [22].

A fast oscilloscope measured the values in Figures 3.7 and 3.8 which display a slight hysteresis behavior.

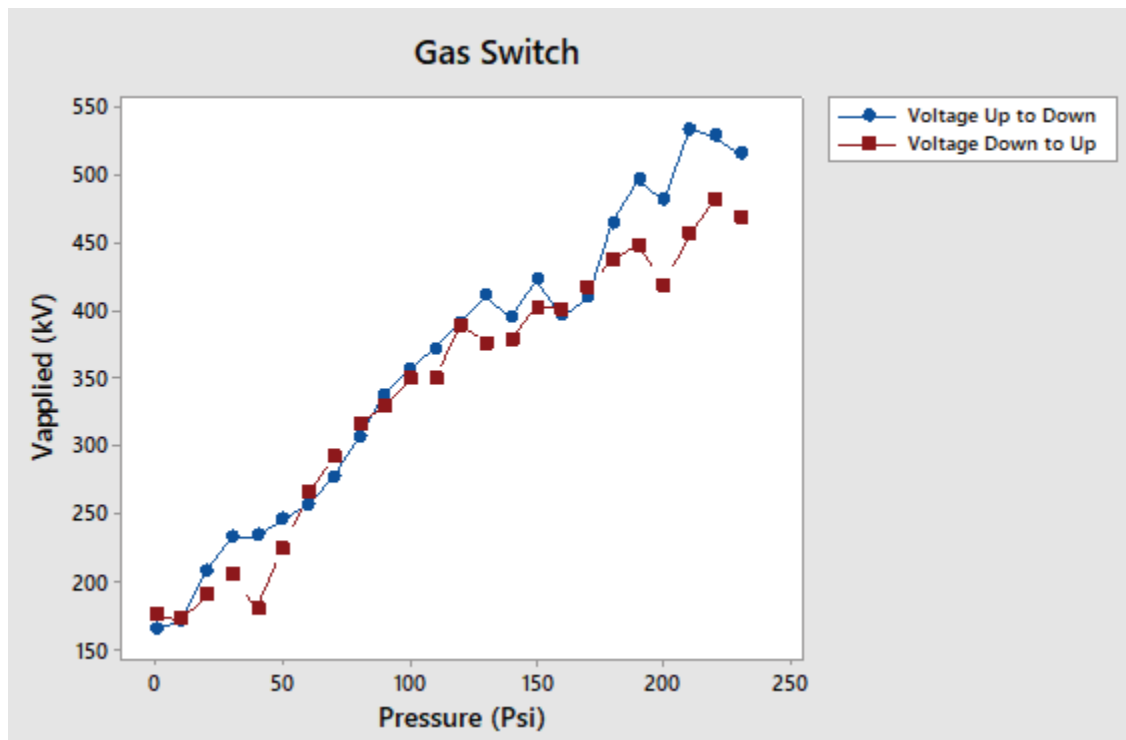


Figure 3.7 Voltage as a function of spark gap pressure.

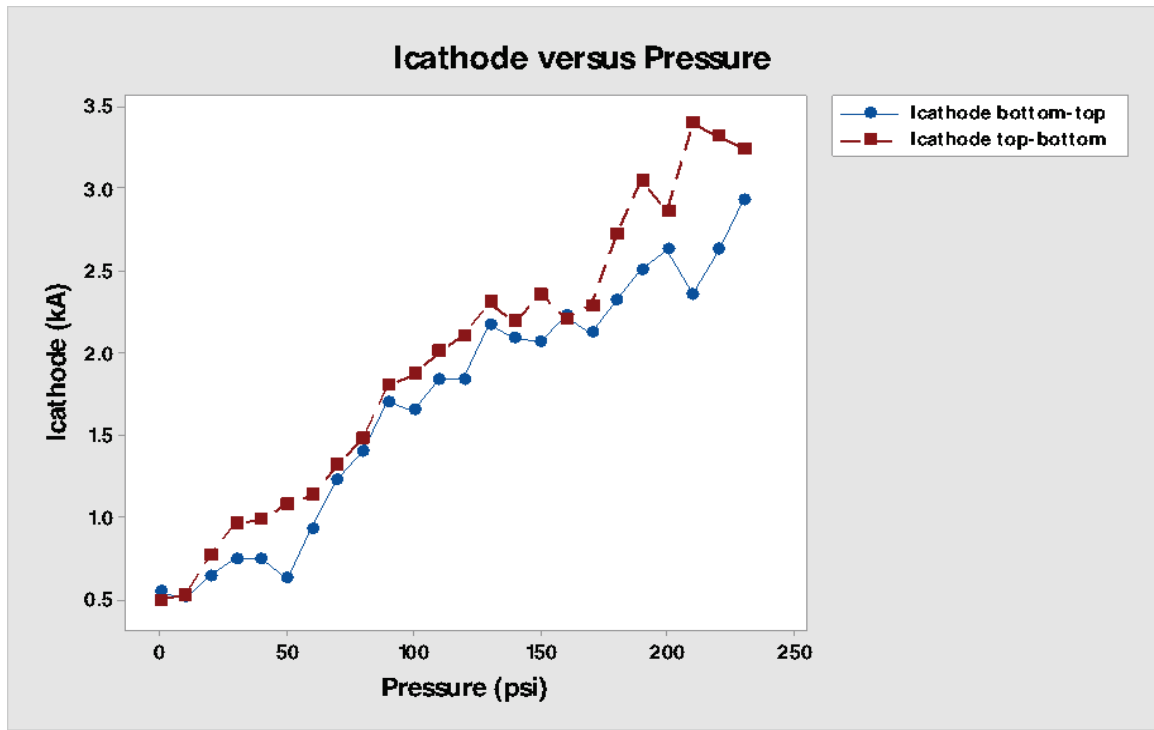


Figure 3.8 Cathode current as a function of spark gap pressure.

A Hall probe characterized the magnetic field along the waveguide for the 9-coil configuration as illustrated in Figure 3.9. A critical requirement for the electron beam propagation along the SWS is a uniform pulsed magnetic field. Another important condition is a sufficient amount of magnetic field lines at both extremes of the solenoid to magnetically insulate the vacuum oil interface and guide the electrons toward the beam collector. One of the constraints during the optimization of the SWS, the length of HPM source, was longer than the waveguide and coil length.

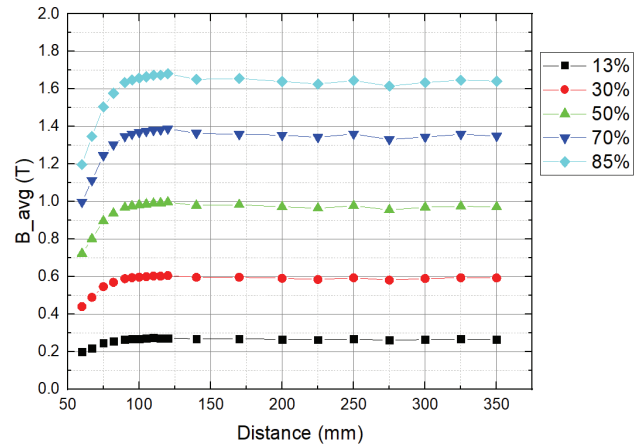
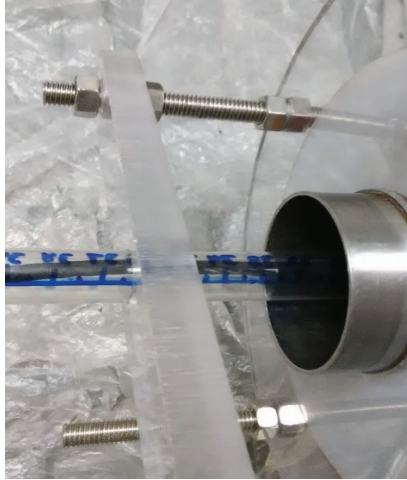


Figure 3.9 Pulsed magnetic field measurement.

3.3 Cold Test Characterization

The test without the electron beam to characterize the MTMSWS is called a cold test. This procedure is performed with the device under test (DUT), and a Vector Network Analyzer (VNA). A sweep in frequency through the DUT gives the operational frequency and the number of resonant frequencies is related to the total amount of unit cells or the periodicity.

Figure 3.10 and 3.11 illustrates the DUT and excitation probe.

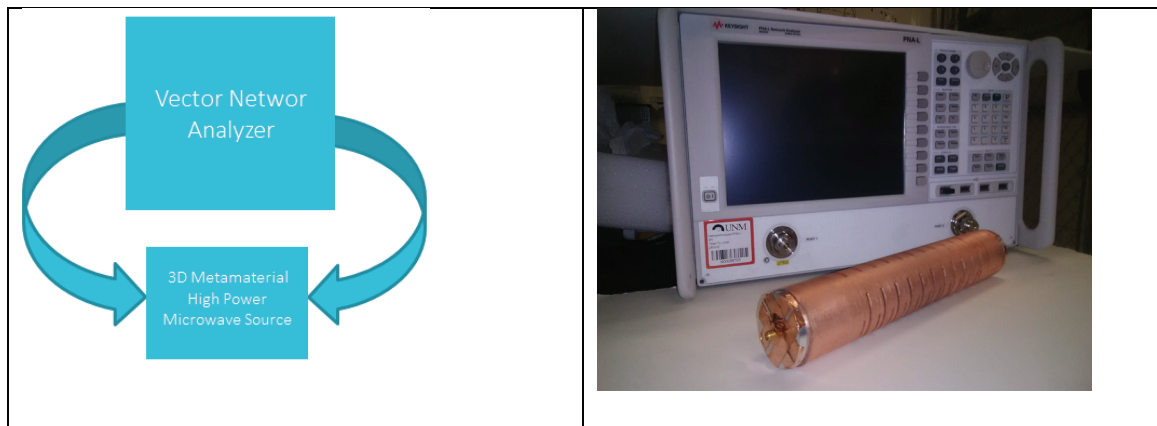


Figure 3.10 Device under test.



Figure 3.11 Excitation probe for the 3D SWS.

The perturbation technique [23] can be used to measure the spatial field distribution of electrical fields inside of a cavity. Initially this procedure was developed to analyze fundamental modes for particle accelerator cavities with Q factor near 4000. Later on, it was adapted to SWSs. Since HPM sources have high fields, the power extraction most of the time is based on open ended structures such as antennas. The mismatches between the parts with lower quality factor produce asymmetrical axial field distribution. This test is the first step to characterize and validate the dispersion curve and the design of the VED before the hot test.

3.4 Frequency Characterization, Power, and Field Mapping

The frequency of the MTMSWS is characterized using an S-band open-ended waveguide detector. To detect the output frequency, signal the waveguide sensor is placed in front of the horn antenna as illustrated in Figure 3.12.



Figure 3.12 Photograph of the RF detector.

The RF signal is measured using a fast oscilloscope and a Python script computes the fast Fourier transform of the incoming electromagnetic wave to give the frequency output. A second sensor, a resistive power detector [24], is aligned 90° towards the antenna and placed 1.3 meters away in the far-field zone.

Figure 3.13 illustrates the layout for a horizontal scan. This methodology measures and records the Poynting vector along a 3D printed arc. The radiation distribution needs to be measured in the far-field to avoid power fluctuations due to the reactive fields.

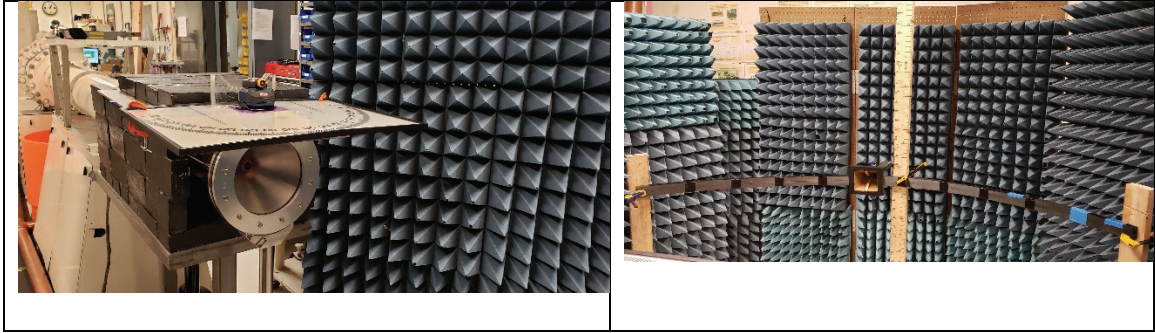


Figure 3.13 RF measurement experimental layout.

The far-field is the minimum distance regarding the antenna aperture and wavelength to measure the field intensity of electromagnetic wave with assurance that you are in the region where the time-average Poynting vector is real. Equation 2.11 approximates this distance. In this region the electromagnetic wave can be considered a plane wave whose field components are perpendicular and angularly independent from the radial distance. The radiation field pattern from a fixed distance recorded the Poynting vector using the resistive sensor along an arc of 120° in 5° steps. Figure 3.14 shows the resistive sensor detector with antenna to measure the power density. Five shots were taken at each position, and the average of maximum peak-to-peak amplitude for five shots at each position plotted peak power versus angular position from the center of the antenna.

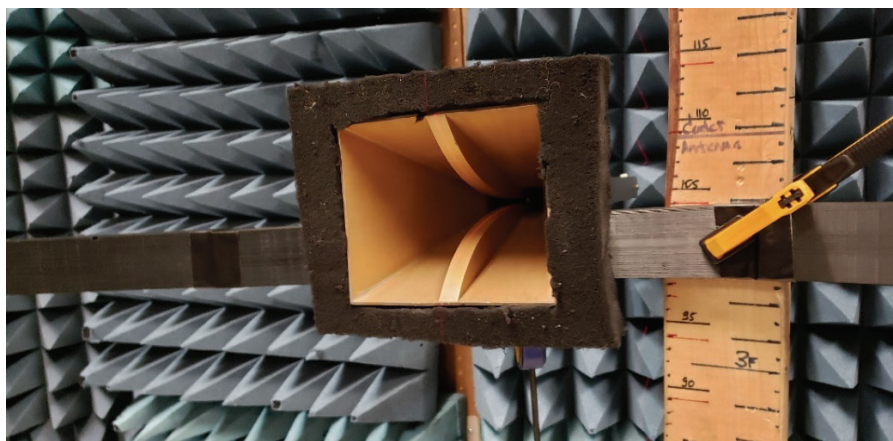


Figure 3.14 Photograph of the resistive sensor used for field distribution measurements.

The electrical field distribution irradiated by a horn antenna is captured using a neon bulb array placed in front of the antenna to register the mode pattern. The intensity of the light is directly related with output RF power from the antenna. The radiation pattern is the geometric distribution of the electric field intensity. This measurement is an accessory diagnostic to evaluate the transverse electromagnetic mode irradiated from the antenna, as shown in Figure 3.15.

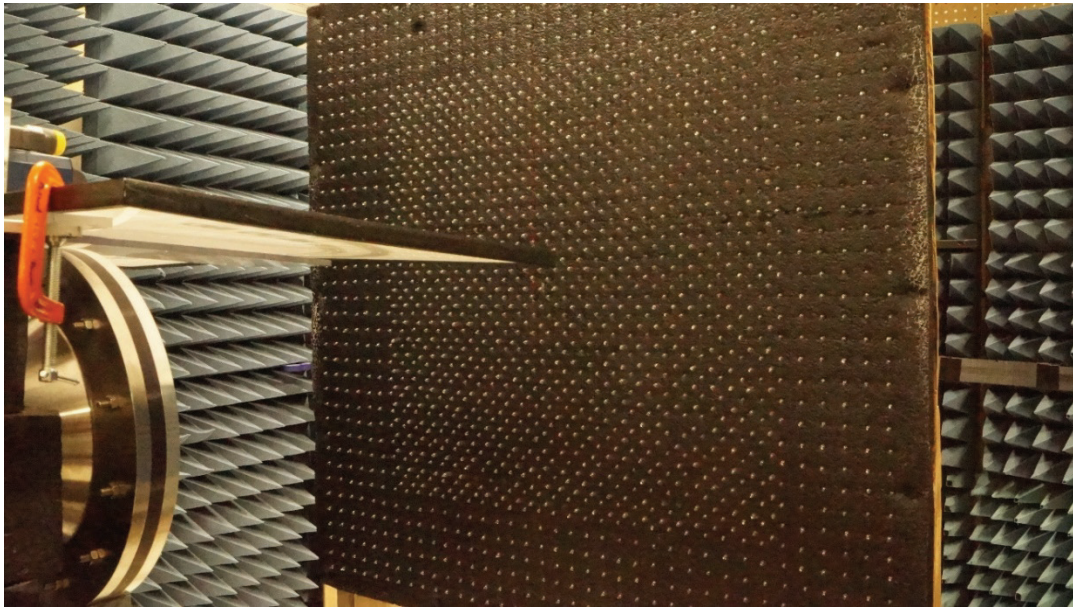


Figure 3.15 Photograph of the neon bulb array for field pattern measurement.

3.5 Optical Diagnostics

HPM sources are very susceptible to voltage and RF breakdown due to local high intensity electrical fields inside MTMSWSs. This phenomenon can cause serious damage to the 3D printed VED. The experimental layout is assembled using an SLR camera and mirror to investigate the light coming out from the HPM horn antenna as illustrated in Figure 3.16. This light coming out from the antenna describes the interaction of the relativistic electron

beam propagating within the SWS and dumping in the collector for the beam generated by explosive electron emission (EEE) from the cathode.

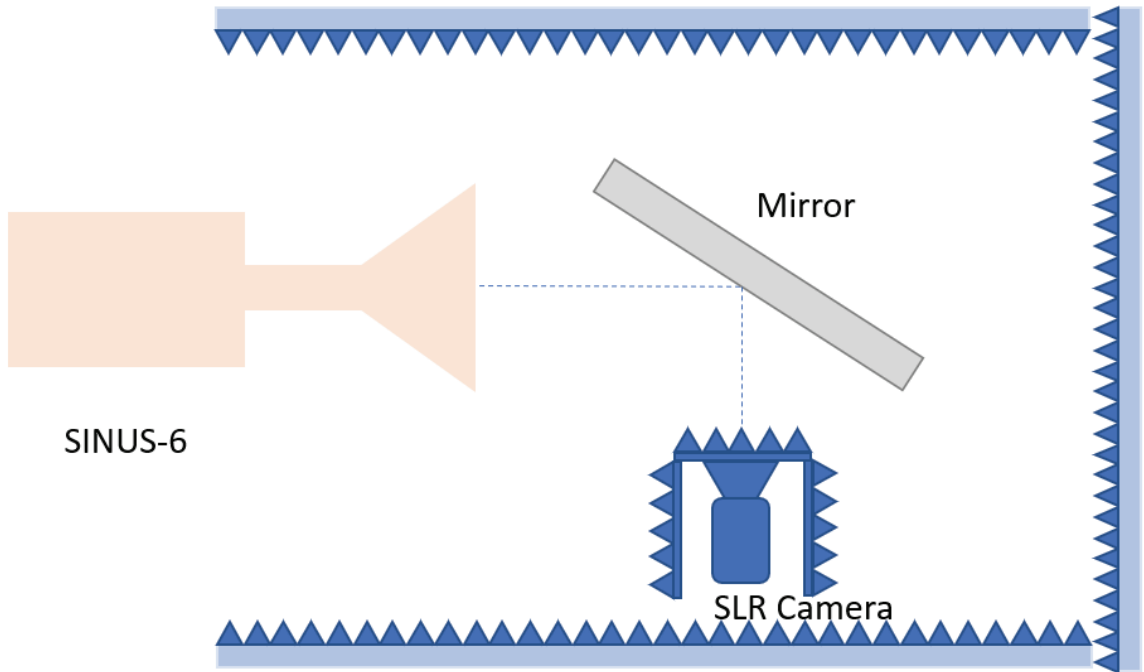


Figure 3.16 Optical diagnostics schematic for visible light emission.

The beam collector is part of the 3D printed SWS and its coaxial feed to the HPM horn antenna as illustrated by Figure 3.17. An open shutter exposure for 1.6 seconds and ISO 3200 will capture the intensity of light in time-integrated measurements.

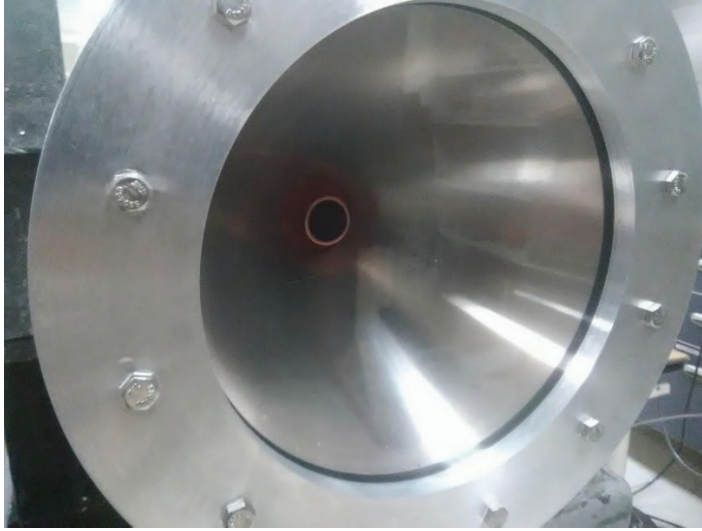


Figure 3.17 HPM antenna output.

4 CHAPTER 4: RESULTS

4.1 Fundamentals of Computer Simulations

Before the process of manufacturing the MTMSWS, a series of computer simulations [25] regarding cold tests using the eigenmode solver, frequency domain, and PIC simulations were performed using CST Particle Studio. The main objective was to evaluate the RF characteristics through virtual prototyping according to the boundary conditions for the best prototype to be manufactured.

The computational power allows nowadays the user to simulate the VED as close as is possible to “the real world”. This is a breakeven point regarding the production of HPM sources. Since the beginning, most of the time researchers in the field used a basic approach to design and then manufacture the device. As a result of poor computational power, it was common to design and manufacture numerous structures due to uncertainties in calculations. Following advances in PIC and electromagnetic simulation tools, this gap between experiment and theory became shorter. This led to economy of time, material, and production cost.

An era led by experimentalists came to an end, and virtual prototyping emerged as the tool to push researchers to design new HPM structures on the computer. Nevertheless, experimentalists are still necessary because experiments validate computer simulations.

4.2 Simulation Results

Computational results from simulations regarding an optimized MTMSWS were performed by the UCI and UNM's Pulsed Power, Beams, and High-Power Microwave Laboratory. For both the electromagnetic solvers and PIC simulations the model was fully 3D.

The simulation results are classified as cold test and PIC. The first, regards the computational of electromagnetic solvers without the relativistic electron beam. The second is a combination of the pulsed electron beam generated by EEE from a cold cathode which feeds the VED. The purpose of the PIC code simulations is to compute the physical behavior of the source self-consistent with the boundary conditions incorporating space charge. Due to the cylindrical geometry for the degenerate band edge oscillator (DBEO) the transverse magnetic mode is the most suitable configuration to generate the RF. Figure 4.1 illustrates a unit cell for analysis.

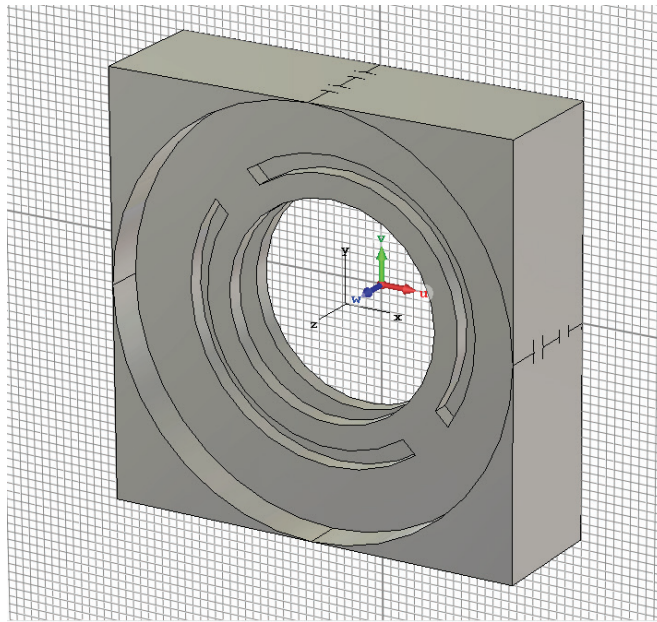


Figure 4.1 A unit cell of the MTM CSSR.

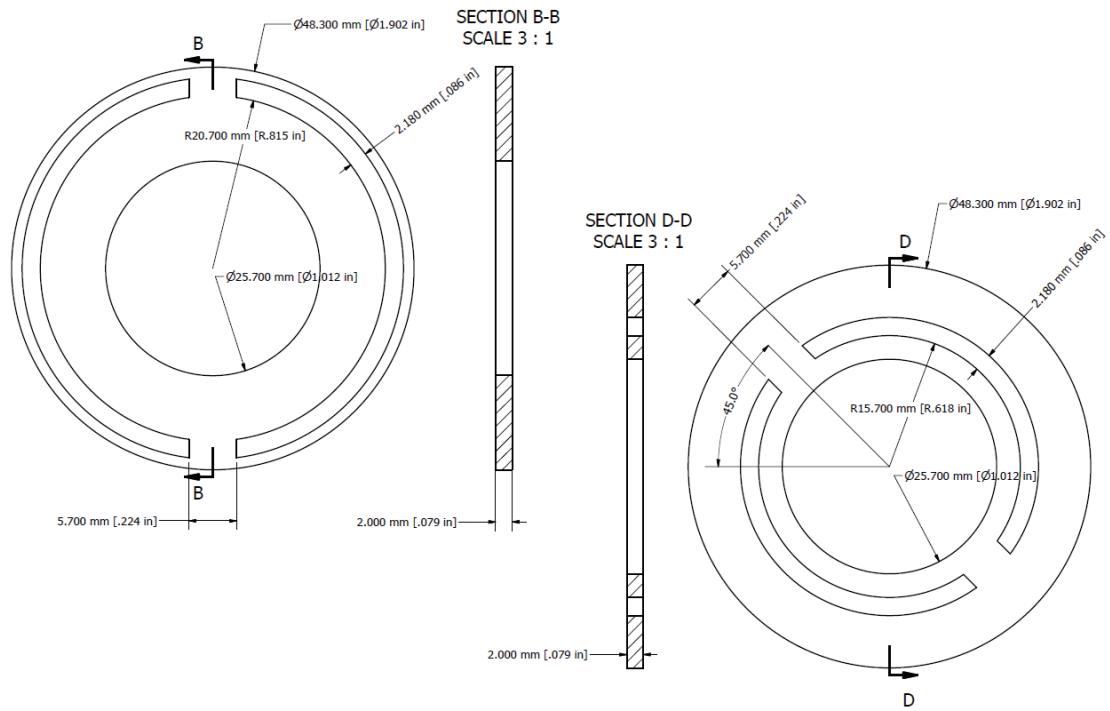


Figure 4.2 MTM's dimensions.

4.3 Eigenmode Solver

The specific geometry and configuration of the slots of the disks and dual arrangement permit a mixing of modes and generation of degeneracy. Figure 4.2 illustrates the dispersion curves with the band stop for a single cell.

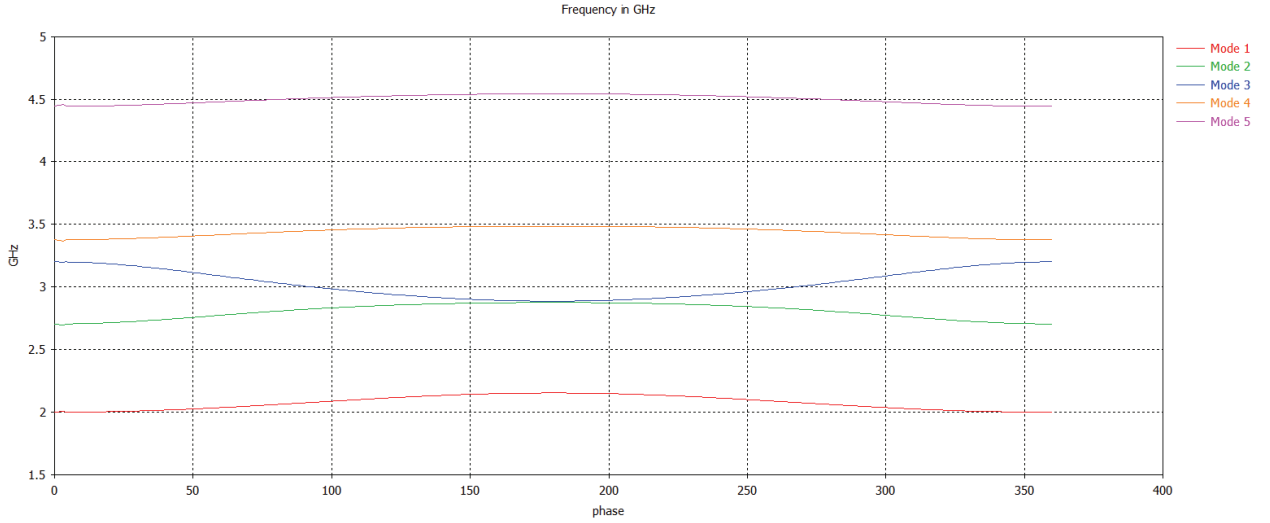


Figure 4.3 Dispersion characteristics for a single cell of the MTMSWS.

The distribution of modes indicates almost a single point of overlap. As is illustrated in Figure 4.3, the minimum stop band between modes 2 and 3 is 11 MHz and the maximum is 91 MHz. Considering the theoretical operation frequency of 2.88693 GHz the difference at maximum is 3.15% and minimum 0.4%; such values indicate a practical overlap between the modes, condition for the phases 120° and 180° . The advantage of forcing the degeneracy for this case where the polarization angle of the rings are rotated 45° is to decrease the group velocity to practically zero forcing a “frozen mode” [26]. This would benefit the exchange of energy between the electron beam and the electromagnetic wave.

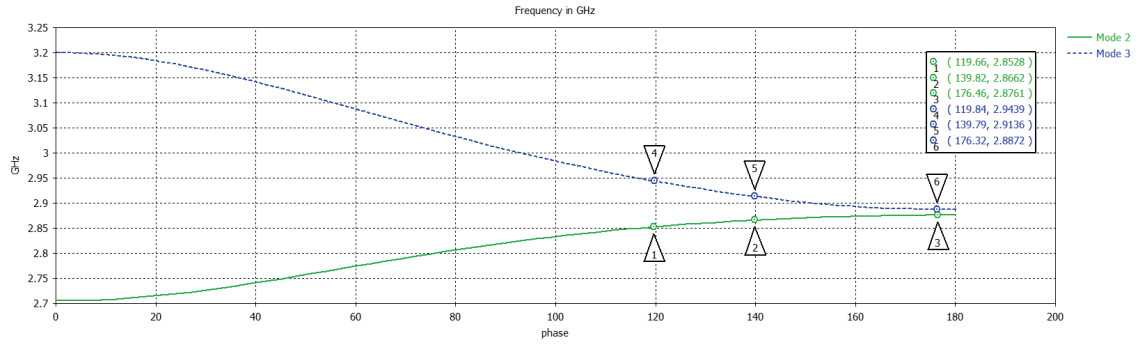


Figure 4.4 DBEO modes.

From Figures 4.2 and 4.3 it is possible to affirm that the SWS is a high order eigenvalue structure. Theoretical calculations and simulations indicate that the cutoff frequency for a hollow waveguide dimension is 3.6 GHz as is indicated from the dispersion curve in Figure 4.4.

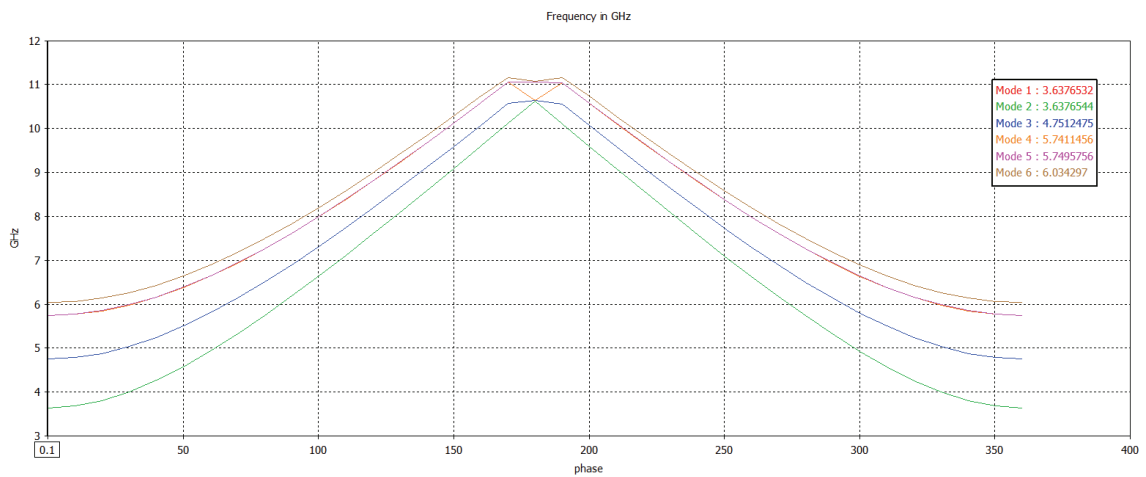


Figure 4.5-Mode dispersion for hollow waveguide

Table 4.1 presents the cutoff frequencies for TE and TM modes for a hollow waveguide with 24 mm radius.

Table 4-1 Cutoff frequencies for a hollow waveguide of 24 mm radius.

Mode	Frequency (GHz)
TE₁₁	3.6
TM₀₁	4.78
TE₂₁	6.07

The frequency of operation for this waveguide is below cutoff, as described in the paragraphs below. From the eigenmode solver simulation the dominant mode inside of the SWS is the TM₀₁ mode. In addition, the third eigenvalue has the operational frequency of oscillation as shown in Figure 4.5. Thus, this is a high order eigenmode structure.

A single cell simulation in cold test showed two eigenvalues close in frequency to the resonant frequency of the unit cell. In both cases the resonance is below the cutoff frequency of the waveguide. Thus, this characteristic demonstrates a MTM property for the CSRRs. This is one of the advantages for using MTMs to create RF oscillators. Moreover, the field distribution inside the unit cell is shown in Figure 4.5. It is interesting to note that eigenvalue 2 (left side) has an asymmetry for field distribution and a lower cutoff. Nevertheless, the dispersion curves from Figure 4.3 showed a degeneracy at a single point of operation.

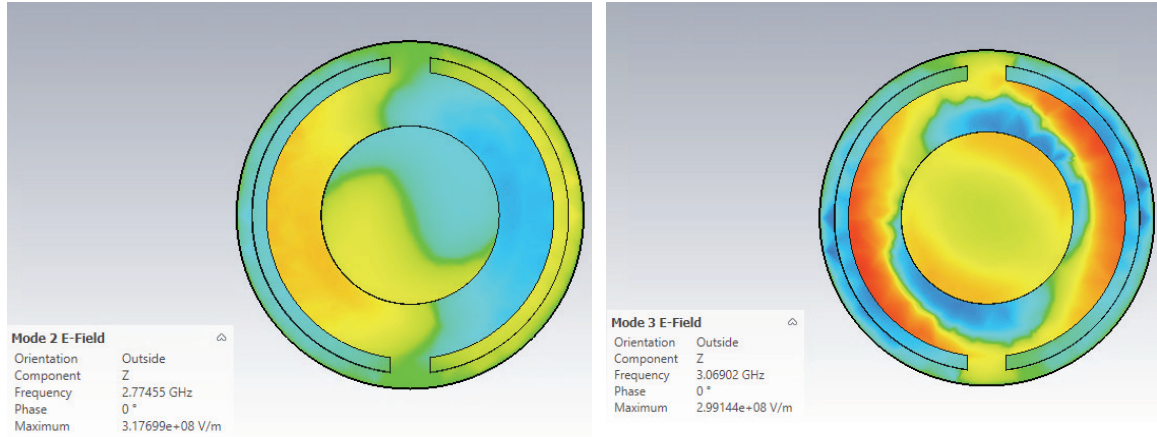


Figure 4.6 Field distribution inside of a unit cell of the MTMSWS [27].

The transverse magnetic field distribution from Figure 4.5 indicates a TM_{01} -like mode. This configuration is interesting because it has a strong E_z component allowing a strong interaction between the structure and the electron beam.

A section view along the x-axis from Figure 4.6 presents the electric field distribution with more detail. This was a result of the boundary conditions which created the dominant mode, TM_{01} , with a field distribution capable of propagation along the SWS. This mode excited a frequency of 3.0 GHz inside the unit cell.

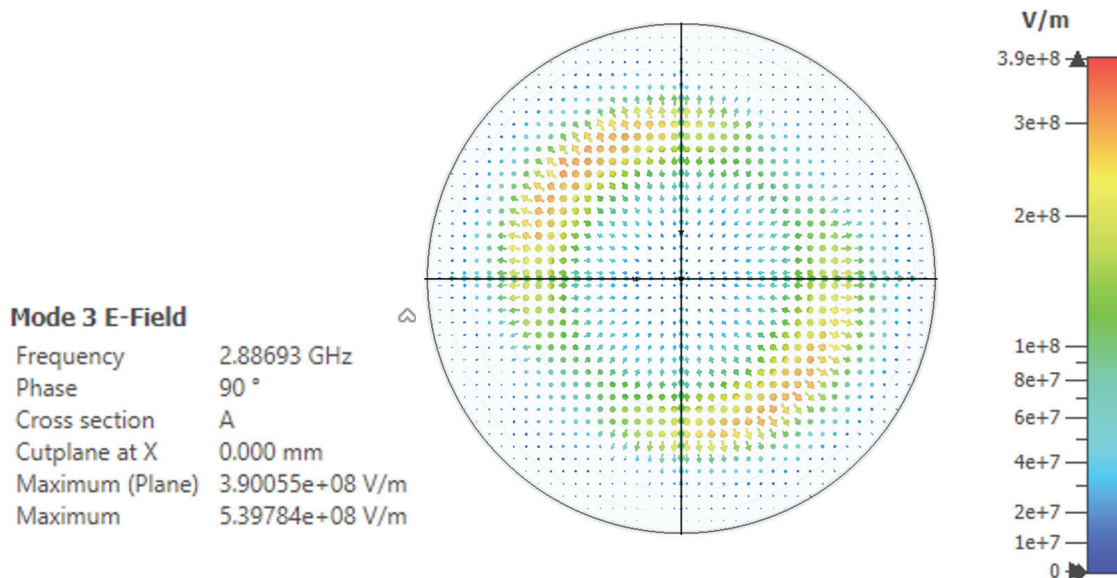


Figure 4.7 Mode 3 E field distribution from TM_{01} .

Figure 4.7 illustrates regions with high intensity electric fields. Later, PIC simulations will show points along the SWS where very high electrical fields are present.

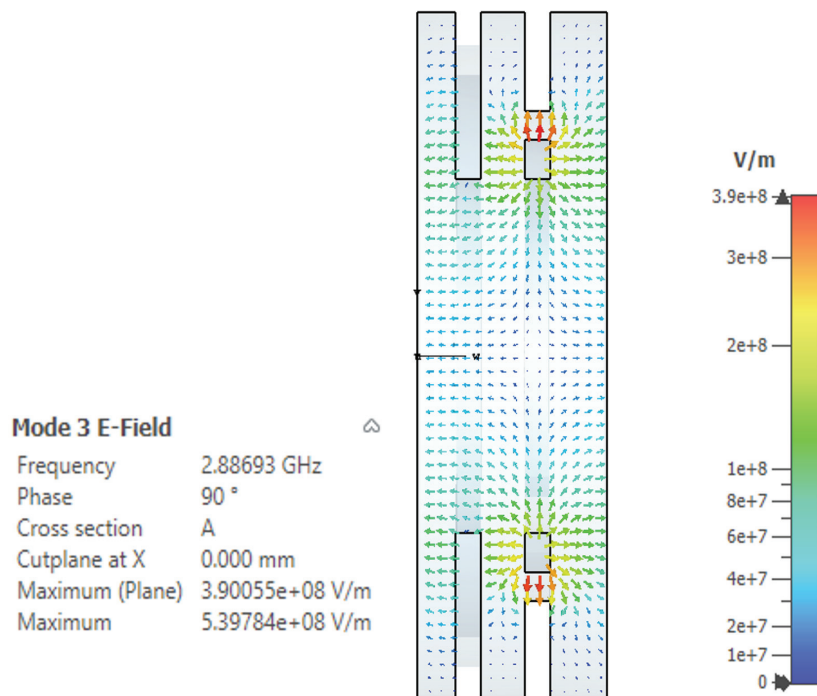


Figure 4.8 Mode 3 E Field distribution z-axis for TM_{01} mode.

The unit cell model for the H field describes a radial configuration with high field values close to the edge due to high frequencies and lower fields due to lower frequency, as is illustrated in Figure 4.8 above. The magnetic field lines from Figure 4.9 describe the TM_{01} mode. In addition, the coupling between the ring slots are strongly dependent on the intensity of the magnetic field generated inside of the unit cell.

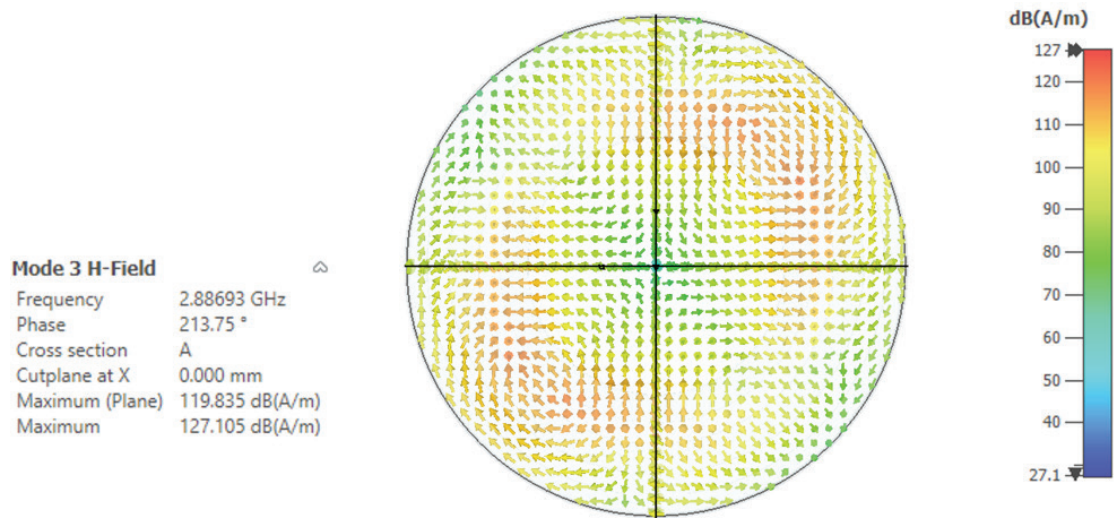


Figure 4.9 Mode 3 magnetic field distribution for the TM_{01} mode.

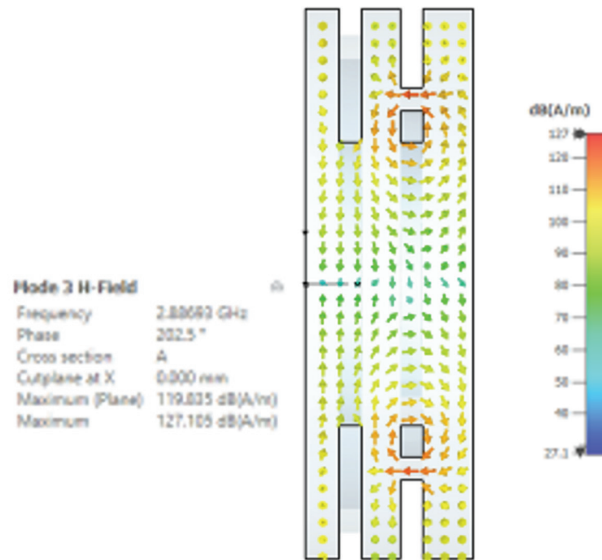


Figure 4.10 Unit cell H-field z-direction distribution for the TM_{01} mode.

The fields inside the cavity can be expressed in terms of the tangential component of the electric field and the normal component of the magnetic field at the slots which are cut in the disks. Because the slot width is much smaller than the wavelength, it can be approximated that the electric field lines in the vicinity of the slot are perpendicular to the longitudinal dimension of the slot. This led to pure TE or TEM waves propagating from the slot. It is not part of this thesis study, but the slot can be modeled as a transmission line from its electrical properties.

The current which flows along the slot is proportional to the normal component of magnetic field at the slot. In addition, a longitudinal component of the magnetic field is created associated with the normal magnetic field at the slot. As a result, this longitudinal component is responsible for a shunt inductance across the slot, shift of the resonant frequency of the slot, and changing the coupling factor from one slot to another.

Another important characteristic for the cold test is the coupling impedance of the structure. When the electron beam velocity and electromagnetic wave phase velocity are synchronous the *Pierce parameter* provides insight into the coupling [28]. This value represents the capability with which the SWS can harvest energy from the electron beam to generate RF power. In the case of the O-Type device under study the operating frequency in a hot test is expected to be near 3.0 GHz and the coupling impedance is 134.48 Ω . This value is close to other structures found in the literature [28].

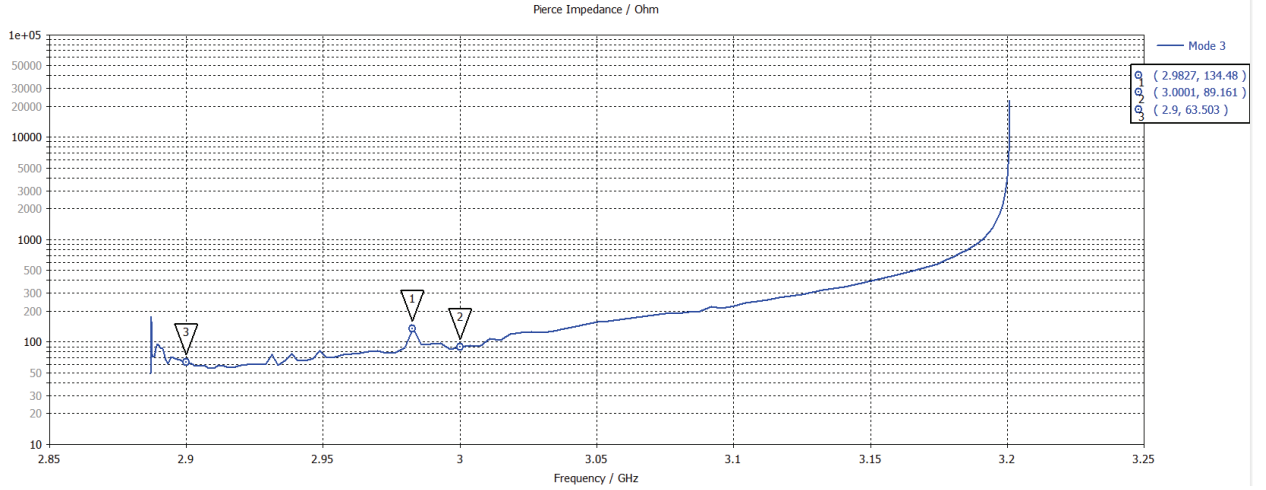


Figure 4.11 Coupling impedance as a function of frequency.

It is important to note that the coupling impedance is basically dependent on the geometry of the electron beam and the SWS. In this case, as told in Section 3.1, misalignment between them can cause change a serious change in the *Pierce parameter*.

The operating mode is verified using the dispersion curves plotted with the beam line in Figure 4.11. According to the intersection of the dispersion curve and beam line, the operating frequency is expected to be near 3 GHz for the TM_{01} mode.

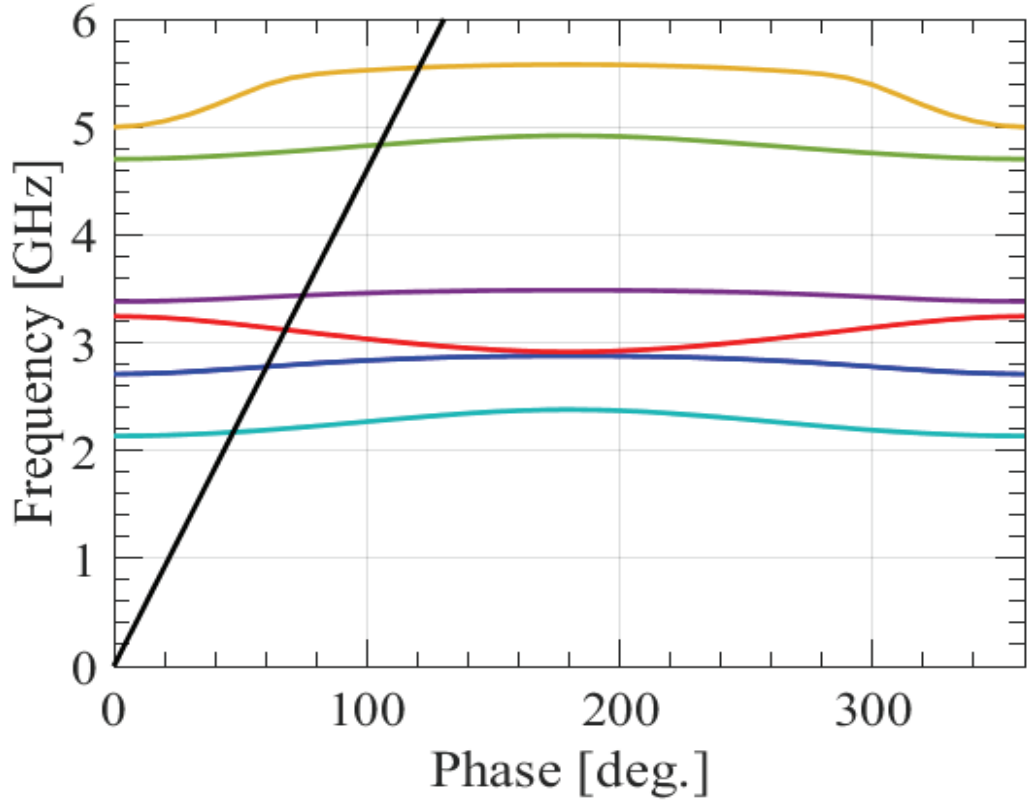


Figure 4.12 Dispersion curve with the beam line for an electron beam voltage of 400 kV [27].

When an electron beam is introduced into the VED it is expected that there will be a shift in the operating point from the intersection of dispersion curve and beam line. Moreover, if the voltage is reduced to 200 kV the effect of degeneracy will improve [27].

4.4 Frequency Domain Solver

One of the exotic properties of MTMs applied to waveguides is below cutoff propagation. Regarding this issue the left-handed material exhibits negative permittivity and permeability, as presented in Chapter 2, Figures 2.14, and in Chapter 4 Figures 4.11 and 4.12, which illustrated these characteristics. The results from a frequency domain solver simulation in Figures 4.12-13 validated the DNG property for the SWS in this thesis. It is

important to notice that this feature highlighted with the markers in Figures 4.13 and 4.14 is appears at a frequency near 3 GHz.

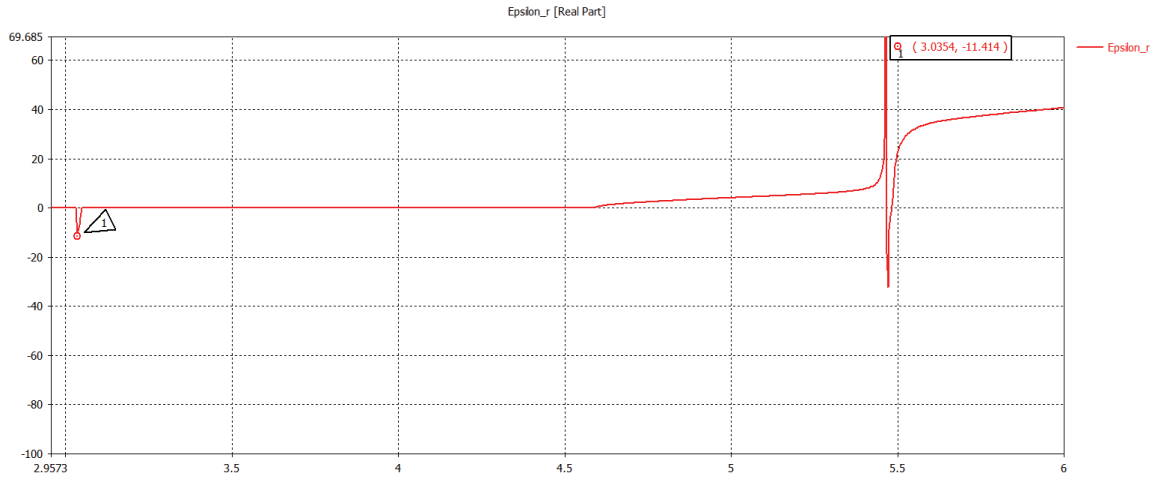


Figure 4.13 Negative permittivity.

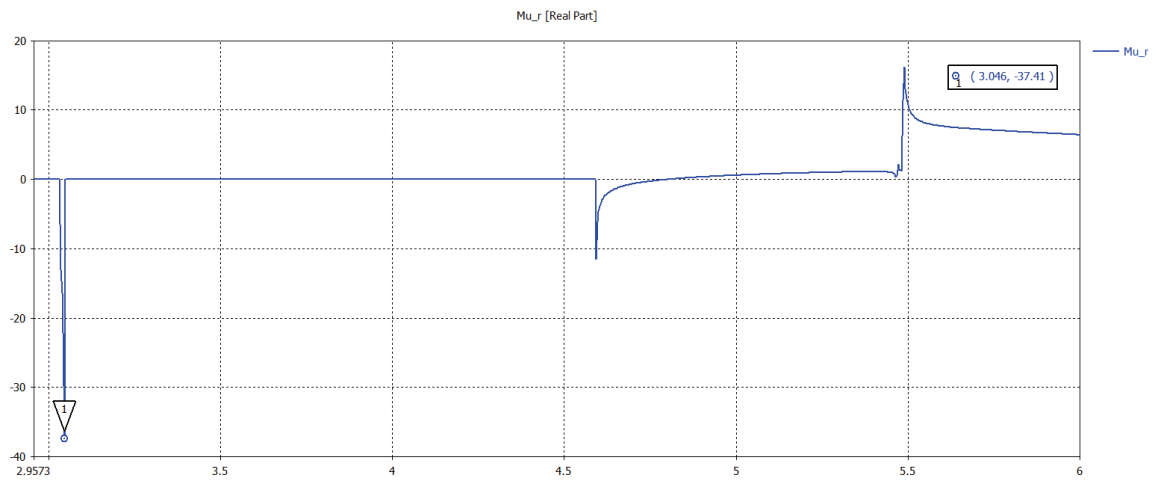


Figure 4.14-Negative permeability

A negative dispersion characteristic from Figure 4.3 at the operating frequency shows TM-like mode behavior due to the E_z component being stronger than the H_z component. The field distribution for this structure was shown in Figure 4.4.

The simulation result for a hollow waveguide with 48.3 mm diameter indicates a cutoff frequency of 4.78 GHz. The DNG aspect of the waveguide decreased the diameter by 59.3%. This reduction is evidence that the permittivity and permeability are negative.

4.4.1 Experimental Results from the Vector Network Analyzer

The characterization of the 3D SWS using a VNA is part of the cold test procedure prior to hot test evaluation. Moreover, it was possible to generate several distinct frequencies for the 3D SWS due to the probe excitation, as shown in figures 4.14-16. The since the probe inside of the DUT was not perfect perpendicular, a non-uniform excitation for TM_{01} of the mode generated frequencies below and above the cutoff.

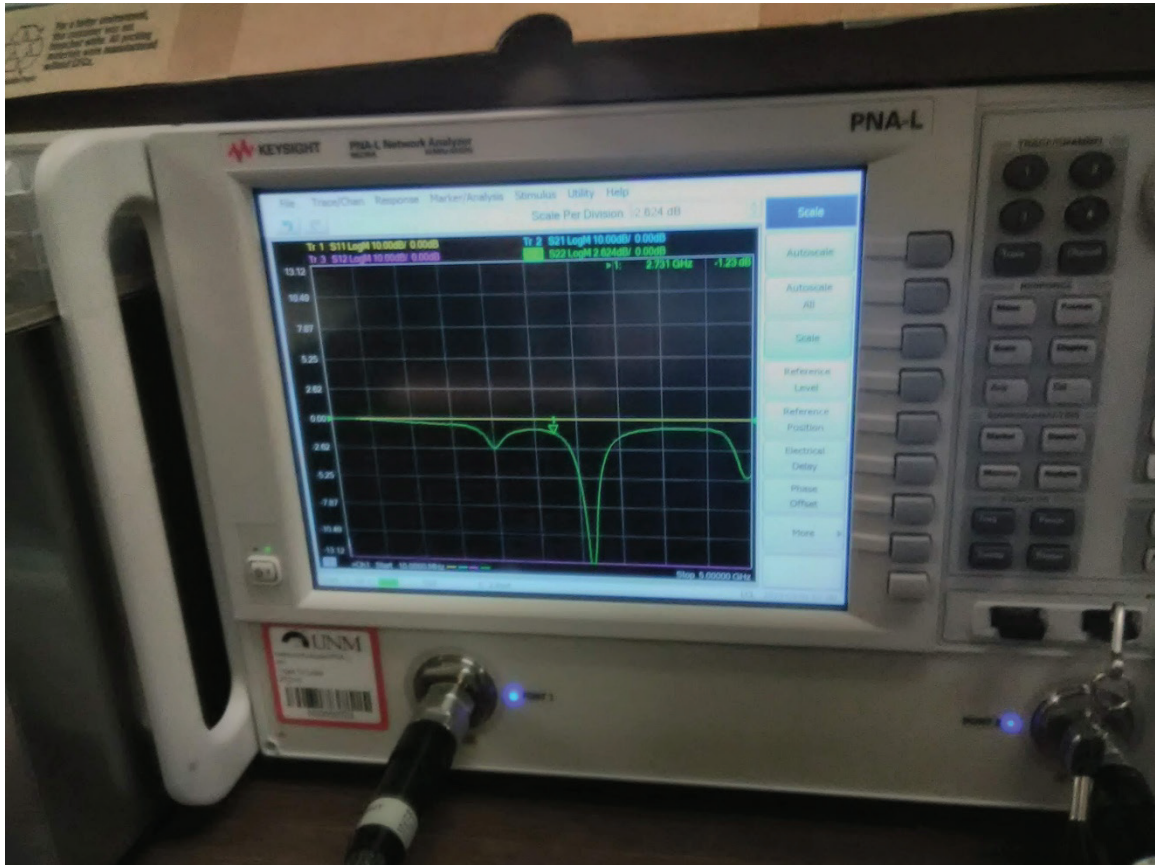


Figure 4.15 Mode 2 excited with S_{22} at 2.731 GHz regarding TM_{01} .



Figure 4.16 Mode 3 excited with S_{22} at 3.38 GHz TM_{01} .

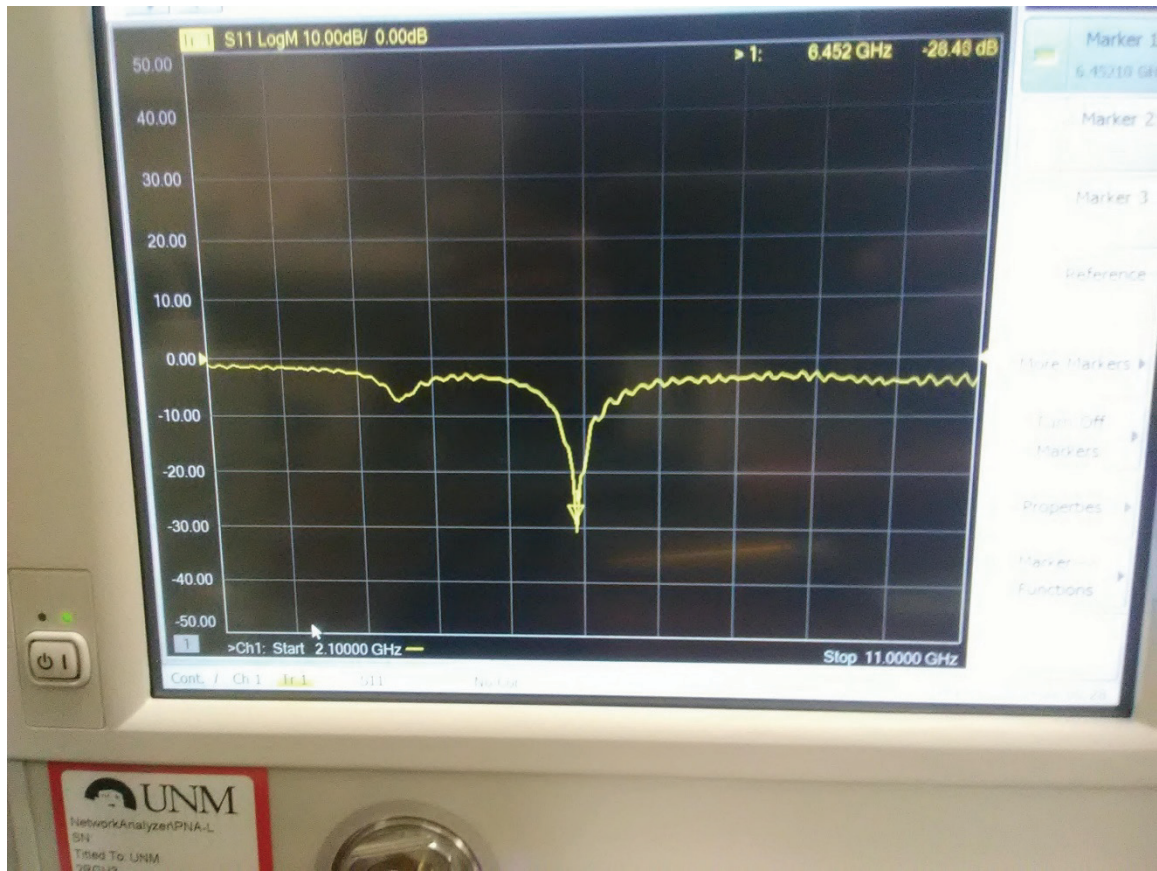


Figure 4.17 Higher order mode, which needs further investigation.

A higher order mode appears at a frequency of 6.452 GHz. This will be discussed later in the following section for PIC CST-SINUS simulations and in hot test experimental results, where a second harmonic close to this value was noticed.

4.5 Particle-in-Cell Simulation

Using a set of PIC codes such as CST, MAGIC, and ICEPIC MTMSWS hot test simulations were performed in order to compute the RF output power, voltage, cathode current, and frequency and establish a benchmark [29].

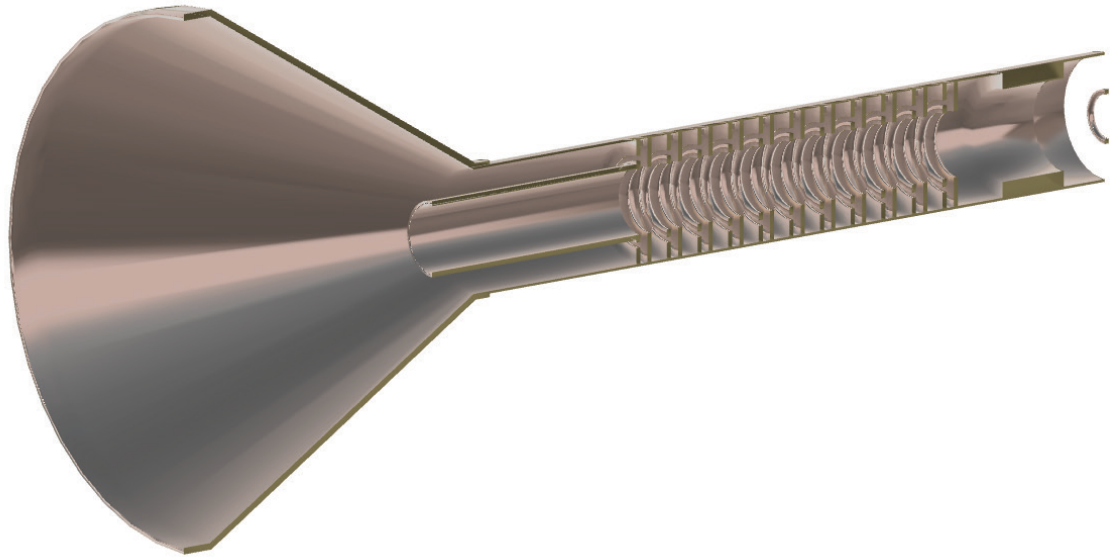


Figure 4.18 3D Printed MTMSWS with antenna.

4.5.1 PIC Simulation for 400 kV

The initial parameters for the CST simulations were an applied voltage of 400 kV and a magnetic field of 2T according to previous reports from UCI for a risetime of 5 ns. After several PIC simulations it was noticed that the applied voltage could be increased regarding the new physical dimensions for the ring slots and gaps. Figures 4.18-4.21 describe the voltage, current, RF power, and frequency for the UCI structure driven by an annular electron beam in CST simulations.

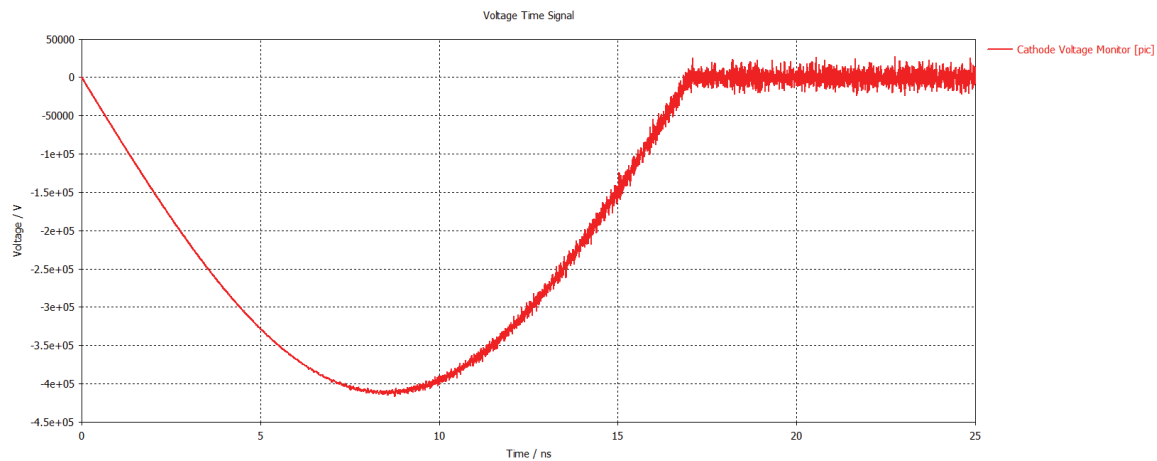


Figure 4.19 Cathode voltage.

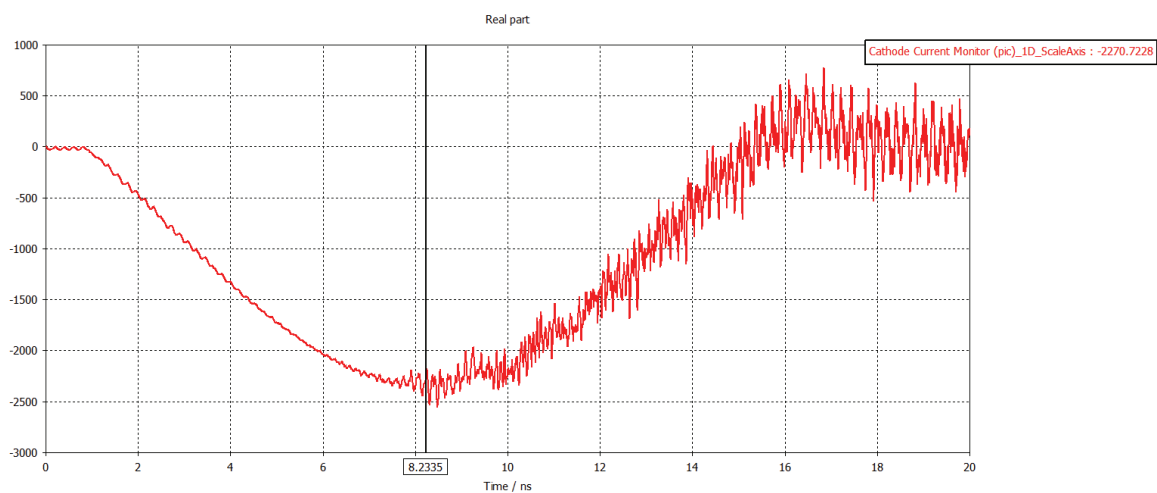


Figure 4.20 Cathode current.

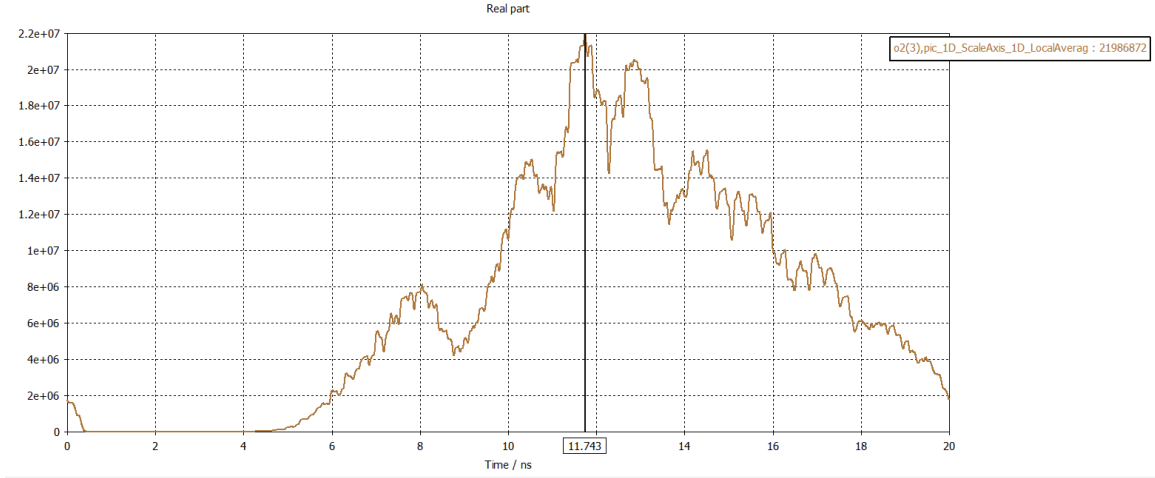


Figure 4.21 Output RF power.

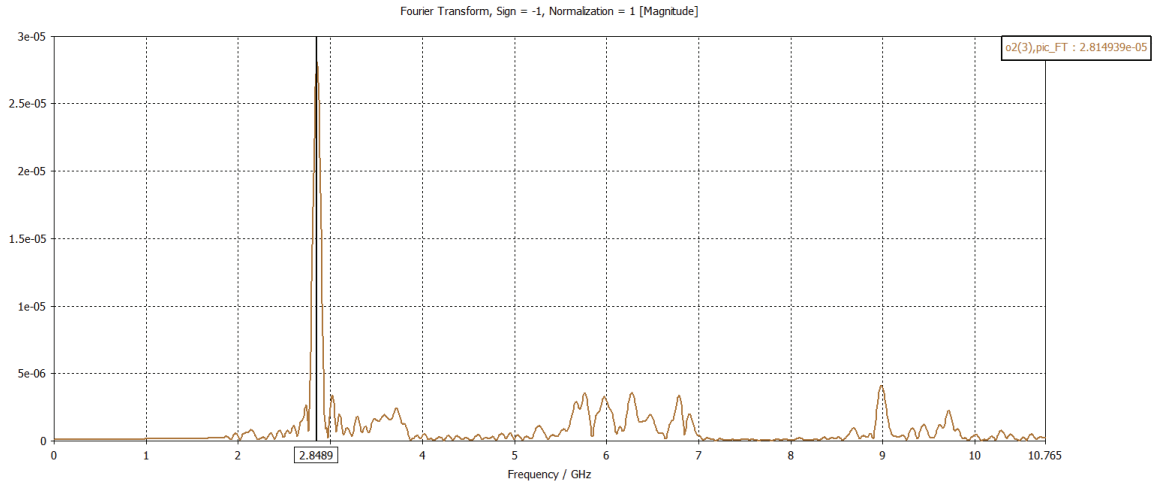


Figure 4.22 FFT of the output electric field.

The purpose of the PIC code is to simulate as close as possible the physics of the HPM source in the real experiment. As noted in the UCI report [11], the RF output pulse in Figure 4.20 has some reflections due to multiple resonances generated inside of the SWS. From Figure 4.11 the intersection of the beam line with the dispersion curve theoretically indicates an operating frequency nearby 3.1 GHz. This is different because when the beam travels through the full structure it shifts the operating point that of a unit cell.

Further investigations into the electrical field distribution inside of the MTMSWS revealed some “hot spots,” regions with very high electric fields. These hot spots were located at the inner slots of the CSSR.

In order to verify CST PIC code simulation results, the HPM source was modeled in MAGIC and ICEPIC. A second set of PIC simulations are presented in Figures 4.22-4.24.

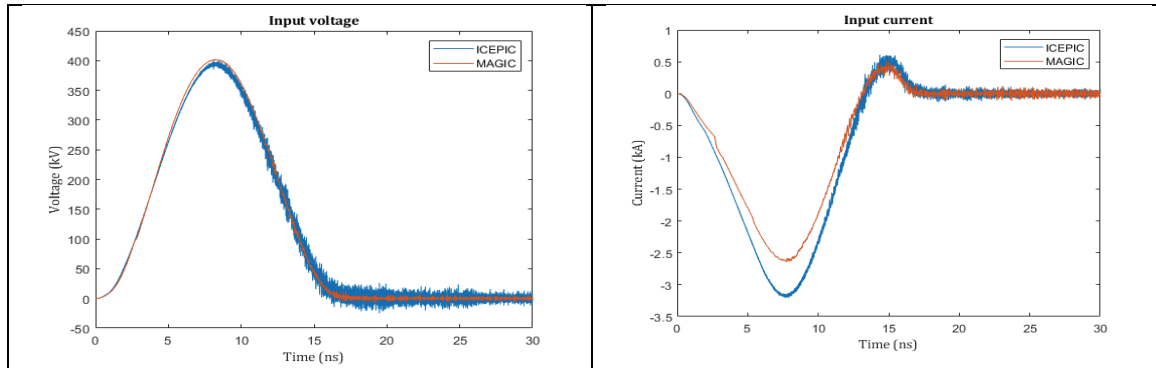


Figure 4.23 PIC voltage and current waveforms from ICEPIC (blue line) and MAGIC (orange line).

The waveforms for RF output power from Figure 4.23 almost overlap. This demonstrated a high degree of convergence for both codes regarding the calculation of power.

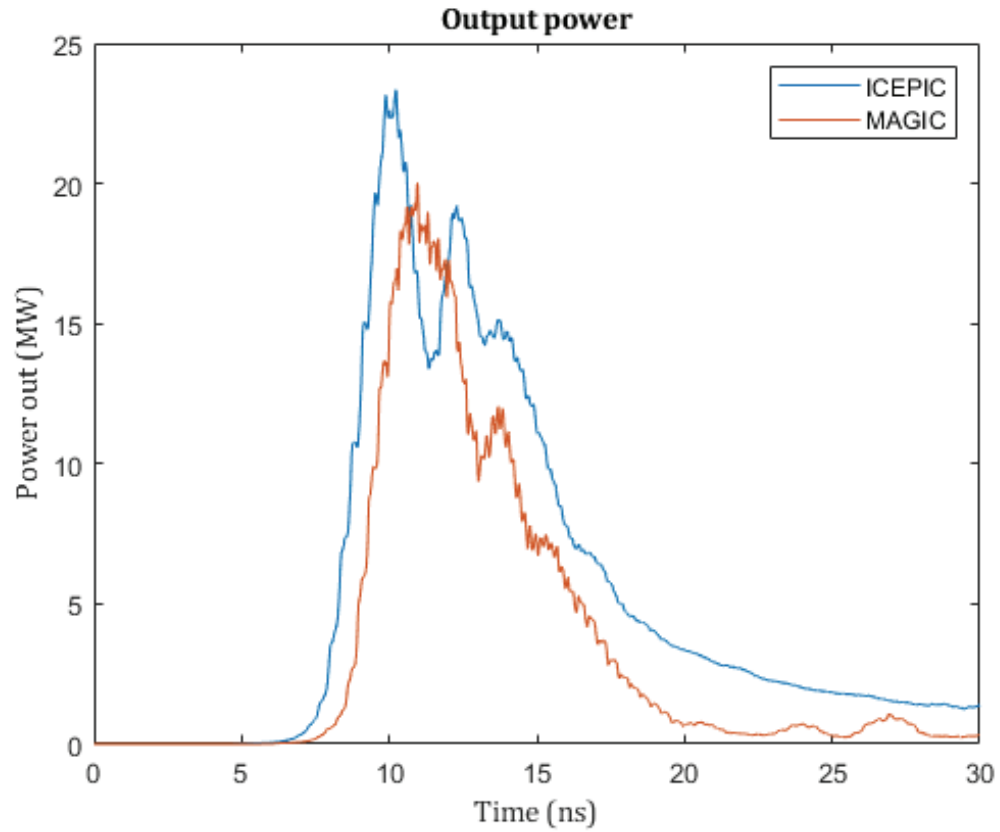


Figure 4.24 Output RF power comparing ICEPIC (blue line) and MAGIC (orange line).

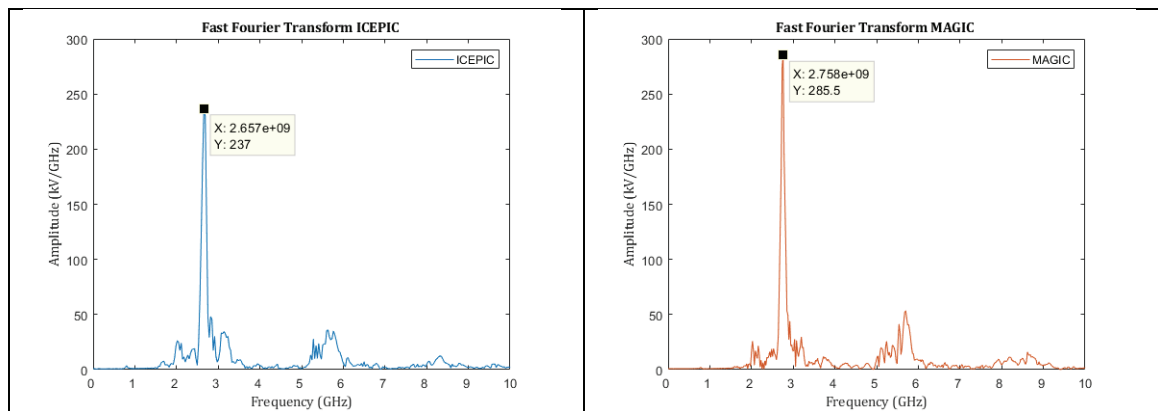


Figure 4.25 FFT of the electric field in ICEPIC (blue line) and MAGIC (orange line).

Table 4-2 Comparison between PIC codes.

PIC CODE	Voltage (kV)	Current (kA)	Frequency (GHz)	RF Power (MW)
CST	400	2.27	2.84	22
MAGIC	400	2.60	2.75	20
ICEPIC	400	3.20	2.67	22

Table 4.2 indicates agreement between the codes regarding frequency and power within 10% of variation. Considering CST as a reference, the efficiency of the system is 9.51%, which is 1.2% higher than the UCI reports. It is also important to note that the second harmonic observed is negligible for all cases. The formation of the second harmonic in RF FFT will be investigated in the following simulations. The crosscheck of the simulation results with different PIC codes validated the CST, since MAGIC and ICEPIC were stable.

4.5.2 PIC Simulation for 490 kV

Our goal is to optimize the performance of the MTMSWS which in experiment is a 3D printed structure. To increase the energy of the particles accelerated it is important to consider the effects of space charge. In this condition the space-charge-limited current is 3.8 kA and the Fedosov current emitted from the cathode is 2.87 kA.

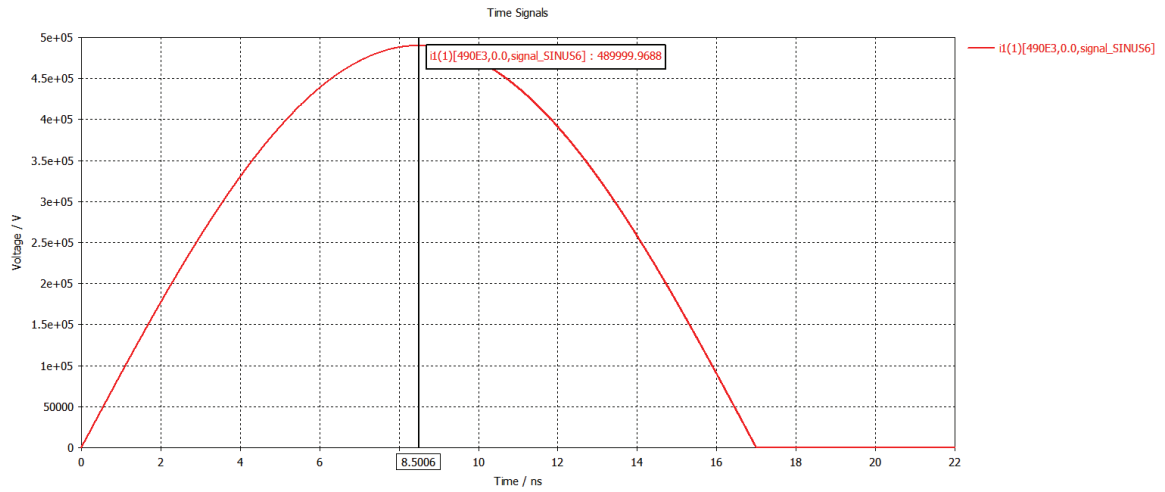


Figure 4.26 SINUS voltage waveform in PIC simulations.

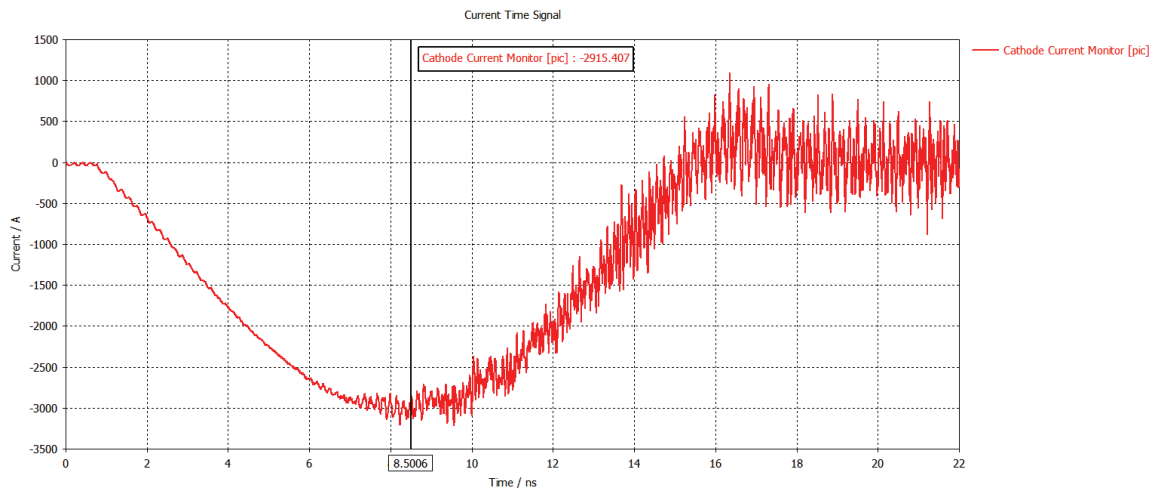


Figure 4.27 Cathode current from SINUS in PIC simulations.

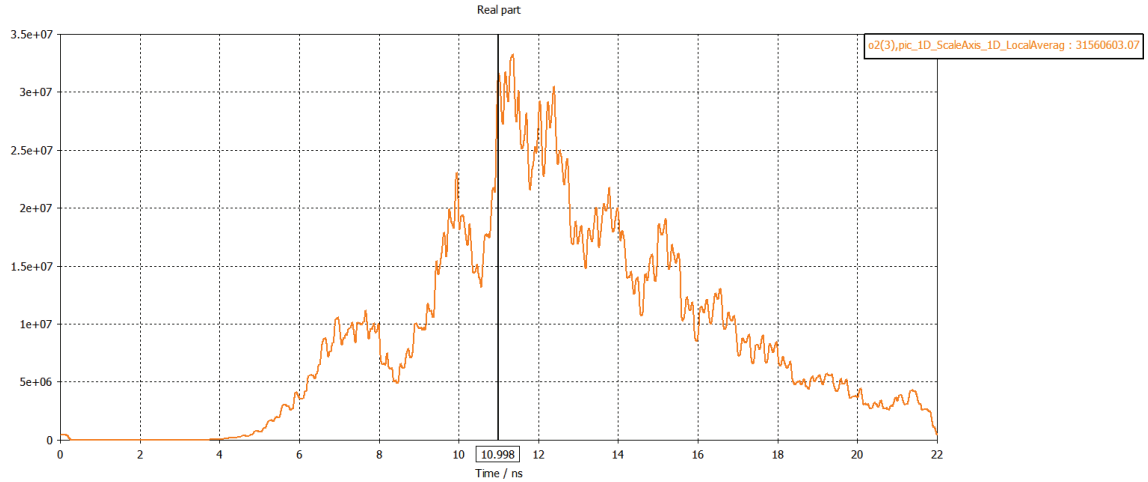


Figure 4.28 Output RF power.

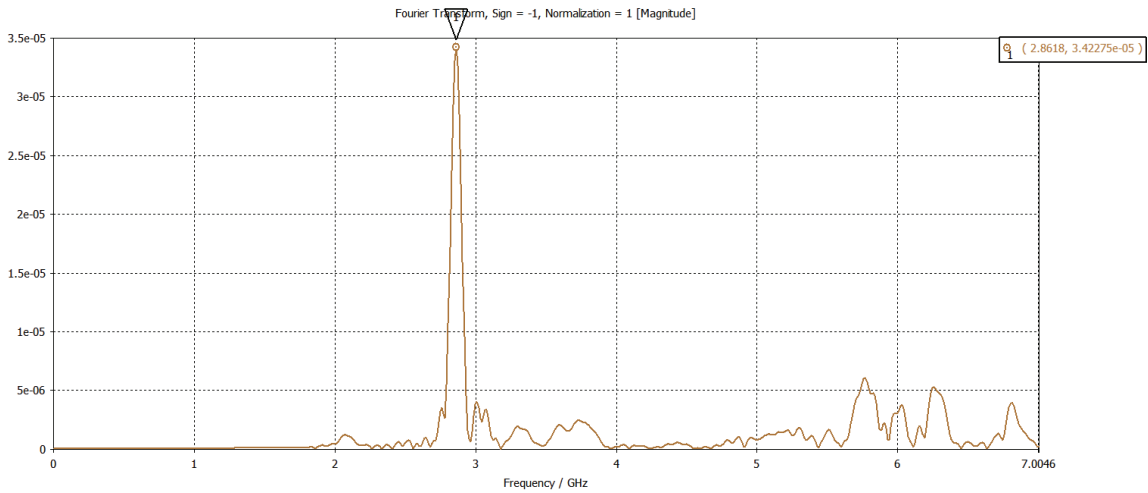


Figure 4.29 FFT of output electric field.

The electric field distribution inside of the CSSR has some high intensity regions. The risk of high intensity electric fields in hot tests is electrical breakdown. The specific unit cell geometric arrangement and polarization angle create a mixture between modes 2 and 3. A temporal analysis computes the electrical field distribution for 2-unit cells below in

Figure 4.29.

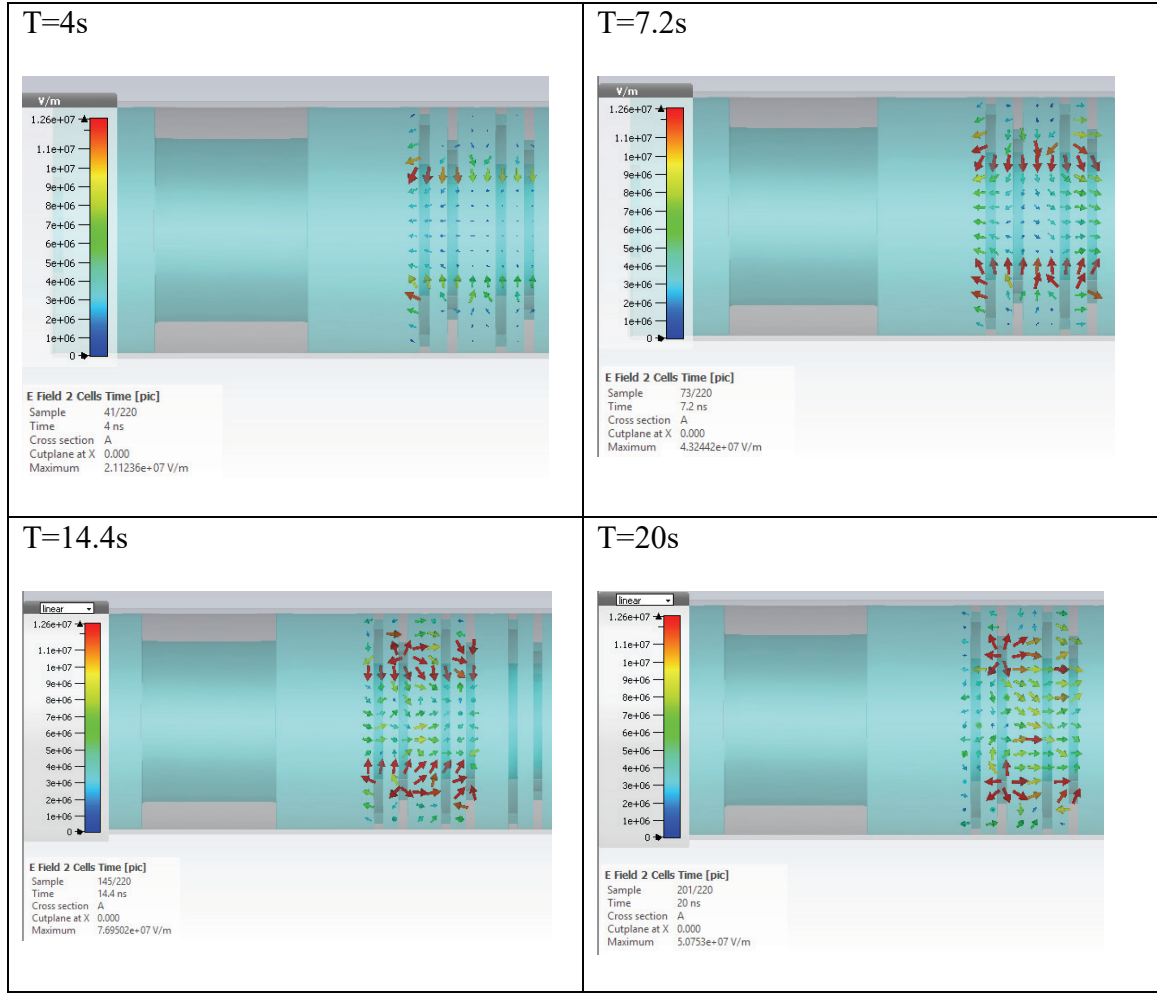


Figure 4.30 E-field distribution for 490 kV at different times.

Since the geometry of this SWS is unique, there is a lack of description in literature. At the same time, it is a great opportunity to consider the space harmonic structure (SHS). The electric field distribution suggests π -mode-like operation. When the fields in adjacent cavities are in phase the net current in the slots is zero and the frequency is equal to the resonant frequency for an isolated unit cell. When the fields are antiphase the net current in the slots is nonzero. In this case the frequency is below the resonant frequency of the slots and they have an inductive reactance to current flow and, as a result, decrease the frequency of the mode.

A full perspective of the electric field along the SHS is illustrated in Figure 4.30. Due to constraints of operation and assembling in the SINUS-6, the number of pairs of CSRRs was reduced from 16 to 11. This might be responsible for the loss of four wave degeneracy in the DBEO.

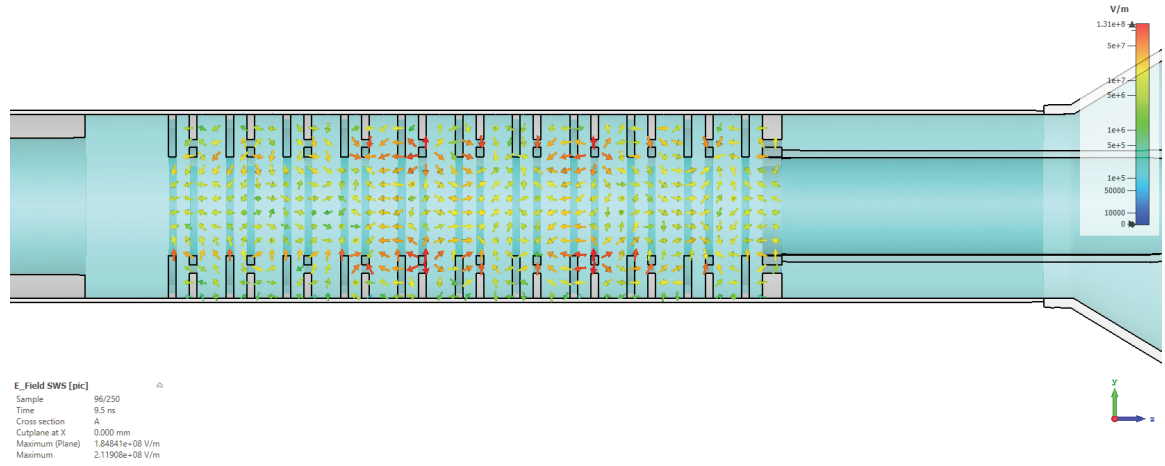


Figure 4.31 Electric field distribution along the 11-period MTMSWS.

The beam created by EEE interacts with the rings and slots. Initially the first ring and slot slightly affect the electron beam as shown in Figure 4.31.

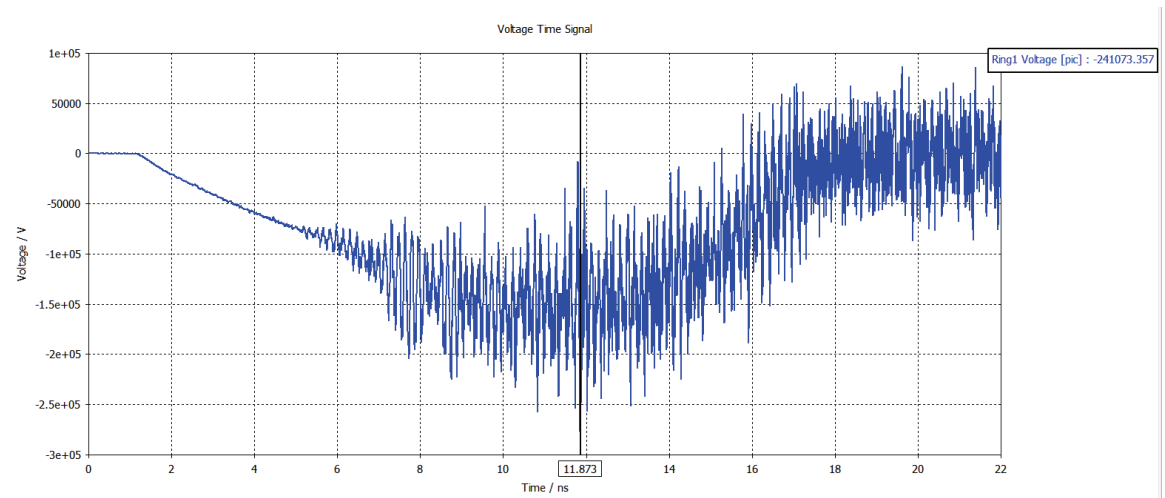


Figure 4.32 Voltage in the first ring (straight).

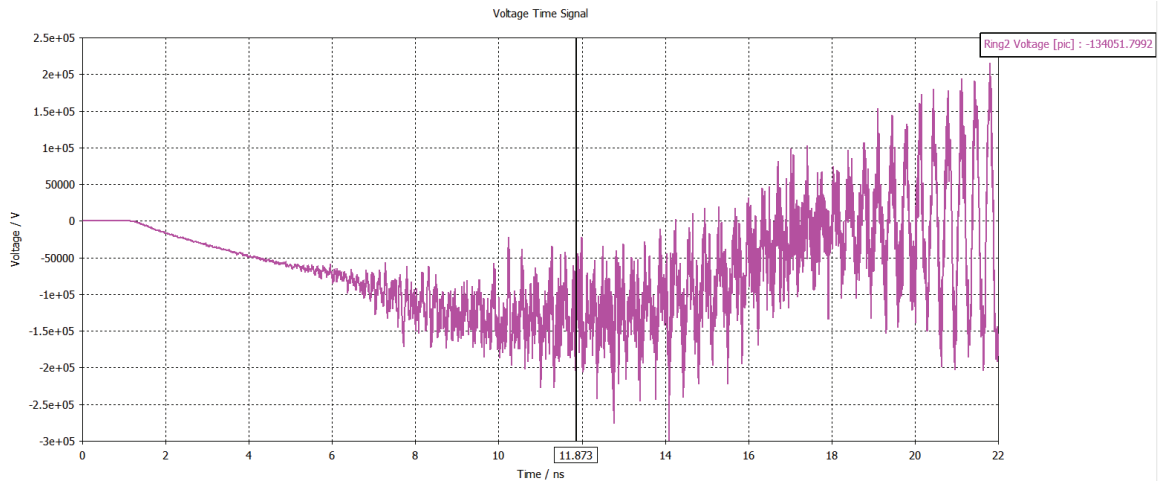


Figure 4.33 Voltage in the second ring (angle).

The amplitude ratio between the disks in Figures 4.31-4.32 is 0.55, and in Figure 4.33 it is possible to note that the perturbation in the beam is getting larger.

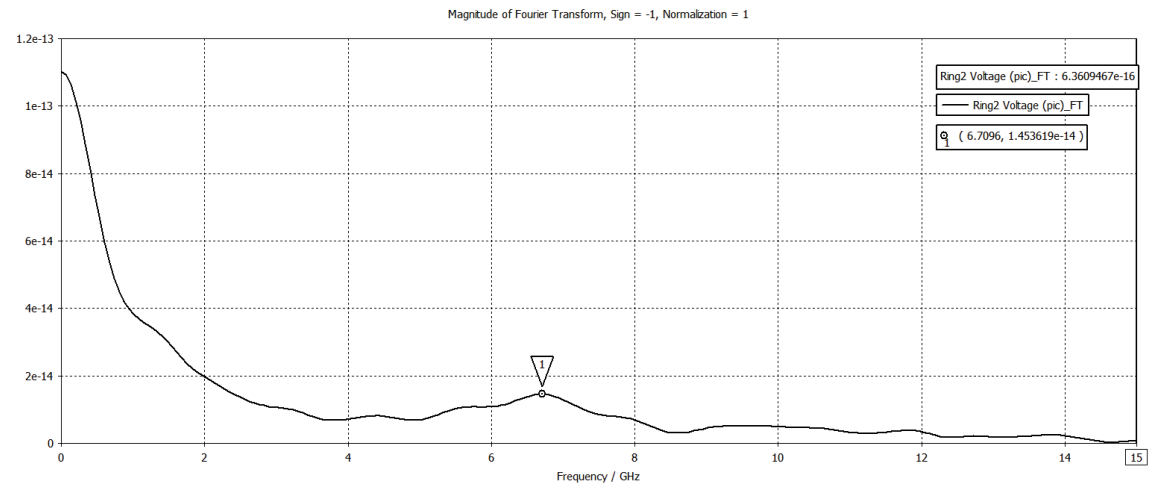


Figure 4.34 FFT of the signal from ring 2.

Applying an FFT to the signal from ring 2, it is observed that a large DC component is present and the frequency of oscillation is near 6.7 GHz. At the same time the interaction of the beam induces a voltage in the slots as illustrated in Figure 4.34.

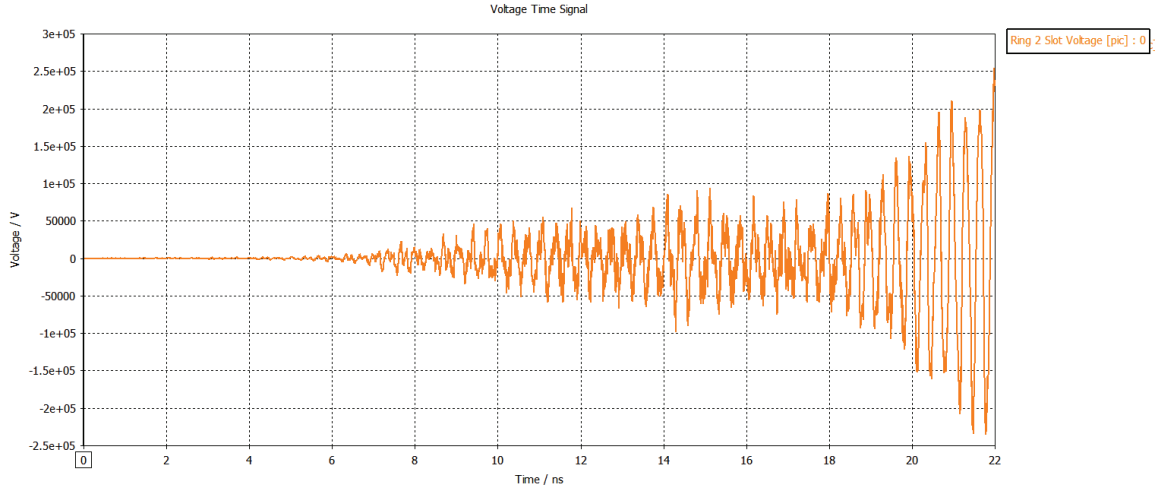


Figure 4.35 Voltage in the slot of ring 2.

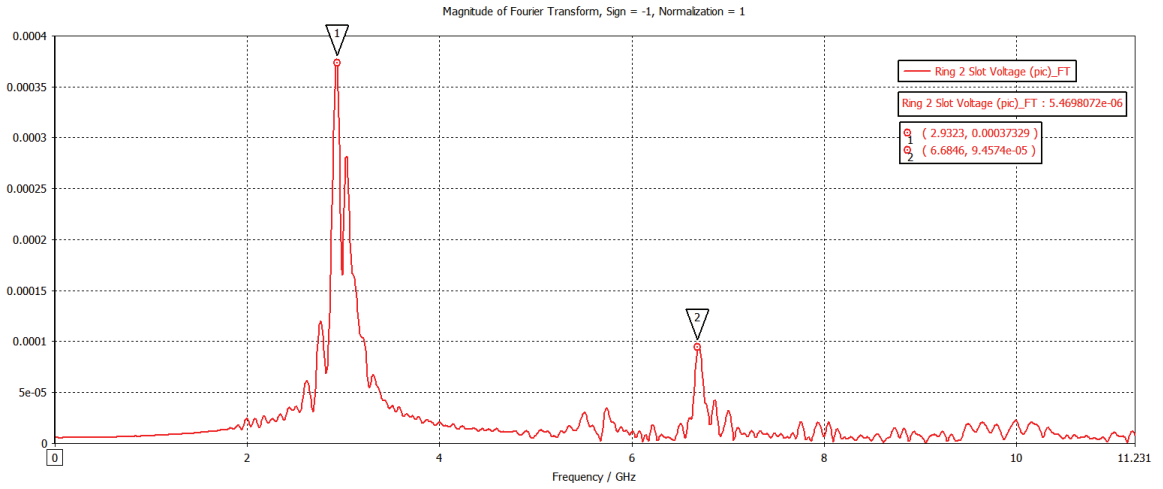


Figure 4.36 FFT of ring 2 slot voltage.

It is interesting to note that the frequency of oscillation in the ring 2 slot is offset by 2.4% from the PIC code results. This is practically the frequency of operation for the VED.

For the second unit cell the amplitude ratio for rings 3 and 4 is 56.4% bigger and the resonant frequency in Figure 4.37 is almost the same as in Figure 4.35 the offset is less by about 1.74% from the PIC code result. Nevertheless, this proximity in frequency also states that the cavity is operating in a π mode-like manner.

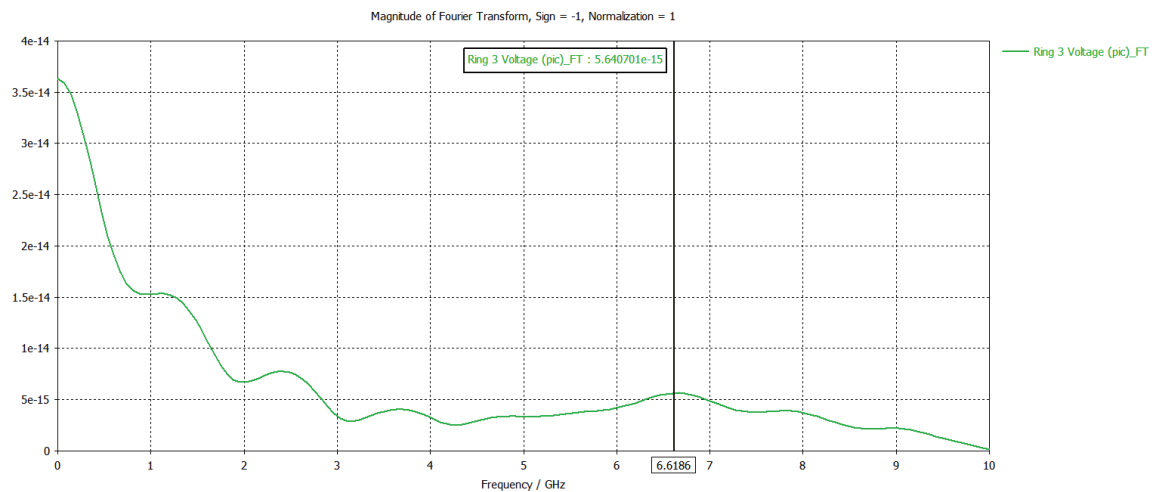


Figure 4.37 Voltage in ring 3 (straight).

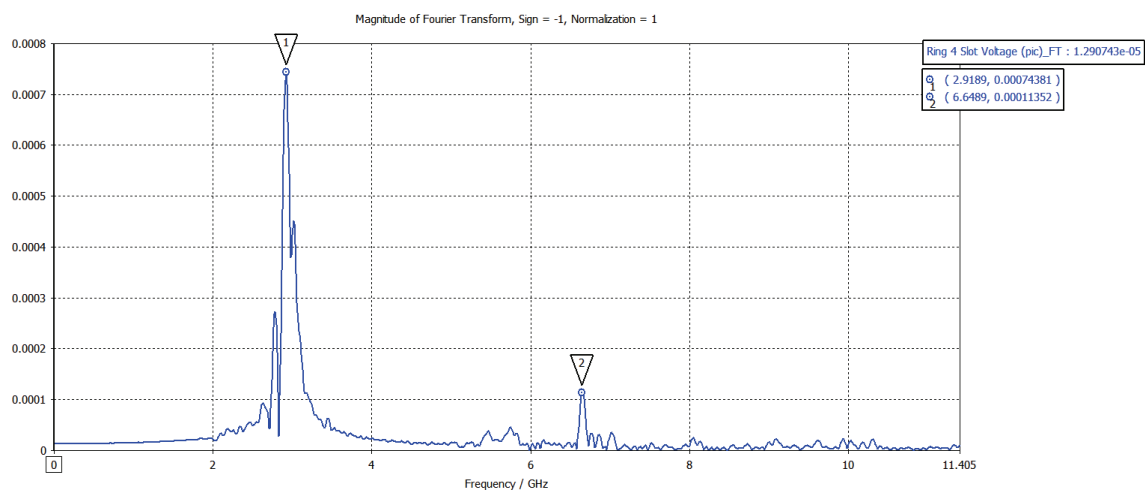


Figure 4.38 FFT of ring 4 slot voltage (angle).

The transverse magnetic mode for the SHS is TM_{01} as illustrated in Figure 4.33. This is expected due to the strong electric field along the z direction. This result matches the simulations from the eigensolver and frequency domain.

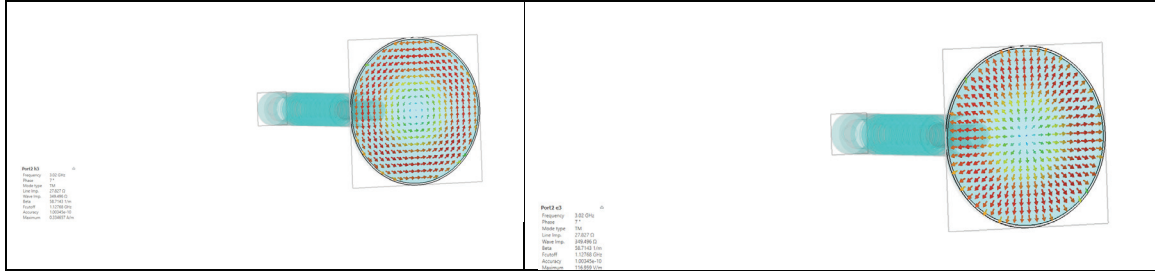


Figure 4.39 Transverse magnetic mode.

4.5.3 PIC Simulation with SINUS Voltage Waveform Input File

An input file with the voltage waveform from SINUS with amplitude 490 kV was used in CST as an excitation source. The purpose is to add to the PIC model the characteristics of the pulse only present in the experiment. The main parameters observed were voltage, cathode current, output RF power, and frequency from Figures 4.39-4.42.

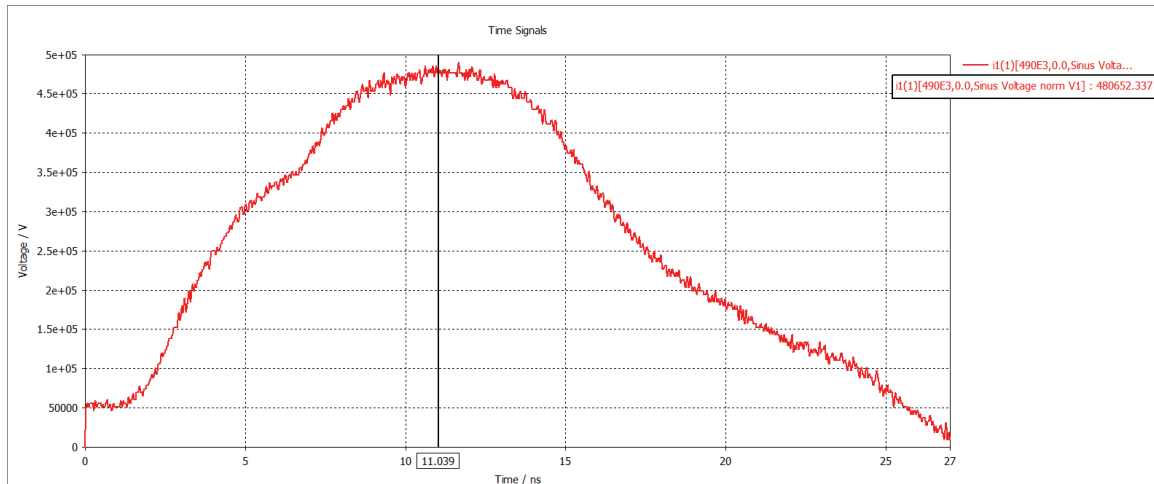


Figure 4.40 SINUS voltage waveform in experiment.

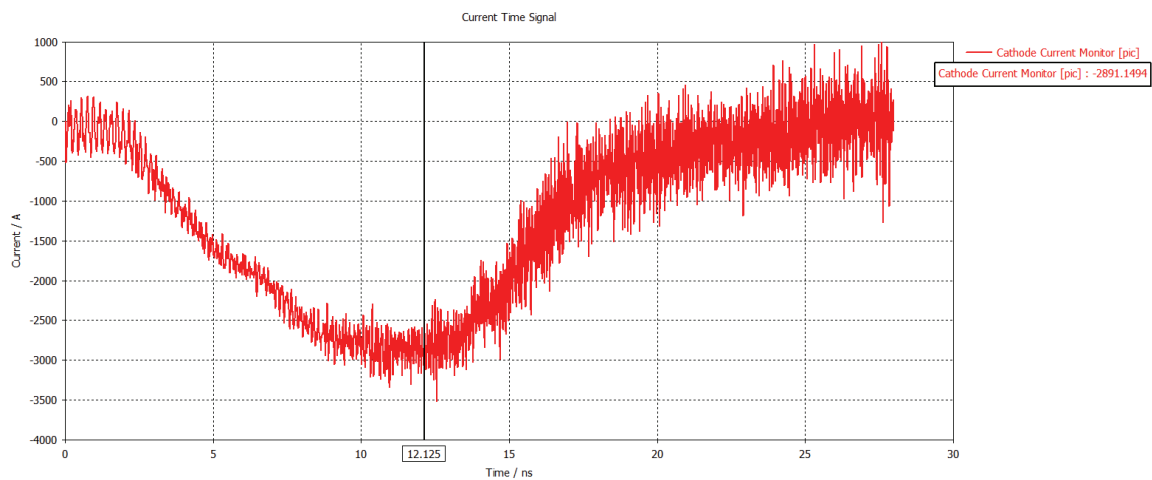


Figure 4.41 Cathode current in experiment.

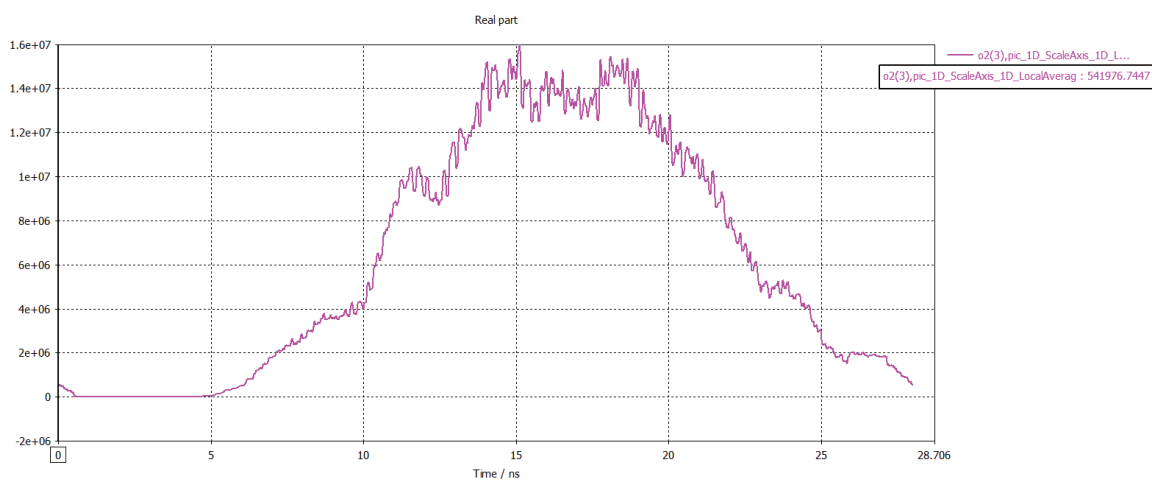


Figure 4.42 Output RF power in experiment.

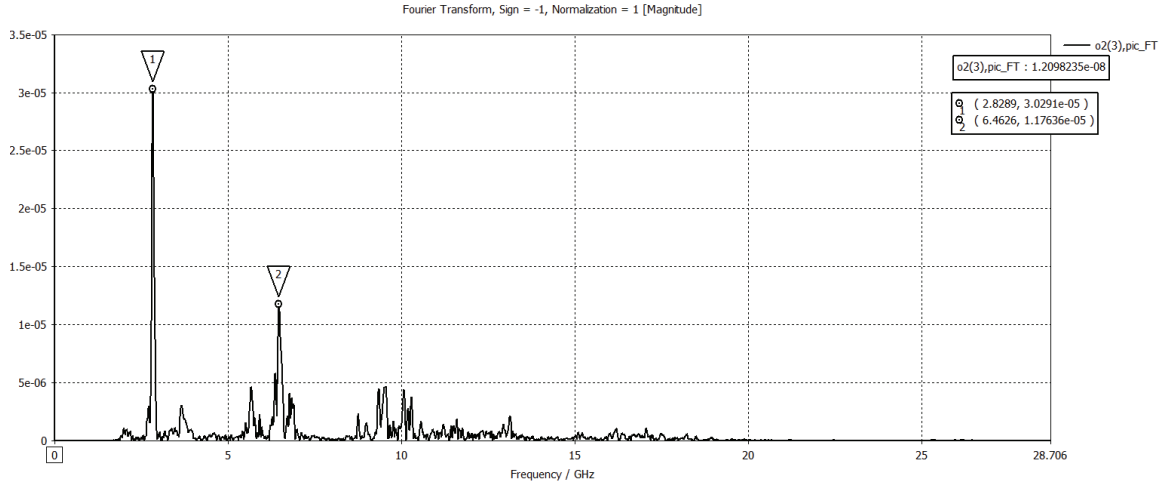


Figure 4.43 FFT of the output RF electric field in experiment.

The fluctuations in output power might be a result of the second harmonic which is stronger for the CST-SINUS 6 profile. It is important to note that it might be possible to generate more than one frequency in the source, although this will degrade the output RF power. Nevertheless, the possibility to excite two tones might offer an opportunity for frequency agility of the MTMSWS source.

The ring slot voltage profile signal is similar to the ideal pulse but second harmonic generation in Figures 4.43-46 is more apparent.

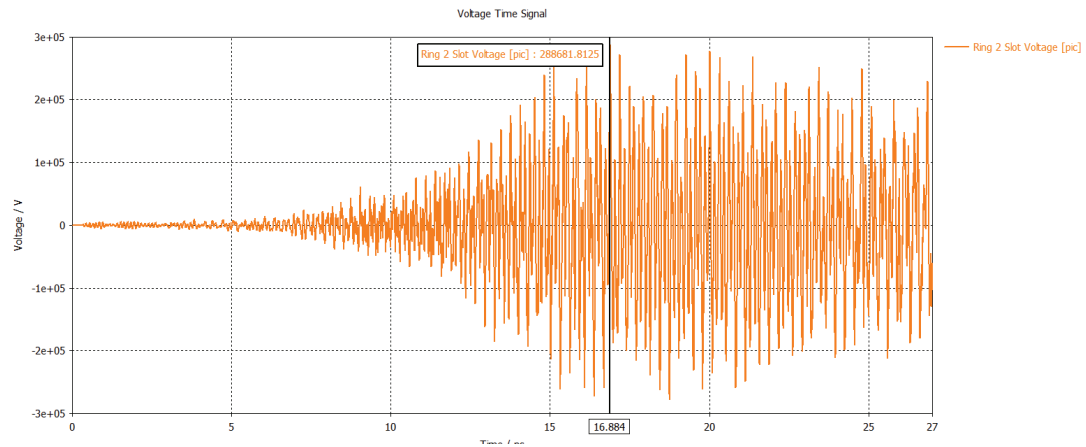


Figure 4.44 Voltage in the slot of ring 2.

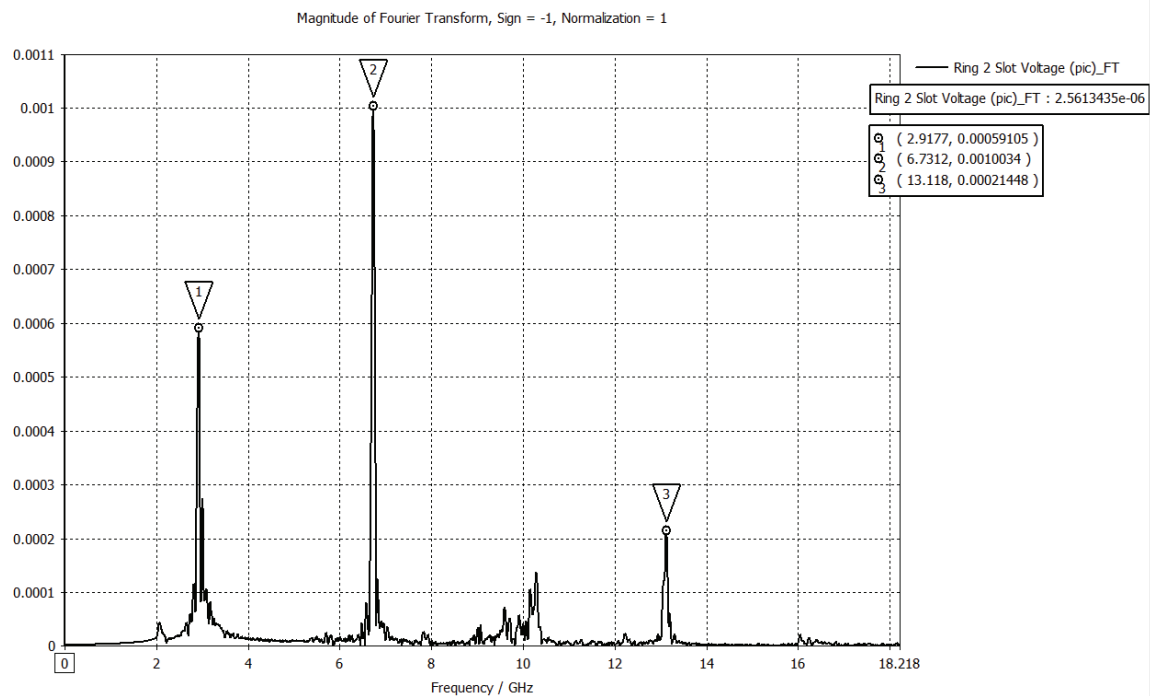


Figure 4.45 FFT of the ring 2 slot voltage (angle).

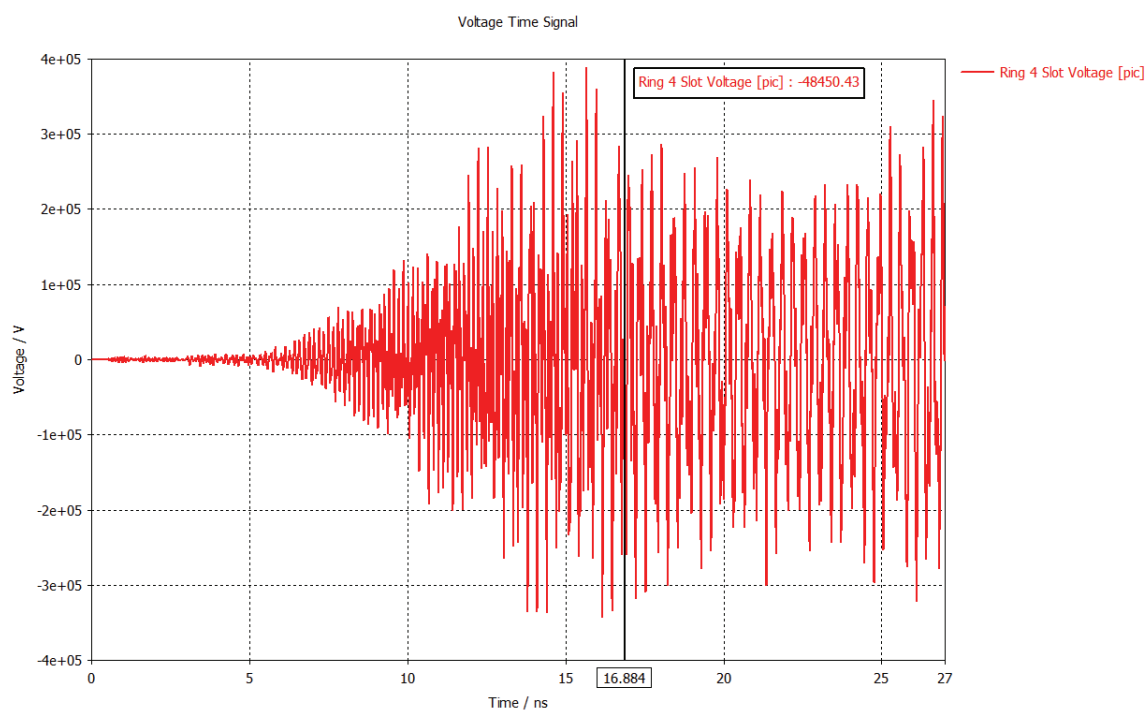


Figure 4.46 Voltage in the slot of ring 4 (angle).

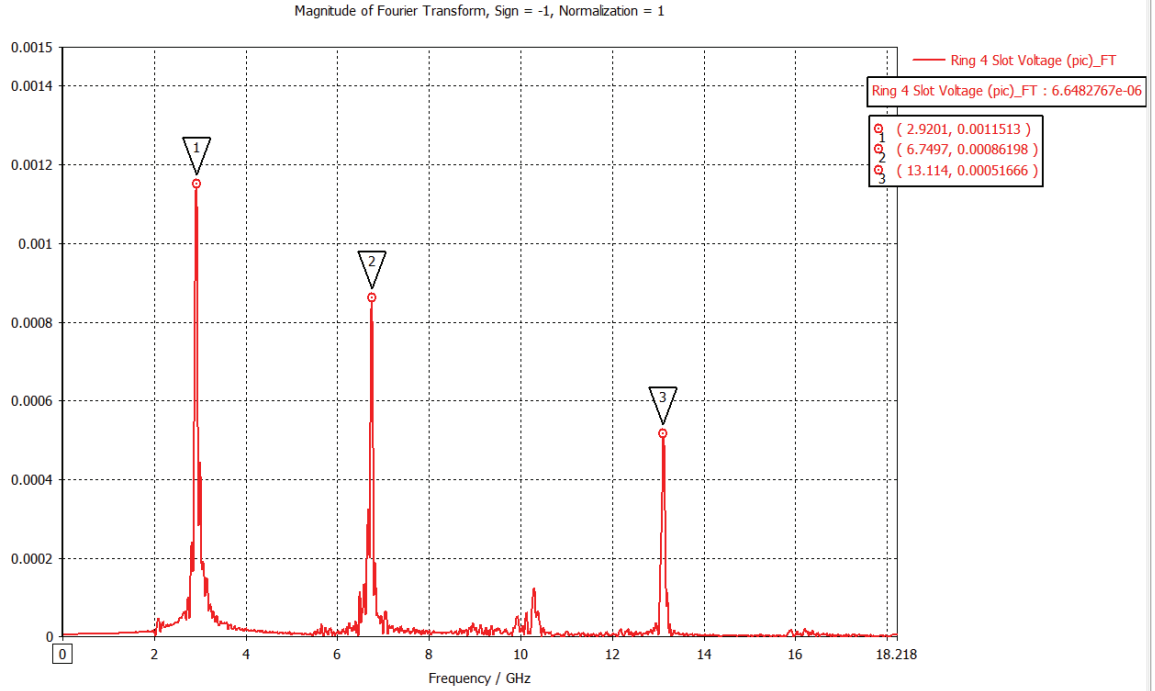


Figure 4.47 FFT of the ring 2 slot voltage (angle).

The simulation results from Figures 4.43-4.46 are in good agreement with the benchmark in Table 4.2. Another interesting result is the frequency of oscillation for the slots are close to frequency of oscillation between the gaps as shown in Figure 4.47. This might be the case when the beam travels through the gap and “lights up” the cavity. Thus, the charged particles generate an electric field which induces the magnetic field that in turn creates the coupling between rings along the structure. The second harmonic present in the FFT of Figure 4.46 might indicate slight mode competition.

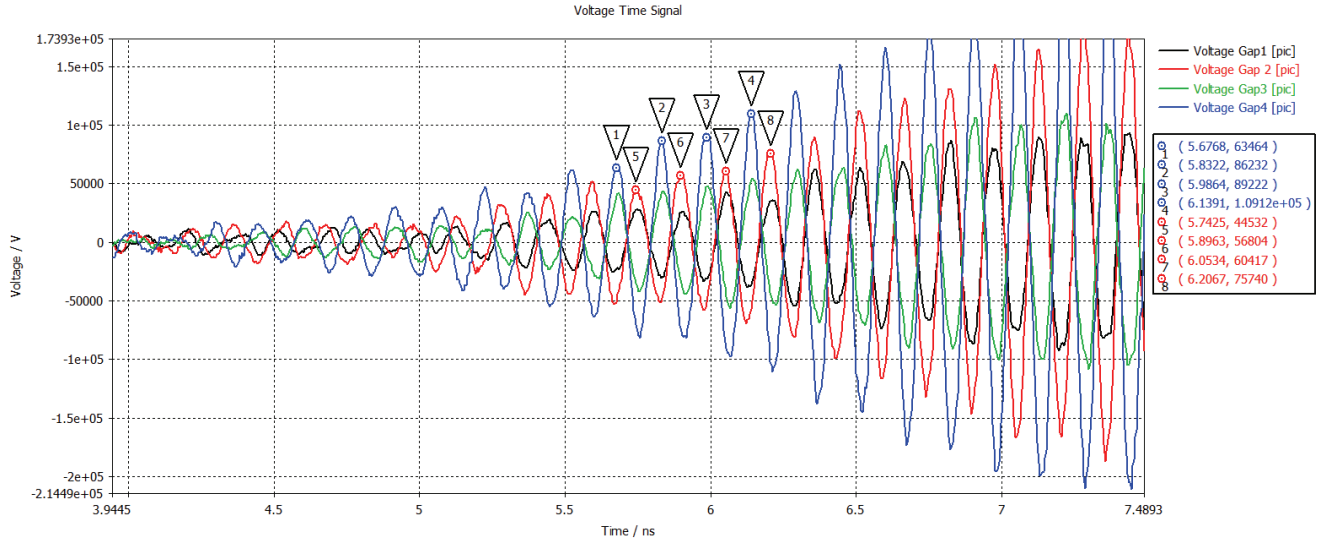


Figure 4.48 Voltage between gaps 1-4

It is possible to notice three distinct characteristics from Figure 4.43-4.47: an increase in voltage, “a match in phase,” and the frequency of oscillation. First, the voltage gradually increases as a result of electrons’ acceleration, followed by a match of oscillation starting point, and finally the frequency generation. According to points 1 to 8 in Figure 4.47 the frequency is about 6.52 GHz and this is twice the oscillation frequency from the slots. This coupled cavity configuration is split basically into two functions. One ring with the outer slot is responsible for polarization shift, the second ring with the slot close to the beam is capable of couple and harvesting energy from the beam. Such a distinct behavior can produce a mixing of modes and improves the degeneracy since this unit cell has three degrees of freedom.

A second crosscheck and optimization of the model for PIC code was done changing the excitation source from ideal to real Sinus-6 voltage waveform. The results from this update are summarized in Table 4.3.

Table 4-3 Optimized PIC and benchmark parameters.

Profile	Voltage (kV)	Current (kA)	Frequency (GHz)	Power (MW)
CST-SINUS 6	489.90	2.89	2.82	15.97
CST-Ideal Pulse	490.00	2.91	2.86	33.28

The results for the optimized PIC code strongly agreed with the ideal pulse except for the power output. Although the power measurement in CST has always been a matter of discussion. Nevertheless, the addition of the new excitation source included nonlinear behavior in pulse profile.

The four-wave mix degeneracy in the original UCI design was lost when the structure was redesigned to fit within the constraints of the UNM set-up. At the same time, it affected the bunching. Another side effect is reducing the overall performance (RF output power) because the last ring from the MTMSWS is thicker than originally designed in order to support the beam collector.

The bunching phenomena along the SWS shows two interesting characteristics in Figures 4.49-4.50. First, due to the reduction in size and number of unit cells with a thicker last ring there is a bunch collapse after 220 mm. The bunching ends in the region of the beam collector and the mode of operation of the cavity suggests an even number of unit cells.

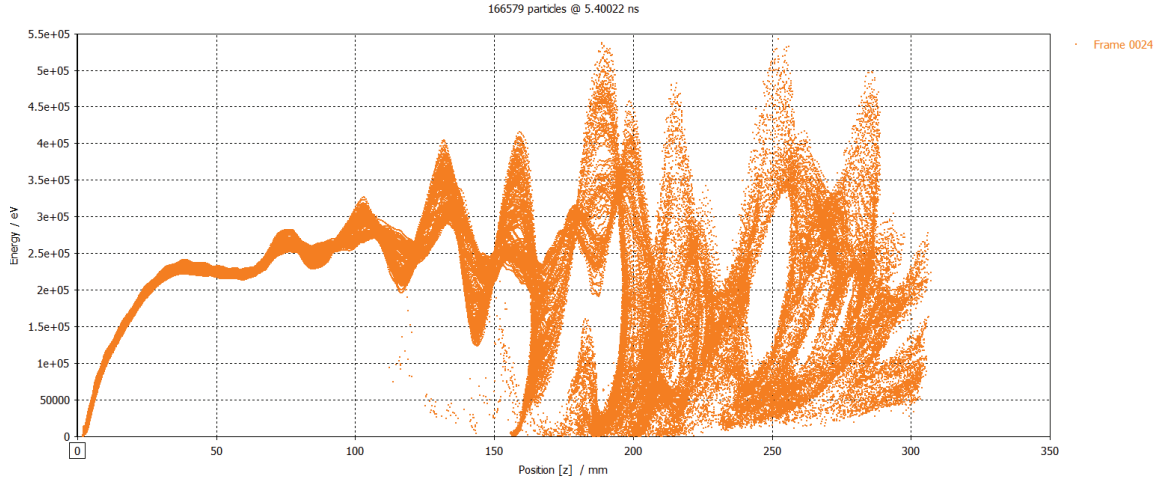


Figure 4.49 Electron bunching inside the SWS at 5.4 ns.

Second is the fact that there are particles traveling back to the cathode with high energy as show in Figure 4.49. This phenomenon might be a result of space charge and dimensions of the beam collector that favor the possible formation of a virtual cathode.

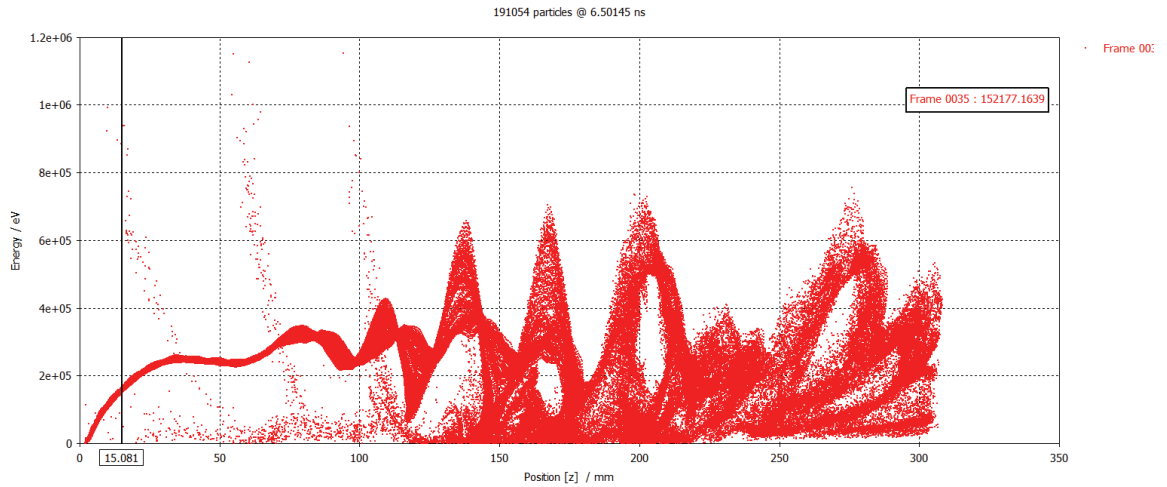


Figure 4.50 Electron bunching inside SWS at 6.5 ns.

4.6 Hot Test Experiments: Horizontal Power Scan

A hot test is the actual experiment where the SWS is attached to the accelerator and has the electron beam traveling through it guided by a strong magnetic field. The purpose of the hot test experiment is to validate the computational PIC results. Figure 4.51 is a summary of the experimental campaign with 40 shots.

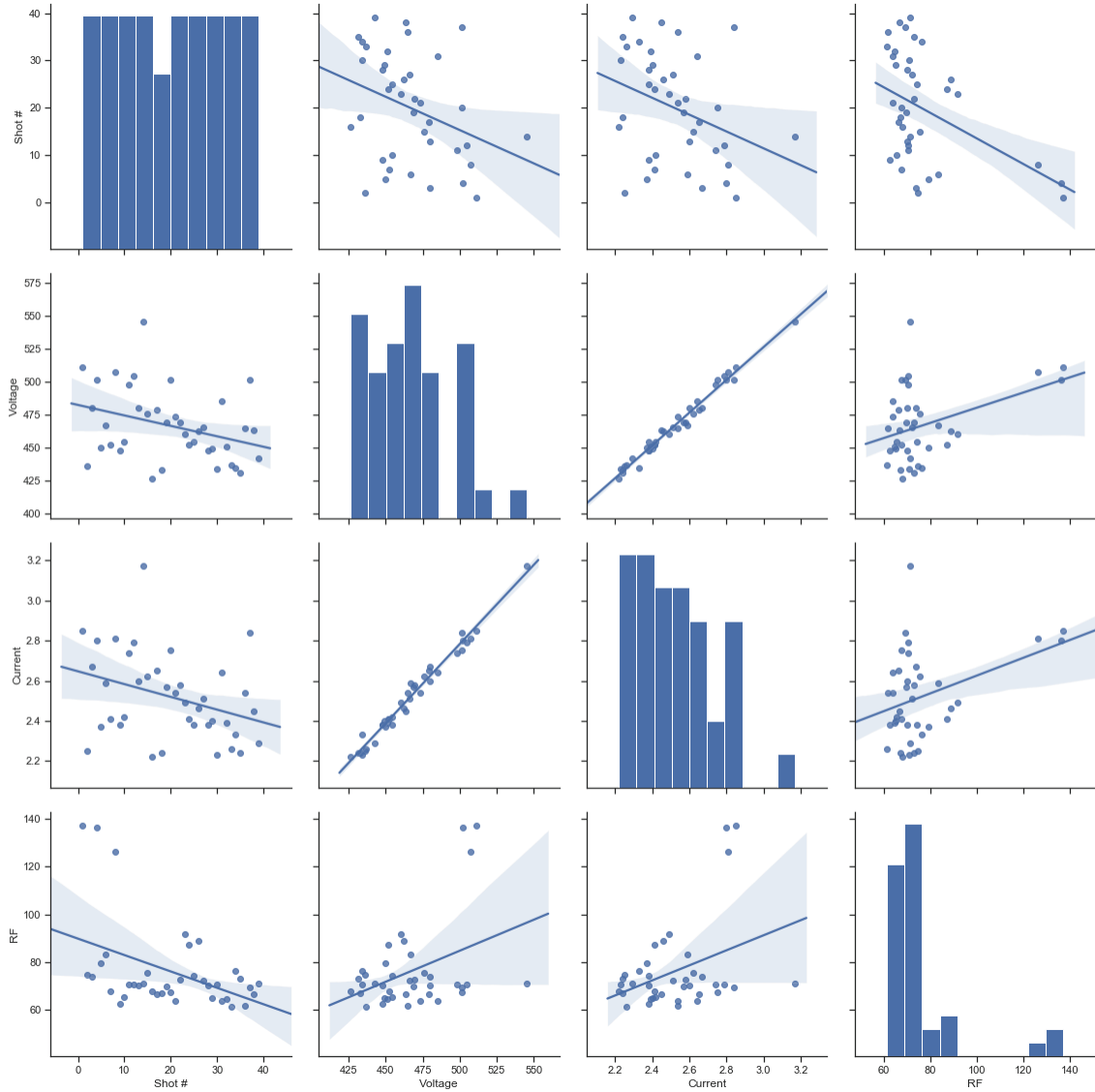


Figure 4.51 Experimental hot test results [22].

Data analysis for the pulsed power driver illustrated a constant load impedance. The electron beam accelerator is a current source driven by voltage. Thus, great fluctuations in the impedance affects SINUS performance.

A fast oscilloscope measured the signal waveforms for voltage, current frequency, and RF power for the MTMSWS as shown in Figure 4.52.

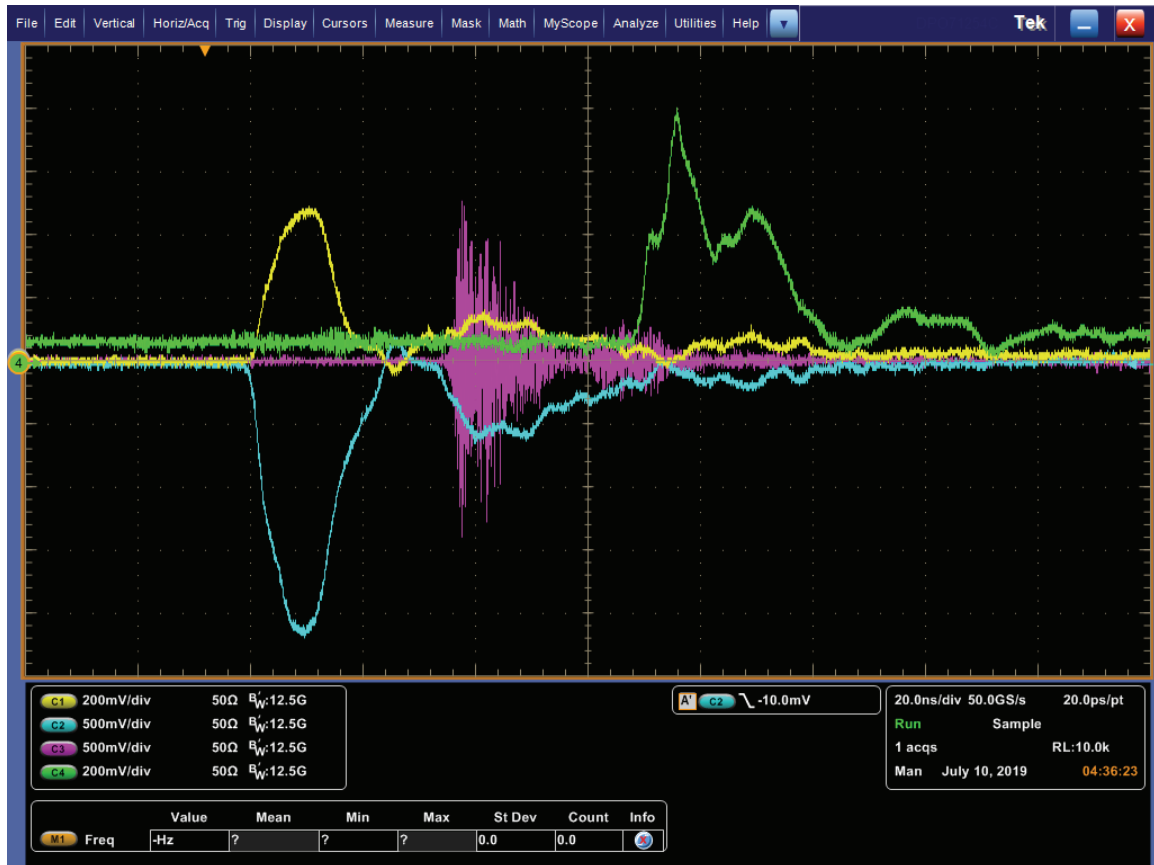


Figure 4.52 Fast signal measurements: CH1-current, CH2-voltage, CH3-RF power, and CH4-frequency.

This is the first time that a fully 3D printed MTM source for HPM generation [30] was evaluated in the nanosecond range. The PIC simulation results agreed with hot test experiments. The time frequency analysis from Figure 4.53 shows a broad-spectrum component. These harmonics degrade the RF power output and widen the pulse duration.

Shot 1

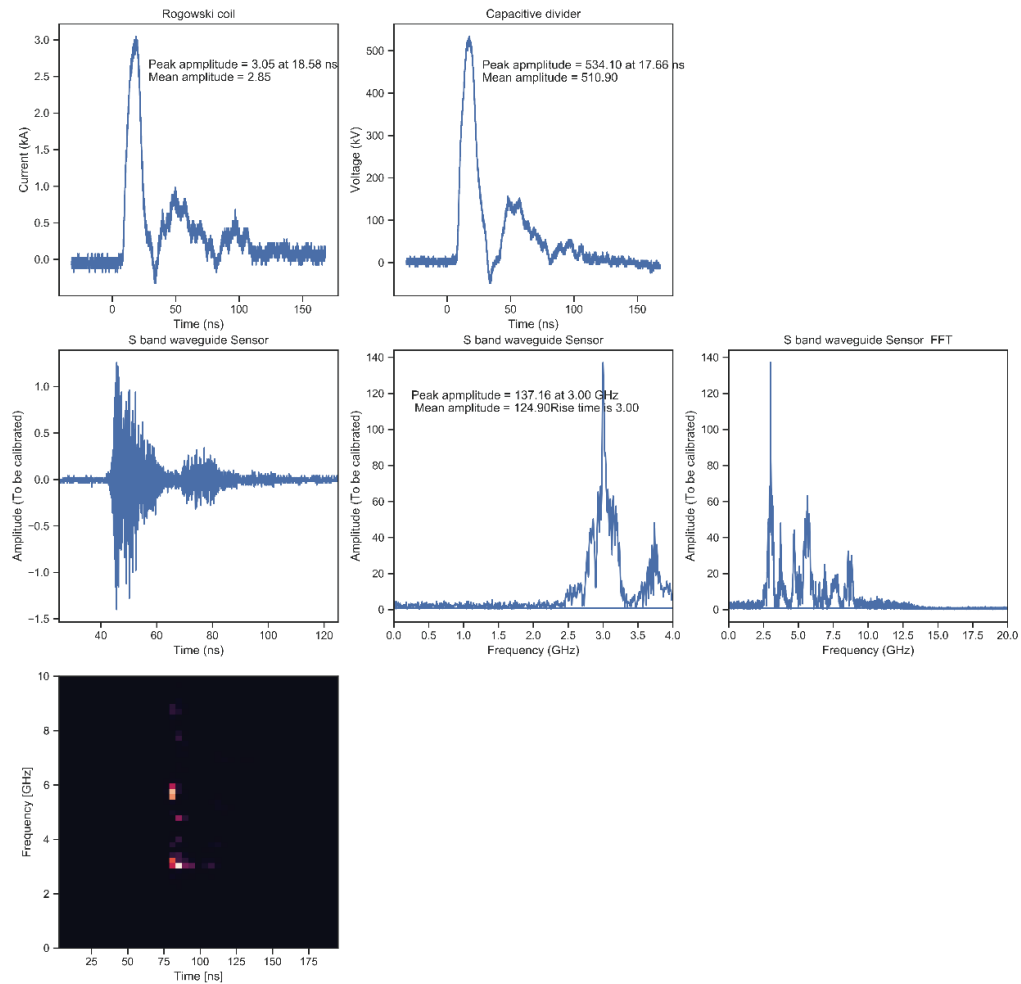


Figure 4.53 Hot test results for the 3D printed MTMSWS.

After running the optimized PIC code simulations using CST the efficiency was 6.04% as shown in Table 4.4. The operation of the MTMSWS can be evaluated using two different metrics, one regarding the efficiency and second the peak RF power [31]. For SINUS-6 the operation considered is highest power.

Table 4-4 Output RF power signal from CST using the SINUS voltage waveform.

V_{applied} (kV)	I_{cathode} (kA)	Peak Power (MW)	Efficiency (%)
510.9	2.85	88.06	6.04

The Poynting vector in the far-field scattering is independent of polarization. This power density shown in Figure 4.54 is measured over an arc, as shown in Figure 3.11 in the far-field zone and is described by the equation

$$P(x) = 7544.22 + \left(\frac{790696.04}{\sqrt{\frac{\pi}{2}}} e^{\left(\frac{x-85.14}{23.84}\right)^2} \right) (1.3^2 \sin(x)) \quad 4-1$$

Equation 4.1 is a Gaussian approximation for the Poynting vector distribution. According to this field scattering it is possible to notice a symmetric distribution. As a result, the horizontal and vertical power density scans have the same distribution. The total power irradiated measured is 22.06 MW. The Gaussian distribution in the far field is shown in the Figure 4.56. The Poynting vector from the antenna has a half power beam width of approximately 35°.

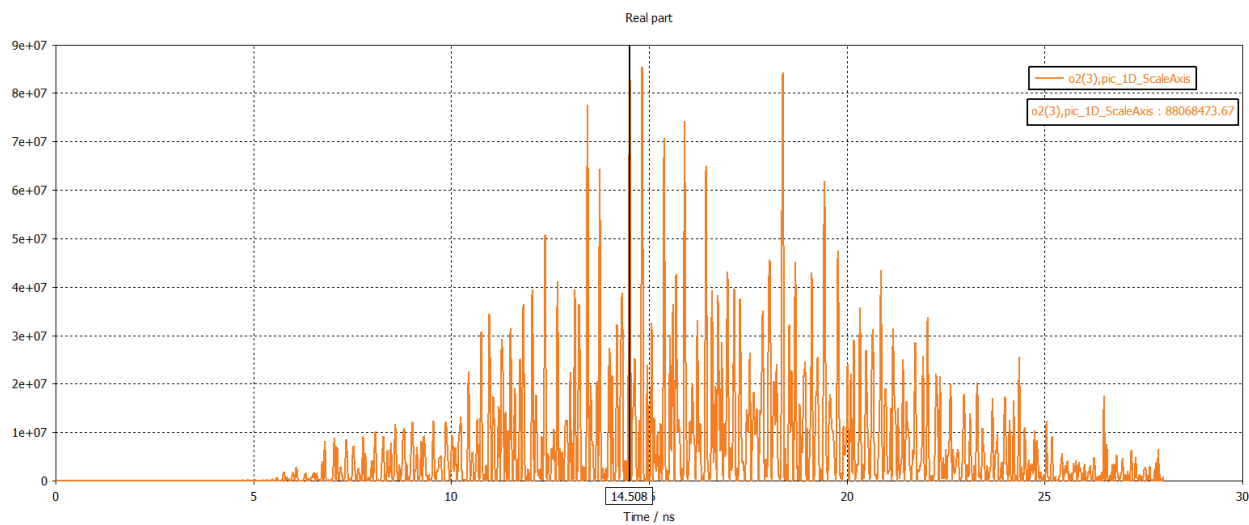


Figure 4.54 Output RF power signal from CST-SINUS-6 driver.

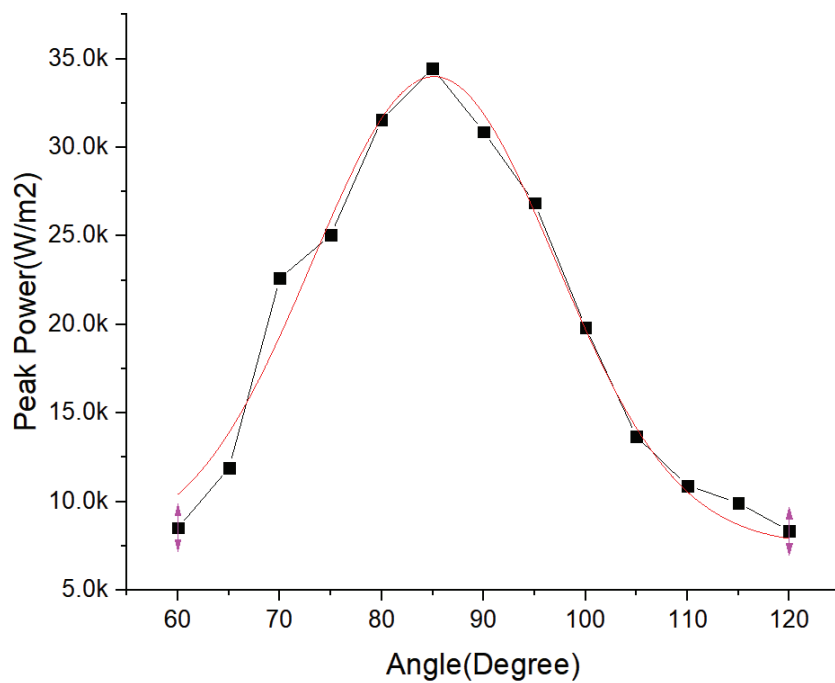


Figure 4.55 Poynting vector distribution.

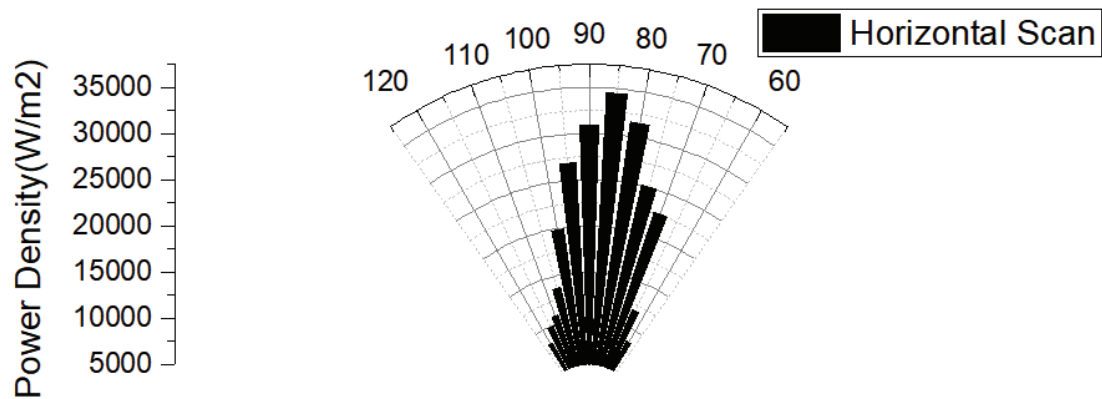


Figure 4.56 Horizontal power distribution.

Comparing the CST-SINUS and experimental hot test results the overall agreement is 88%, as shown in Figure 4.57.

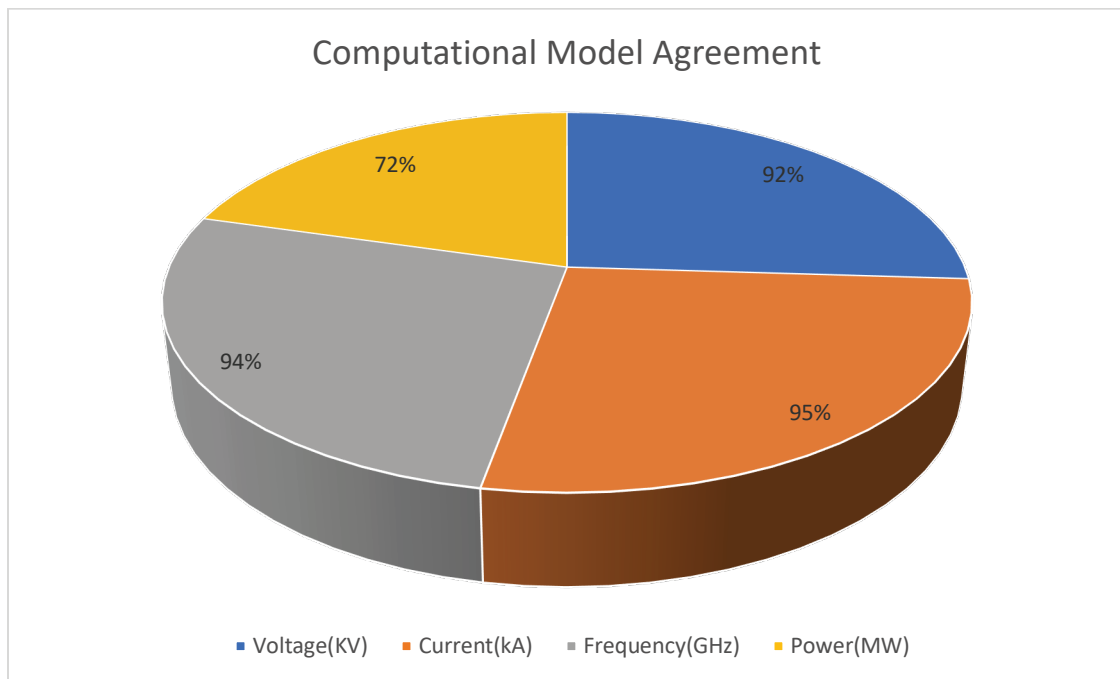


Figure 4.57 Computational versus experimental hot test results.

It is interesting to point out that the experimental value for output RF power is now a world record for a 3D printed S-band O-type MTM device since this value is almost 7 times greater than a similar structure geometry [32].

4.7 Visible Radiation Pattern Detection

Basically, two measurements were made, radiation pattern and time-integrated light coming out the source were detected using the same diagnostic. The radiation pattern is not TM_{01} as expected from PIC code simulations. As shown in Figure 3.15, part of the beam collector is inside of the antenna and this changes the electric field as was also noticed for another MTMSWS [33]. As a result, there is mode conversion from TM_{01} to a “ TE_{12} -like” mode due to the coaxial feed.

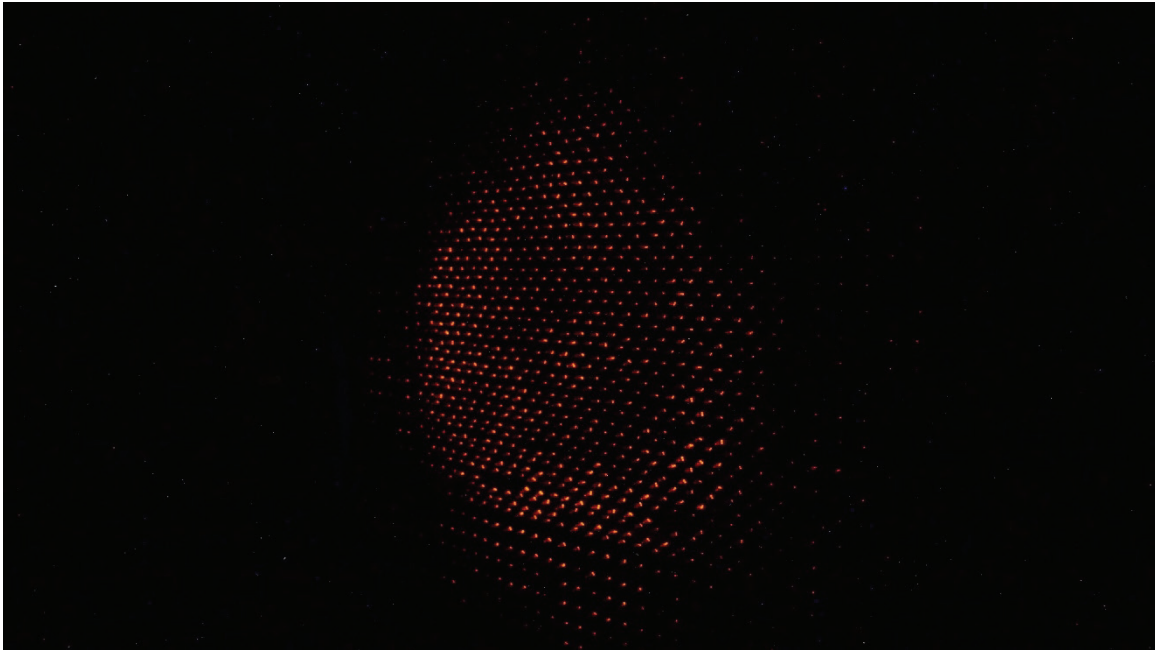


Figure 4.58 Radiation pattern from the neon bulb array.

The idea to capture the emission of light from the source is to evaluate through plasma diagnostic aspects of charge particle beam and SWS interaction. Unfortunately, the only diagnostic available was an SLR camera. Figure 3.14 describes the layout for the experiment. An unexpected result is shown in Figure 4.58 - blue light coming out from the HPM source during the experiment when the highest voltage measured was about 563 kV and no breakdown was noticed inside the MTMSWS. Cherenkov radiation [34] in nuclear reactors is blue light attributed to charged particles (electrons) traveling faster than the characteristic speed in the medium (water). However, the light observed here is probably a glow following diode impedance collapse at the end of the voltage pulse.

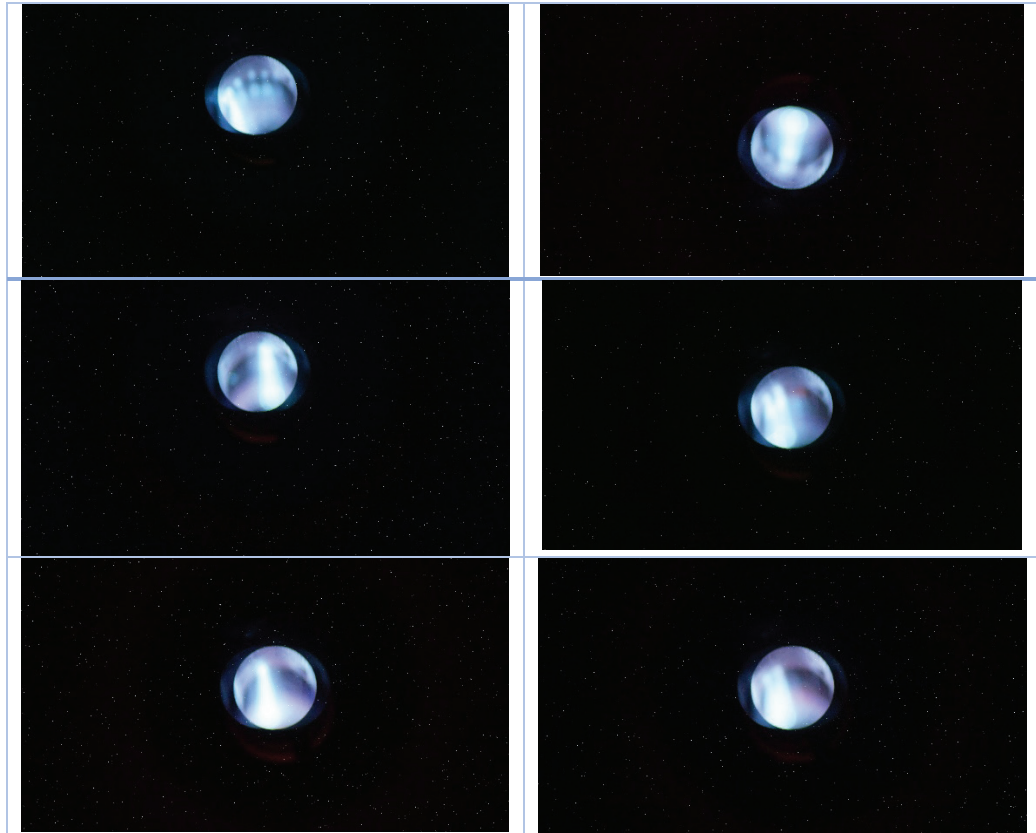


Figure 4.59 Visible light detection from the MTMSWS source.

5 CHAPTER 5: CONCLUSION AND FUTURE WORK

Initially the purpose of this thesis was to experimentally verify PIC simulations of the DBEO oscillator designed by UCI. However, due to the constraints of the SINUS-6 electron accelerator a series of optimizations performed by UNM led to a MTMSWS capable of fitting inside the accelerator. The new model was extensively tested experimentally with more than 100 shots for a vacuum between $7.6\text{E-}6$ to $1.3\text{ E-}5$ Torr. Figure 5.1 indicates a very little bump, which might be the result of part of the annular electron beam emitted from cathode hitting the first ring of the SWS.



Figure 5.1 3D printed MTMSWS after more than 100 shots.

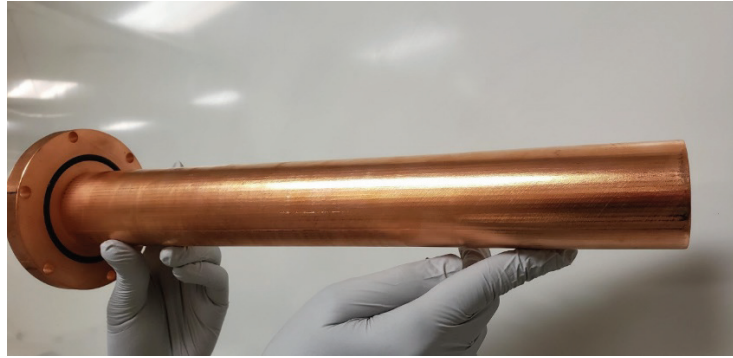


Figure 5.2 3D printed MTMSWS in its waveguide.

The simulation results from the eigenmode solver showed that mode 3 with a cutoff frequency of 2.88 GHz and in the TM_{01} mode were shown. In addition, the coupling impedance indicated how well the MTMSWS harvested the energy from the beam with value about $134.48 \, \Omega$ as reported in previous UCI reports. Also, this value was later validated in cold tests using the VNA.

According to frequency domain simulation results, a negative permittivity and permeability in the passband were computed. This is strong evidence of DNG behavior and also permitted operation below the cutoff frequency of the waveguide.

Simulations using PIC codes agreed regarding the basic parameters to evaluate the source. At the same time each code validated the other disregarding their premises in modelling the VED. A very good charged particle model requires high computational resources and longtime exposure to an experiment to update the parameters and optimize the code. As a result, the experimentalist became an essential asset capable to interact with computer code and experiment itself. The plot from Figure 4.56 described such interaction and overall the agreement is 88% demonstrating that the optimized PIC code model is reliable.

The neon bulb array showed a different radiation pattern from the simulations in which a null was presented in the middle resembling a TM_{01} mode. Possible mode conversion occurred inside of the horn antenna due to the presence of a coaxial feed (beam collector) from the MTMSWS to the output horn antenna.

Following the PIC simulations experimental hot test were performed and synthesized the expectations of how the real prototype would work. In a practical sense small steps between mechanical alignment, vacuum, and condition of the pulsed power driver allowed the source to work properly. After more than one hundred shots there was no evidence that mechanical properties and electromagnetic characteristics were affected. The average parameters for the 3D printed MTM are summarized in Table 5.1.

Table 5-1 Average parameters.

V_{applied} (kV)	Current (kA)	Frequency (GHz)	Power (MW)
490	2.71	2.98	22.06

The impedance mismatch for SINUS is nearly 26.4%. However, the design of the MTMSWS made its operation resilient to voltage fluctuations. Nevertheless, a very good alignment of 91% guaranteed the safe operation of the 3D printed MTMSWS.

Future work will include measuring the light emission from breakdown, and a voltage and magnetic field scan to identify other possible points of operation as cold test initially predicted. Furthermore, a deep investigation into the radiation pattern is important to validate the performance of the antenna. There is the possibility that the mode conversion due to the coaxial feed reduces the quality factor of the oscillator.

Nevertheless, an outstanding result was achieved, a 3D printed MTM S band was capable to generate an average power of 22.06 MW. This achievement brought UNM to the top of HPM generation from a 3D printed MTMSWS. Because of this, new sources can be developed using the additive manufacturing process leading research to a point where its limits are the creativity of the scientist.

REFERENCES

- [1] J. Benford, J.A. Swegle, and E. Schamiloglu, *High Power Microwaves*, Boca Raton, FL, CRC Press, 2016, p. 11.
- [2] S. D. Davis, "Controlled Warfare: How Directed Energy Weapons will Enable the US Military to Fight Effectively in an Urban Environment while Minimizing Collateral Damage," *Small Wars & Insurgencies*, pp. 49-71, 24 December 2014.
- [3] R.J. Barker and E. Schamiloglu, Eds., *High Power Microwave Source and Technologies*, New York, NY, IEEE Press, 2001, pp. 3-4.
- [4] Z. Duan, X. Tang, Z. Wang, Y. Zhang, X. Chen, M. Chen, and Y. Gong, "Observation of the Reversed Cherenkov Radiation," *Nat. Commun.*, pp. 1-7, 23 March 2017.
- [5] D. Andreev, A. Kuskov, and E. Schamiloglu, "Review of the Relativistic Magnetron," *Matter and Radiatio Extremes*, vol. 4, no. 6, pp. 1-19, 2019.
- [6] G.J. Pollock and K.I. Ashwin, "Below-Cutoff Propagation in Metamaterial Lined Circular Waveguides," *IEEE Trans. Microw. Theory Techn.*, vol. 61, no. 9, pp. 3169-3178, 2013.
- [7] V.G. Veselago, "The Electrodynamics of Substances with Simultaneously Negative Values of ϵ and μ ," *Sov. Phys. Usp.*, vol. 10, no. 4, pp. 509-514, 1968.
- [8] R. Marques, J. Martel, and F. Medina, "Left Hand Media Simulation and Transmission of EM Waves in Sub-Wavelength Split-Ring Resonator Loaded Metallic Waveguides," *Phys. Rev. Lett.*, vol. 89, no. 18, pp. 1-4, 2002.
- [9] D.R. Smith, W.J. Padilla, D.C. Vier, S.C. Nemat-Nasser, and S. Schultz, "Composite Medium with Simultaneously Negative Permeability and Permittivity," *Phys. Rev. Lett.*, vol. 84, no. 18, pp. 4184-4187, 2000.
- [10] N.M. Jordan, G.B. Greening, B.W. Hoff, S.S. Maestas, S.C. Exelby, and R.M. Gilgenbach, "Additively Manufactured High Power Microwave Anodes," *IEEE Trans. Plasma Sci.*, pp. 1258-1264, 26 May 2016.
- [11] M. Othman, A. Figotin, and C. Filippo, "Design and Simulation Results of a Hot Test of UCI High Power Degenerate Band Edge Oscillator at UNM," University of California Irvine, Irvine, 2018.
- [12] C.A. Balanis, *Antenna Theory Analysis and Design*, New York, NY, John Wiley & Sons, 1997, pp. 28-36.

- [13] M.G. Schorr and F.J. Beck, "Electromagnetic Field of the Conical Horn," *J. Appl. Phys.*, vol. 21, no. 8, pp. 795-801, 1950.
- [14] A.P. King, "The Radiation Characteristics of Conical Horn Antenna," *Proc. IRE*, vol. 38, no. 3, pp. 249-251, 1950.
- [15] G.A. Mesyats, S.D. Korovin, A.V. Gunin, and V.P. Gubanov, "Repetitively Pulsed High Current Accelerators with Transformer Charging of Forming Lines," *Laser Part. Beams*, vol. 21, no. 2, pp. 197-209, 2003.
- [16] "Sinus-6 Repetitively Pulsed Electron Beam Accelerator & High Power Microwave Source Operation & Maintenance Manual," Institute of High Current Electronics, Tomsk, Russia, 1992.
- [17] T.H. Martin, A.H. Guenther, and M. Kristiansen, Eds., *J.C. Martin, On Pulsed Power, Advances in Pulsed Power Technology*, vol. 3, New York, NY: Plenum Press, 1996.
- [18] N. Engheta and R.W. Ziolkowski, *Metamaterials Physics and Engineering Explorations*, New York, NY: Wiley-IEEE, 2006.
- [19] J.S. Derov, R. Hammond, and I. Young, "The History of the Early Years of Metamaterials in USA and UK Defense Agencies," *J. Optics*, vol. 19, pp. 1-6, 2017.
- [20] G. Singh, R. Rajni, and A. Marwaha, "A Review of Metamaterials and Its Applications," *IJETT*, vol. 19, no. 6, pp. 305-310, 2015.
- [21] E. Sharples and R. Letizia, "Investigation of CSRR Loaded Waveguide for Accelerator Applications," *J. Instrum.*, vol. 9, pp. 1-13, 2014.
- [22] A. Kuskov, "Sinus-6 Pulsed Power Driver Layout," PPLAB, Albuquerque, 2018.
- [23] W. Main, Y. Carmel, K. Ogura, J. Weaver, G.S. Nusinovich, S. Kobayashi, J. P. Tate, J. Rodgers, A. Brombosky, S. Watanabe, M.R. Amin, K. Minami, W.W. Destler, and V.L. Granatstein, "Electromagnetic Properties of Open and Close Overmoded Slow-Wave Resonators for Interaction with Relativistic Electron Beams," *IEEE Trans. Plasma Sci.*, vol. 22, no. 5, pp. 566-576, 1994.
- [24] Z. Zancleris, P. Ragulis, R. Simniskis, and M. Dagys, "Resistive Sensor for High Power Microwave Pulse Measurement in Double Ridge Waveguide," Centre for Physical Sciences and Technology, Vilnius, Lithuania, 2014.
- [25] D. Gamzina, M. Kozina, A. Mehta, E.A. Nanni, S. Tantawi, P.B. Welandar, T. Horn, and C. Ledford, "Copper Reconsidered: Material innovations to Transform Vacuum Electronics," *IVEC 2019*, Busan, South Korea, 2019.

- [26] A.T. Drobot, C.L. Chang, K. Ko, A. Mankofsky, A. Mondelli, L. Seftor, and P. Vitello, "Numerical Simulation of High Power Microwaves Sources," *IEEE Trans. on Nucl. Sci.*, vol. 32, no. 5, pp. 2733-2737, 1985.
- [27] M.A.K. Othman, X. Pan, G. Atmatkakis, C.G. Chirstodoulou, and F. Capolino, "Demonstration of Degenerate Band Edge in Periodically-Loaded Circular Waveguide," *IEEE Microw. Wireless Compon. Lett.*, vol. 25, no. 11, pp. 700-702, 2015.
- [28] A. Farghaly (private communications, 2019).
- [29] J.R. Pierce, *Travelling Wave Tubes*, New York, NY: D. Van Nostrand Company Inc, 1950, pp. 27-29.
- [30] A.D. Grigoriev, A. Vyacheslav, and S. I. Molokovsky, *Microwave Electronics*, Berlin, Germany: Gewerbestrasse, Springer, 2018, p. 534.
- [31] D. Andreev, "UNM-UCI Report for Particle in Cell," PPLAB, Albuquerque, 2019.
- [32] A.B. de Alleluia, *Personal Notes on Experimental Testing of 3D Printed Metamaterial Slow Wave Structure for High Power Microwave Generation*, Albuquerque: PPLab, 2019.
- [33] A. Farghaly (private communications, November 2019).
- [34] X. Lu, J.S. Hummelt, M.A. Shaphiro, and R.J. Temkin, "Long Pulse Operation of a High Power Microwave Source with a Metamaterial Loaded Waveguide," IVEC 2017, London, United Kingdom, 2017.
- [35] K.A. Shipman, *Experimental Testing of a Metamaterial Slow Wave Structure for High Power Microwave Generation* (MS Thesis, University of New Mexico, Albuquerque, NM, 2018).
- [36] H. Chen and M. Chen, "Flipping Photons Backward: Reversed Cherenkov Radiation," *Mater. Today*, vol. 14, no. 1-2, pp. 34-41, 2011.